

COMPUTATIONAL AND THEORETICAL STUDY
OF THE PHYSICAL CONSTRAINTS ON CHEMOTAXIS

A Dissertation

Submitted to the Faculty

of

Purdue University

by

Julien Varennes

In Partial Fulfillment of the

Requirements for the Degree

of

Doctor of Philosophy

May 2018

Purdue University

West Lafayette, Indiana

I dedicate this to all my homies out there.

ACKNOWLEDGMENTS

I would like to thank my advisor and my committee.

TABLE OF CONTENTS

	Page
LIST OF TABLES	vi
LIST OF FIGURES	vii
ABSTRACT	xi
1 Introduction	1
1.1 Cancer-related motivation for Studying Chemotaxis	3
1.2 Physical limits to sensory precision	3
1.2.1 Single-cell concentration sensing	4
1.2.2 Single-cell gradient sensing	7
1.2.3 Multicellular gradient sensing	9
1.3 Models of collective migration	11
1.3.1 Mechanisms of collective migration	11
1.3.2 Model implementations	14
1.3.3 Relative changes vs. absolute molecule numbers	15
1.4 Drug sensitivity and implications for therapy	17
1.5 Outlook	20
2 Constraints on Single-Cell Chemotactic Performance	22
2.1 Review of Chemotaxis Metrics	23
2.1.1 Accuracy	23
2.1.2 Persistence	25
2.1.3 Migration Speed	27
2.2 Experimental Results	28
2.3 Chemotaxis Simulations	30
2.3.1 Computational Implementation	31
2.3.2 Calibration of Simulation Parameters	33

	Page
2.3.3 Simulation Results	34
2.4 Theoretical Model of Chemotaxis	36
2.4.1 BPRW Formulation	37
3 Limits to Collective Chemotaxis	42
3.1 Individual-based Chemotaxis	45
3.2 Emergent Chemotaxis	48
3.3 Model Extensions	51
3.4 Discussion	53
3.5 Description of Simulations	54
3.6 Derivation of Analytic Results	55
3.6.1 Individual-based Chemotaxis	56
3.6.2 Emergent Chemotaxis	57
3.6.3 Variance in Cell & Cluster Polarization	59
3.6.4 Individual-based Chemotaxis	61
3.6.5 Emergent Chemotaxis Clusters	66
4 Dynamics of Collective Chemotaxis	71
4.1 Model	74
4.1.1 Multicellular LEGI Gradient Sensing	74
4.1.2 Connecting Gradient Sensing to Cell Motility	78
4.1.3 Computational Implementation	79
4.2 Results	82
4.3 Discussion	87
REFERENCES	91

LIST OF TABLES

Table	Page
1.1 Gradient sensory thresholds for single cells and multicellular collectives. Note that experiments can provide equal percent concentration differences but unequal molecule number differences across a cell body, as seen for amoeba and breast cancer cells. We see that multicellular groups can detect smaller gradients than single cells by all measures.	17
1.2 Drug sensitivity thresholds. Molecules per cell volume are calculated assuming a cubic cell of length $a = 20 \mu\text{m}$ for tumor cells (rows 1-3) and $a = 10 \mu\text{m}$ for epithelial cells (row 4).	18
2.1 Table of parameters and values used in simulations. The first six parameters are intrinsic to the cell and remain fixed. The final three parameters represent the environment and are varied in Fig. 2.4. Energy costs are in units of $k_B T$, where $k_B T$ is the thermal energy of the CPM Monte Carlo scheme.	34
3.1 Summary of scaling behavior. N dependence of the leading order term for the mean $\langle P_z \rangle$, and the variance (V) and covariance (C) contributions to the relative error $\epsilon^2 = (V + C)/\langle P_z \rangle^2$. C for EC in 2D has a log correction [106].	48
4.1 Table of parameter values. Energy costs are in units of $k_B T$, where $k_B T$ is the thermal energy of the CPM Monte Carlo scheme.	80

LIST OF FIGURES

Figure	Page
1.1 Metastatic invasion is guided by chemical attractants and can occur via (A) single cells or (B) multicellular groups. (C) Drugs are delivered to the tumor environment in order to prevent tumor growth and metastasis. Drugs may cause cell death (orange), block cell-to-cell communication (purple), or prevent cell migration (blue).	4
1.2 Deriving the limits to concentration and gradient sensing. (A) An idealized cell as a permeable sphere that counts molecules inside its volume. (B) A cell counts molecules in two compartments in order to estimate a concentration gradient. (C) The local excitation–global inhibition (LEGI) model of multicellular gradient sensing. Y molecules diffuse between neighboring cells, whereas X molecules do not. The difference between X and Y counts in a given cell reports the extent to which that cell’s concentration measurements are above the average.	5
1.3 Mechanisms of collective migration: (A) individual sensing and migration (the “many wrongs” mechanism), (B) individual sensing but collective migration (emergent chemotaxis), and (C) collective sensing and migration. Implementations of collective migration: (D) in force-based models, dynamics evolve from stochastic forces acting on each cell; (E) in energy-based models, dynamics evolve via energy minimization with thermal noise. E shows the cellular Potts model framework, in which cells are collections of lattice sites, and cell-cell (dashed blue) and cell-environment (dashed yellow) contacts contribute to the energy of the system.	13
2.1 a) Illustration of cell chemotaxis. The cell’s displacement makes an angle θ with the gradient direction. b) Illustration of cell trajectories associated with different CI and CR values. Illustrations of typical cell trajectories are shown in different colors.	24
2.2 a) Directional Autocorrelation from control dataset. Light-colored trajectories indicate autocorrelations for individual cell trajectories. Timescale τ is calculated using Eq. 2.4. b) Directional autocorrelation timescales and CR values for all experimental assays. Data points are color-coded based on chemical environment.	27

Figure	Page
2.3 [Plots a-c can be replaced with box-whisker style plots.] MDA-MB-231 cell chemotaxis assays. Cells are cultured in different chemical environments and trajectories are tracked. CI (a), CR (b) and mean speed (\bar{v}) are reported. d) Summary of chemotaxis assay results, data point size is proportional to mean speed. In all plots colors: no chemoattractant (gray), 400nM EGF uniform concentration (red), 0-800nM EGF gradient (orange), 25nM TGF β uniform concentration (blue), and 0-50nM TGF β gradient (light blue). Error bars are the standard error over the population of trajectories observed.	28
2.4 a) Screen shot of simulation. Cell (gray) is migrating towards increasing chemical concentration, and the white line traces out the cell's path. Inset, illustration of the CPM. A Cell is comprised of simply connected lattice sites. There is an adhesion energy associated with cell-collagen contact, α (red-dashed line). Cell motility occurs through the addition/removal of lattice sites (light-gray). The white dot represents the cell's center of mass and the black arrow its polarization vector \vec{p} . b) Simulation results. Environmental parameters collagen stiffness α (red), background concentration c_0 (green), and gradient g are varied (blue). Parameter values along each trajectory: $\alpha \in \{0.1, 0.4, 0.7, 1.0\}$, $c_0 \in \{1.0, 10.0, 100.0 \text{ nM}\}$, $g \in \{1.0, 5.0, 10.0 \text{ nM}/\mu\text{m}\}$	31
2.5 a) Possible values of CI and CR for a BPRW. Each dot represents the CI and CR value for a BPRW of a given bias and persistence strength. Inset, sample trajectories of a BPRW. b) Example reorientation probability densities $T(\theta, \theta')$, and their component bias $k(\theta)$ and persistence $h(\theta - \theta')$ functions. For both b) plots $\theta' = 0$. For all plots: $t = 36$, $\lambda = 1.0$, $s = 3.75$, and $\theta = 0$ is the direction of bias.	40
2.6 Theoretical bounds on chemotactic performance based on the biased persistent random walk model. Gray dots represent possible theoretical CI and CR values for a BPRW. Colored squares are experimentally recorded values for different environmental conditions.	41
3.1 (a) We study the chemotactic performance of 1D chains, 2D sheets, and 3D clusters of cells. (b) In individual-based chemotaxis (IC), cells in the collective polarize based on their own gradient measurement. (c) In emergent chemotaxis (EC), cell polarization depends on intercellular interactions: cells on the edge polarize based on their measurement of the concentration, and cells in the bulk do not polarize. In both mechanisms the total polarization \vec{P} will fluctuate in magnitude and direction due to noise in cell measurements.	44

Figure	Page
3.2 (a) Mean cluster polarization and (b) relative error for both mechanisms of collective chemotaxis in every configuration. Points are simulation data, colored lines are analytical predictions. 1D EC data plotted with respect to $N - 1$	46
3.3 (a) Short-time integration relative error results. Data points are of simulations for $T = \frac{1}{100}\tau_D$. (b) Exponential concentration profile relative error results. The mean concentration profile is $\bar{c}(z) = c_0 e^{-z/\lambda}$, the lengthscale $\lambda = \sqrt{D/\beta}$ is set by the diffusion coefficient D and the molecule decay rate β . Lines are from original analytical predictions using $T > \tau_D$ and a linear concentration profile.	52
3.4 $\text{Var}[P_z]$ for a 3D cluster of EC cells. Cluster variance shown in red. Pink circles are the single cell variance contributions V , and pink diamonds are the cell-cell covariance contributions C	70
4.1 Model implementation. (A) Cell polarization is biased by multicellular sensing. On average, the cells on the left and right edges will measure negative and positive values of R , respectively. This causes the left-edge (Cell 1) and right-edge (Cell 3) cells to polarize in the direction of the gradient, while cells in the middle (Cell 2) are on average not polarized since $\bar{R} \approx 0$. Polarization vectors \vec{p} are red, repulsion vectors \vec{q} are black. (B) Simulations are implemented using the Cellular Potts Model (CPM). Cells comprise of simply connected lattice points. There are adhesion energies associated with different types of contact: cell-cell, α (blue-dashed line), and cell-ECM, β (yellow-dashed line). Cell motility is modeled by the addition/removal of lattice points (pink). Each cell has a center-of-mass (white dot), a polarization vector, \vec{p} (red) and a repulsion vector, \vec{q} (black).	73

Figure	Page
4.2	Characterizing the emergent multicellular migration. (A) Snapshot from simulation. Individual cells are distinguished by color and white arrows represent their polarization vectors. The cluster centroid is initially located along the gray dashed line and must cross the black dashed line in order to record a first-passage time event. (B) A heat-map of MFPT in units of minutes as a function of cell-ECM adhesion energy, β and polarization bias strength, ϵ . Warmer colors represent higher MFPT values (colorbar). Parameter values for the heat-map: $N = 20$, $\bar{c} = 10\text{nM}$, $g = 0.004\text{nM}/\mu\text{m}$, $\Gamma = 80(\mu\text{m min.})^{-1}$. Illustrations in (C) represent cluster migratory behavior in their respective regimes of parameter space. Larger values of ϵ correspond to larger cell polarization vectors (red arrows), whereas larger values of β correspond to an ECM that is more difficult to traverse. (D) Mean cluster size $\langle N_{\text{sub}} \rangle$ as a function of the total number of cells in the system N . Regime 1: $\beta = 1.5$, $\epsilon = 1.0$. Regime 2: $\beta = 3.5$, $\epsilon = 0.8$
4.3	Tradeoff between sensing and drag leads to a minimum mean first-passage time (MFPT) with cluster size. $\Gamma_0 = 0.80(\mu\text{m min})^{-1}$. (A) MFPT for various values of the exchange rate per unit contact-length Γ . (B) Relative error in gradient sensing for various values of Γ . (C) Area A and perimeter P scaling relationships with the number of cells N in a cluster. (D) MFPT results in A on a log-log scale, compared with the geometric prediction arising from C. All error bars represent standard deviation.
4.4	Prediction to distinguish collective from individual chemotaxis in experiments. (A) Expected MFPT behavior for cluster migration driven by collective sensing. (B) Expected MFPT behavior for cluster migration driven by local interactions.
	83
	85
	89

ABSTRACT

Varennnes, Julien PhD, Purdue University, May 2018. Computational and Theoretical Study of the Physical Constraints on Chemotaxis. Major Professor: Andrew Mugler.

Collective cell migration in response to a chemical cue requires both multicellular sensing of chemical gradients and coordinated mechanical action. Examples from morphogenesis and cancer metastasis demonstrate that clusters of migratory cells are extremely sensitive, responding to gradients of less than 1% difference in chemical concentration across a cell body. While the limits to multicellular sensing are becoming known, how this information leads to coherent migration remains poorly understood. We develop a model of multicellular sensing and migration in which groups of cells collectively measure noisy chemical gradients. The output of the sensing process is coupled to individual cells polarization to model migratory behavior. Through the use of numerical simulations, we find that larger clusters of cells detect the gradient direction with higher precision and thus achieve stronger polarization bias, but larger clusters are also accompanied by less coherent collective motion. The trade-off between these two effects leads to an optimally efficient cluster size. Experimental tests of our model are ongoing and are focused on observations of breast cancer cell migration. Future plans include extending the model to systems of cells which include leading-edge cells that are phenotypically different from non-leading cells, and exploring an alternative model of collective migration in which cells make independent measurements and coordinated behavior emerges through local interactions. By completing these studies we aim to understand the precise roles of multicellular sensing in producing collective cell migration, in metastasis and in general.

1. INTRODUCTION

Parts of the introduction are from my previously published work: J. Varennes and A. Mugler, Sense and sensitivity: physical limits to multicellular sensing, migration and drug response, Molecular Pharmaceutics, 2016.

Cells are extremely sensitive to their environment, capable of gathering information on chemicals in their environment with remarkable precision. For example, the amoeba *Dictyostelium discoideum* is sensitive to chemical concentration differences on the order of ten molecules between its front and back half [1]. Cell sensory precision of chemical concentrations is limited by the extrinsic noise inherent in molecule diffusion. The physical limits to concentration sensing due to extrinsic noise were theoretically derived around 40 years ago by Berg and Purcell [2]. *Escheria coli* bacterium operate very near this physical bound set by extrinsic noise [3]. Studies have revisited the topic of cell sensory precision to account for receptor binding kinetics, spatiotemporal correlations and spatial confinement [4–6].

One very common cellular behavior in response to sensory information is chemotaxis. Chemotaxis is the process in which a cell or organism moves in response to a changing chemical concentration in its environment. There are two canonical forms of chemotaxis; cells either move towards the direction of increasing chemical concentration (positive chemotaxis), or they move away from the chemical and migrate in the direction of decreasing chemical concentration (negative chemotaxis). Positive chemotaxis may occur in response to nutrients in the environment, whereas negative chemotaxis is caused by waste or poisons in the environment. This work is focused solely on positive chemotaxis, and we refer to the chemical signal that induces positive chemotaxis as the chemoattractant. Chemotaxis is critical to many biological processes in single-celled organisms as well as within multicellular organisms such as: nutrient search, organism development, wound healing, immune system target-

ing, and cancer metastasis [7, 8]. Since chemical sensing is necessary for chemotaxis to occur, the extrinsic noise in sensing affects chemotactic performance. Therefore studying the effect of extrinsic noise on chemotaxis can yield physical insight into chemotaxis and how it constrains the many biological processes mentioned above.

Chemotaxis can be viewed as a three step process: chemical sensing, polarization, and locomotion. Detection of a chemical gradient causes an asymmetric response in the cell's sensory network, this leads to intracellular actin polymerization polarizing the cell along the asymmetry, and protrusions and retractions are made in the polarization direction. Many studies have examined chemotaxis at the intracellular level in order to understand the biochemical machinery involved in producing polarization and locomotion [9, 10]. Modeling how cell signaling produces polarization is still unclear [7]. Additionally, in many biological contexts cells act in close proximity to one another so their interactions may have a significant impact on their chemotactic performance [11].

Here we develop models that link sensing to polarization in order to examine how extrinsic noise from cell sensing puts physical constraints on chemotaxis. First, we briefly review the fundamental limits to concentration sensing and gradient sensing precision for single cells and multicellular collectives. We apply our computational and theoretical models to breast cancer cell chemotaxis. Computational simulations are conducted to explain and predict their chemotactic performance, and provide a relationship to common cell-migration experimental observables. We find that our simulations and theoretical model place physical constraints on the chemotactic performance of the breast cancer cells observed in experiments. Single-cell chemotaxis simulations also give predictive power over how experimental parameters affect chemotactic performance in different ways. Next, we examine multicellular chemotaxis. Cells often exist and function in collective groups and chemotaxis is no different. We develop a novel theoretical approach to studying the effects of extrinsic noise on collective chemotaxis. We find that chemotactic performance is dependent on the type of collective behavior as well as on experimental parameters. Finally, we extend our

single-cell chemotaxis simulations to multicellular chemotaxis. A model that explicitly accounts for extrinsic noise, as well as noise in intercellular communication, is used to study the performance of communication-aided multicellular chemotaxis.

1.1 Cancer-related motivation for Studying Chemotaxis

Chemotaxis plays an important role in many biological processes, of which cancer metastasis is one that stands out for significant importance. The first step of metastasis is invasion, wherein cells break away from their original tumor and invade the surrounding tissue. Our understanding of metastatic invasion has benefited tremendously from genetic and biochemical studies [12–14]. However, the physical aspects of metastatic invasion are still unclear [14]. Previous research shows that cancer cells sense and respond to chemical gradients provided by surrounding cells [15–18] or other features of the tumor environment [17, 19, 20] (Fig. 1.1A,B). Indeed, cancer cells are highly sensitive, able to detect a 1% difference in concentration across the cell length [17], and sometimes chemotax in response to these signals. Since metastasis is one of the most critical and lethal stages of cancer, studying the basic physics underlying chemotaxis can help us better understand metastasis.

During metastasis, chemotaxis can occur as a single-cell (Fig. 1.1A) or a multicellular phenomenon (Fig. 1.1B).

1.2 Physical limits to sensory precision

Cancer cells can sense very small concentration gradients [17] and may also act collectively [18, 21–23]. We review the basic theory of concentration and gradient sensing by cells and cell collectives. This theory places physical limits to sensory precision due to extrinsic noise caused by the diffusing chemical.

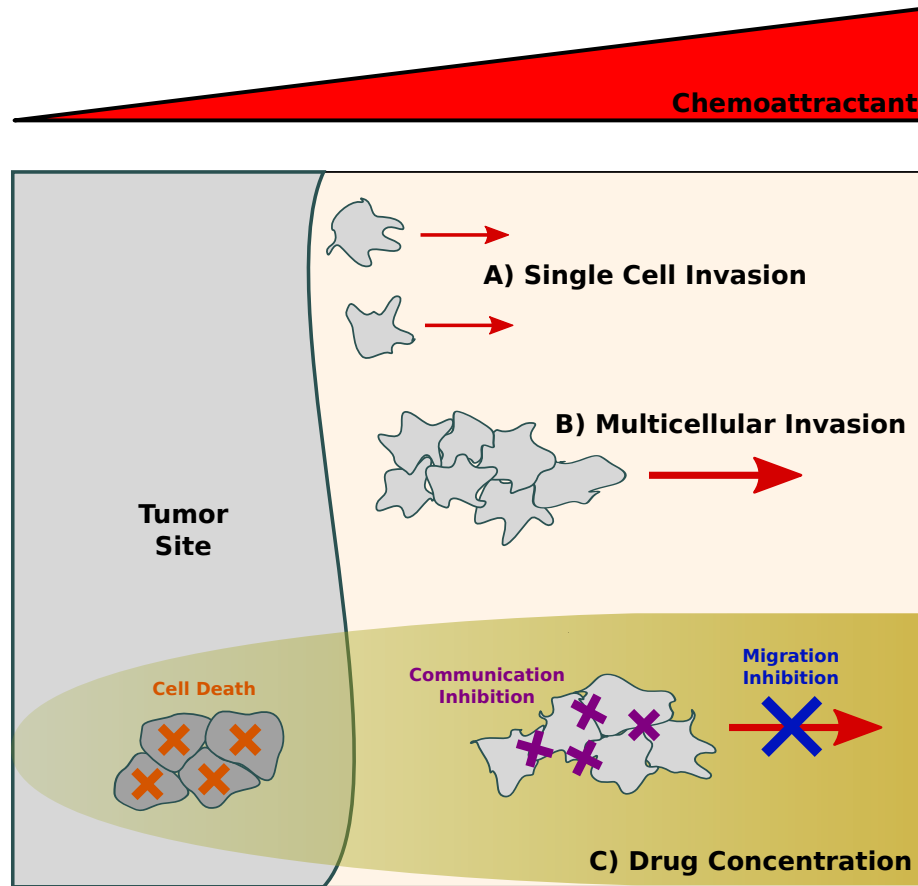


Fig. 1.1. Metastatic invasion is guided by chemical attractants and can occur via (A) single cells or (B) multicellular groups. (C) Drugs are delivered to the tumor environment in order to prevent tumor growth and metastasis. Drugs may cause cell death (orange), block cell-to-cell communication (purple), or prevent cell migration (blue).

1.2.1 Single-cell concentration sensing

Theoretical limits to the precision of concentration sensing were first introduced by Berg and Purcell almost 40 years ago [2]. Berg and Purcell began by considering an idealized cell that acts as a perfect counting instrument. The cell is assumed to be spherical and that molecules can freely diffuse in and out of it (Fig. 1.2A). The concentration of these molecules is uniform in space, and the cell derives all its information about the concentration by counting each molecule inside its spherical

body. The expected count is $\bar{n} = \bar{c}V$ where \bar{c} is the mean concentration and V is the cell volume. However, since molecules arrive and leave via diffusion, there will be fluctuations around this expected value. Diffusion is a Poisson process, meaning that the variance in this count σ_n^2 equals the mean \bar{n} . Therefore the relative error in the cell's concentration estimate is $\sigma_c^2/\bar{c}^2 = \sigma_n^2/\bar{n}^2 = 1/(\bar{c}V)$.

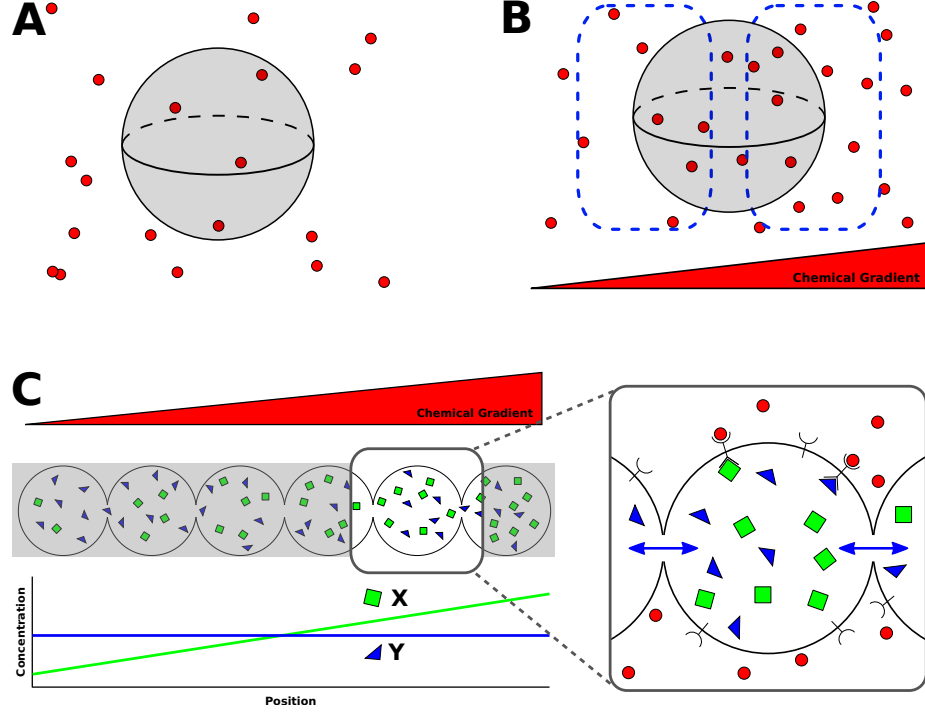


Fig. 1.2. Deriving the limits to concentration and gradient sensing. (A) An idealized cell as a permeable sphere that counts molecules inside its volume. (B) A cell counts molecules in two compartments in order to estimate a concentration gradient. (C) The local excitation–global inhibition (LEGI) model of multicellular gradient sensing. Y molecules diffuse between neighboring cells, whereas X molecules do not. The difference between X and Y counts in a given cell reports the extent to which that cell's concentration measurements are above the average.

The cell can improve upon the relative error in its concentration estimate by time-averaging over multiple measurements. However, consecutive measurements are only statistically independent if they are separated by a sufficient amount of time such

that the molecules inside the cell volume are refreshed. The amount of time required is characterized by the diffusion time, $\tau \sim V^{2/3}/D \sim a^2/D$, where D is the diffusion constant and a is the cell diameter. In a time period T the cell makes $\nu = T/\tau$ independent measurements, and the variance is reduced by the factor $1/\nu$. This gives the long-standing lower limit

$$\frac{\sigma_c^2}{\bar{c}^2} = \frac{\sigma_n^2}{\bar{n}^2} \sim \frac{1}{a\bar{c}DT} \quad (1.1)$$

for the cell's relative error in estimating a uniform concentration. The relative error decreases with a and \bar{c} , since the molecule count is larger, and also with D and T , since more independent measurements can be made. Berg and Purcell derived this limit more rigorously [2], and the problem has been revisited more recently to account for binding kinetics, spatiotemporal correlations, and spatial confinement [4–6]. In all cases a term of the form in Eq. 1.1 emerges as the fundamental limit for three-dimensional diffusion.

Does cell sensory performance reach this limit in real biological contexts? Berg and Purcell themselves addressed this question using the *Escheria coli* bacterium [2]. Motility of *E. coli* has two distinct phases: the run phase in which a cell swims in a fixed direction, and the tumble phase in which the cell erratically rotates in order to begin a new run in a different direction. The bacterium biases its motion by continually measuring the chemoattractant concentration, and extending the time of runs for which the change in concentration is positive [2, 24]. The change in concentration $\Delta\bar{c} = Tv\bar{g}$ over a run time T depends on the concentration gradient $\bar{g} = \partial\bar{c}/\partial x$ and the bacterium's velocity v . Berg and Purcell argued that for a change in concentration to be detectable, it must be larger than the measurement uncertainty, $\Delta\bar{c} > \sigma_c$. Together with Eq. 1.1, this places a lower limit on the run time, $T > [\bar{c}/(aDv^2\bar{g}^2)]^{1/3}$. Using typical values [2] for the sensory threshold of *E. coli* of $\bar{c} = 1$ mM, $\partial\bar{c}/\partial x = 1$ mM/cm, $a = 1$ μ m, $v = 15$ μ m/s, and $D = 10^{-5}$ cm²/s, we find $T > 0.1$ s. Actual run times are on the order of 1 s. Thus we see that *E. coli* chemotaxis is consistent with this physical bound. The fact that actual run times are not too much longer than the minimum indicates that the sensory machinery of *E. coli* operates near the

optimal precision of a perfect counting device. If *E. coli* were to use much shorter run times, there would be no way to acquire sufficient statistics, and chemotaxis would be physically impossible.

1.2.2 Single-cell gradient sensing

Unlike *E. coli* bacterium, larger cells do not need to swim in order to detect temporal changes in concentration. Larger cells, like amoeba, epithelial cells, neutrophils, and neurons, sense gradients by comparing concentration measurements between spatially separate compartments along the cell body [10]. These compartments are typically receptors or groups of receptors on the cell surface, but in a simple model we may treat these compartments as idealized counting volumes as we did for concentration sensing. The difference in counts between two such compartments provides the cell with an estimate of the gradient (Fig. 1.2B). Following the same procedure as for concentration sensing we can derive the relative error in gradient sensing.

Consider two compartments of linear size s on either side of a cell with diameter a (Fig. 1.2B). Given that the compartments are aligned with the gradient \bar{g} of a linear concentration profile, then the mean concentrations at each compartment are \bar{c}_1 and $\bar{c}_2 = \bar{c}_1 + a\bar{g}$. The mean molecule counts in the two compartments are roughly $\bar{n}_1 = \bar{c}_1 s^3$ and $\bar{n}_2 = \bar{c}_2 s^3$, and the difference is $\Delta\bar{n} = \bar{n}_2 - \bar{n}_1 = a\bar{g}s^3$. The variance in this difference is $\sigma_{\Delta n}^2 = \sigma_{n_1}^2 + \sigma_{n_2}^2 \sim \bar{n}_1^2/(s\bar{c}_1 DT) + \bar{n}_2^2/(s\bar{c}_2 DT)$, where the first step assumes the two compartments are independent, and the second step uses Eq. 1.1 for the variance in each compartment's measurement. For shallow gradients, where the limits on sensing are generally reached, $a\bar{g} \ll \bar{c}_1$, and so $\bar{c}_1 \approx \bar{c}_2 \approx \bar{c}$, where \bar{c} is the mean concentration at the center of the cell. Thus $\sigma_{\Delta n}^2 \sim 2(\bar{c}s^3)^2/(s\bar{c}DT)$, and the relative error in the cell's estimate of the gradient is then

$$\frac{\sigma_g^2}{\bar{g}^2} = \frac{\sigma_{\Delta n}^2}{\Delta\bar{n}^2} \sim \frac{\bar{c}}{s(a\bar{g})^2 DT}, \quad (1.2)$$

where the factor of 2 is neglected in this simple scaling estimate. Similar to Eq. 1.1, the relative error in gradient sensing decreases with s , since larger compartments allow

for larger molecule counts. The relative error also decreases with D and T , since they increase the number of independent measurements. Additionally, the relative error decreases with $a\bar{g}$, since the concentrations measured by the two compartments are more different from each other. However, we see that unlike Eq. 1.1, the relative error increases with the background concentration \bar{c} . The cell is measuring a concentration difference, not the concentration itself, and it is more difficult to accurately measure a small difference on a larger background than on a smaller background [25]. Eq. 1.2 has been derived more rigorously in other studies [26], and the problem has been extended to describe different receptor configurations and geometries [26–28]. In all these cases, the relative error has a term similar to Eq. 1.2, with the lengthscale s dictated by the particular sensory mechanism and geometry. The optimal mechanism would result in an effective compartment size that is roughly half of the cell volume, in which case $s \sim a$.

I don't like the Endres Wingreen part of this paragraph. Experiments on the amoeba *Dictyostelium discoideum* have tested the limits to gradient sensing [29]. *Dictyostelium* cells exhibit biased movement when exposed to gradients of cyclic adenosine monophosphate as small as $\bar{g} = 10$ nM/mm, on top of a background concentration of $\bar{c} = 7$ nM. Bias is typically quantified in terms of the chemotactic index (CI), which is the cosine of the angle between the gradient direction and the direction of a cell's actual motion. By relating the error in gradient sensing (a term of the form in Eq. 1.2 with $s = a$) to the error in this angle, Endres and Wingreen [27] obtained an expression for the optimal CI, which they then fit to the experimental data with one free parameter, the integration time T . The inferred value of $T = 3.2$ s serves as the physical lower bound on the response time required to perform chemotaxis. Actual response times of *Dictyostelium* cells, as measured by the time from the addition of a chemoattractant to the peak activity of an observable signaling pathway associated with cell motility [30,31], are about 5 – 10 s. Taken together, these results imply that *Dictyostelium* operates remarkably close to the physical limit to sensory precision set by the physics of molecule counting.

1.2.3 Multicellular gradient sensing

Next, we turn our attention to multicellular gradient sensing. In many biological processes, such as metastatic invasion [21, 22], cells behave in a collective manner. Collectives of cells sense shallower gradients than single cells, both in terms of percent concentration changes and absolute molecule numbers (Table 1.1). For example, neuron collectives respond to gradients equivalent to a difference of less than one molecule across an individual neuron's growth cone [32]. It is likely that this benefit in sensory precision found in collectives also translates to better chemotaxis for collectives. This may be a reason why collective invasion is sometimes observed during metastasis.

From Eq. 1.2 we see that a multicellular collective has lower sensory error because it is larger than a single cell. The cell collective spans a larger portion of the concentration profile, leading to a larger difference between the concentration measurements on either end, and a lower relative error. In terms of Eq. 1.2, if we consider that cells on the ends act as the molecule-counting compartments, $s \rightarrow a$, and that the entire collective acts as the detector, $a \rightarrow Na$, where N is the number of cells in the gradient direction, then we have [33]

$$\frac{\sigma_g^2}{\bar{g}^2} \sim \frac{\bar{c}}{a(Na\bar{g})^2DT}. \quad (1.3)$$

As expected, the relative error goes down with the size Na of the multicellular collective.

It is important to note that in formulating Eq. 1.3 we have overlooked any loss of precision caused by communicating sensory information across the collective. The larger the group of cells, the more difficult it will be for cells on either end to communicate measurement information. Eq. 1.3 does not account for this, and assumes that any error induced by the communication process is negligible. In fact, Eq. 1.3 states that the relative error decreases with increased collective size. For a single cell it may be a reasonable approximation to assume that compartments quickly and reliably communicate information across the cell body, but for a multicellular collective, the

communication process should deteriorate as the collective grows in size. This process introduces additional noise to the collective’s gradient sensing abilities. Therefore, it is imperative when considering collective sensing to properly account for the effects of communication.

Recent studies have explored the physical limits to collective gradient sensing for different communication mechanisms and collective geometries [25, 33, 34]. In two of the studies [25, 33] communication was modeled using a multicellular version of the local excitation–global inhibition (LEGI) paradigm [35], in which each cell produces a “local” and a “global” molecular species in response to the chemical in the environment. The global species is exchanged between cells to provide the communication, whereas the local species remains within the cell it was produced (Fig. 1.2C). The difference between local and global molecule numbers in a cell provides it with information about the chemical gradient. A positive difference informs the cell that its measured concentration (represented by the local species) is above the spatial average among its neighbors, and therefore that the cell is located up the gradient, not down. The relative error of gradient sensing for the LEGI model was shown [33] to be limited from below by

$$\frac{\sigma_g^2}{\bar{g}^2} \sim \frac{\bar{c}}{a(n_0 a \bar{g})^2 D T}, \quad (1.4)$$

where n_0^2 is the ratio of the global species’ cell-to-cell exchange rate to its degradation rate. When communication is accounted for the error is bounded by $n_0 a$, whereas in Eq. 1.3 the error decreases indefinitely with size Na . The communication strength defines an effective number of cells n_0 over which information can be reliably conveyed, and a collective that grows beyond this size no longer improves its sensory precision.

The communication-limited relative error prediction was tested experimentally in epithelial cell collectives [25]. Mouse mammary epithelial cells were grown in organotypic culture and subjected to very shallow gradients of epidermal growth factor (Table 1.1). While single epithelial cells did not respond to the gradient, the multicellular collectives exhibited a biased cell-branching response. Critical to communication-limited prediction, the response of large collectives was no more biased than that

of small collectives, supporting the idea that communication sets an effective collective size. From experiments the effective collective size was inferred to be $n_0 \approx 3.5$ cells, which is consistent with the collective sizes found in nature (the “end buds” of growing mammary ducts) [36]. Communication between cells is mediated by gap junctions between cells, and experiments show that when gap junctions are blocked, the biased response in collectives vanished [25]. This demonstrates that collective response is critically dependent on cell-to-cell communication. Taken together, these results indicate that communication is a necessary but imperfect component of collective gradient sensing. The results also speak to the power of simple physical theory to quantitatively explain collective cellular capabilities. Many epithelial cancers are known to invade collectively [21], and these theoretical predictions may also describe the sensory behavior of metastatic cell collectives.

BELOW NOT EDITED

1.3 Models of collective migration

Here we review models of migration since chemotaxis involves both sensing and movement. From a physical modeling perspective, describing collective cell dynamics is an interesting problem, because often rich and unexpected behavior can emerge from a few simple interaction rules between cells. Even in the absence of sensing, simple models have successfully explained observed collective behaviors such as cell streaming, cell sorting, cell sheet migration, wound healing, and cell aggregation [37–40]. Here we focus on the collective dynamics that emerge when sensing plays a key role. In this case, a sensory cue results in polarization of a cell or cell collective via one of a variety of mechanisms [10], and the dynamics are directed, i.e. migratory.

1.3.1 Mechanisms of collective migration

Mechanisms of collective migration can largely be divided into three categories. First, cells may exhibit individual sensing and individual migration (Fig. 1.3A). Here,

each cell can perform gradient sensing and migration individually, although the precision may be low. When many such cells are placed in a group, the group migration can be enhanced and focused by local interactions between the cells. Even if each individual cell has low sensory and migratory precision, the precision of the group as a whole is high due to the interactions. This mechanism is often termed “many wrongs,” and it is successful at explaining how group migratory behavior emerges from individual agents that act independently [41]. For example, a recent study demonstrated that single-cell chemotaxis can be improved through collisions between cells which align cell polarization in the gradient direction [42]. Collisions act to average over the errors in individual cells’ noisy measurements, thereby decoupling group behavior from single-cell properties.

Second, cells may exhibit individual sensing but collective migration (Fig. 1.3B). In this mechanism, each individual cell senses its own local environment, and tight mechanical interactions result in the emergent directed motion of the entire group. This mechanism is applicable to the collective migration of connected clusters of cells. For example, a model of this type was recently developed by Camley et al. to describe behavior seen in clusters of neural crest cells and other cell types [43]. In this model, cells are tightly connected but are polarized away from neighboring cells due to contact inhibition of locomotion (CIL), the physical phenomenon of cells ceasing motion in the direction of cell-cell contact [44]. Individual cells sense a local chemoattractant concentration and attempt to migrate away from the group with a strength proportional to this concentration. However, the mechanical coupling keeps them together. In the presence of a concentration gradient, the imbalance in their migration strengths results in net directed motion (Fig. 1.3B). Notably, this mechanism results in directed motion of a cluster even though individual cells cannot execute directed motion alone, since without other cells, there is no CIL to bias the motion.

Third, cells may exhibit collective sensing and collective migration (Fig. 1.3C). As discussed above, multicellular groups exploit cell-to-cell communication to sense

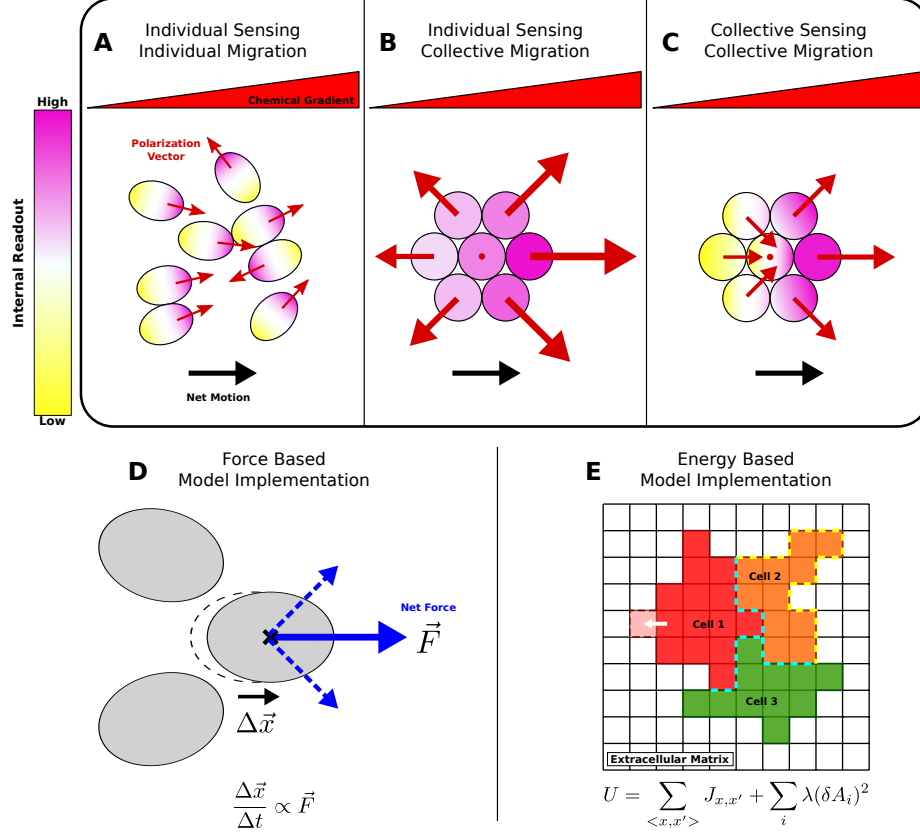


Fig. 1.3. Mechanisms of collective migration: (A) individual sensing and migration (the “many wrongs” mechanism), (B) individual sensing but collective migration (emergent chemotaxis), and (C) collective sensing and migration. Implementations of collective migration: (D) in force-based models, dynamics evolve from stochastic forces acting on each cell; (E) in energy-based models, dynamics evolve via energy minimization with thermal noise. E shows the cellular Potts model framework, in which cells are collections of lattice sites, and cell-cell (dashed blue) and cell-environment (dashed yellow) contacts contribute to the energy of the system.

gradients collectively, thereby enhancing the precision of sensing. A feature of this collective sensing, e.g. via the multicellular LEGI mechanism discussed above [25,33], is that each cell has information on the extent to which it is up or down the gradient. Through CIL or other contact-mediated interactions, this information can translate directly into cell polarity, leading to more coherent collective migration than in the

previous mechanism (Fig. 1.3C vs. B). In fact, the multicellular LEGI model was used by Camley et al. [43] to explore a model of this type. Adding collective sensing to their model of CIL-dependent migration gave the advantage that the repulsive tension on a cell cluster was adaptive and therefore remained constant as the cluster migrated to regions of higher chemical concentration.

1.3.2 Model implementations

To study the above mechanisms quantitatively and compare predictions with experiments, one must turn to mathematical and computational modeling. Models of cell dynamics range from continuum or semi-continuum descriptions, which describe groups of cells as continuous tissues, to individual-based models, which describe cells as individual interacting entities [45]. Physics-driven individual-based models generally fall into two categories: force-based models and energy-based models.

Force-based models (Fig. 1.3D) typically represent cells as centers of mass or as collections of vertices. Cell dynamics evolve from forces acting on individual cells, which can be stochastic, and arise from internal features such as cell polarity, and external features such as mechanical interactions with other cells [45]. Force-based models are able to reproduce multicellular behavior such as chemotaxis, wound healing, and cell aggregation [39, 40, 43]. Parameters are often directly relatable to experimental measurements, and the simplest models are often amenable to exact mathematical analysis [43].

Energy-based models (Fig. 1.3E) allow cell dynamics to emerge from the minimization of a potential energy with thermal noise (the so-called Monte Carlo scheme). A widely used example is the cellular Potts model (CPM) [46, 47], in which cells are represented as collections of co-aligned “spins” on a lattice (Fig. 1.3E). Cells remain contiguous because it is energetically favorable for neighboring spins to be co-aligned. Biophysical features such as cell shape, cell-cell adhesion, and cell protrusions into the environment are modeled by introducing corresponding terms into the global

potential energy. The CPM has been used to describe cell sorting, streaming, and chemotaxis [48] and has successfully reproduced experimental observations of epithelial streaming, cell sorting, and collective migration [37, 38, 48]. In energy-based models, the parameters are less directly relatable to experiments; rather, their values can often be set by calibrating emergent features, such as cell diffusion coefficients or average speeds, with experimental measurements [38].

Although the physical limits to multicellular sensing are becoming better understood, the physical limits constraining multicellular migration are less clear. This remains an interesting open question, and answering it will require integrating the theories of sensing and communication with the models of collective migration described herein. For tumor cells in particular, an integrated physical theory of sensing and migration would prove immensely useful for identifying the key determinants of invasive capabilities. Identifying these determinants would help pinpoint the ways that these capabilities could be disrupted, using drugs and other therapies, as described next.

BELOW IS OLD
REVIEW STARTS BELOW

1.3.3 Relative changes vs. absolute molecule numbers

The precision of gradient sensing is often reported in terms of percent concentration change across a cell body. For example, both amoeba [29] and tumor cells [17] are sensitive to a roughly 1% change in concentration across the cell body. However, this method of reporting sensitivity may be misleading. Experiments imply very different sensory thresholds for these cells in terms of absolute molecule numbers, as we will now see.

The key is that it takes two numbers to specify the conditions for gradient sensing: the mean gradient \bar{g} and the mean background concentration \bar{c} . For the amoeba *Dictyostelium*, these numbers are $\bar{g} = 10$ nM/mm and $\bar{c} = 7$ nM at the sensory

threshold [29]. Given a typical cell size of $a = 10 \mu\text{m}$, these values imply a mean percent concentration change of $\bar{p} = a\bar{g}/\bar{c} = 1.4\%$ (Table 1.1). However, we may also compute from these values the mean molecule number difference $\Delta\bar{n} = a\bar{g}s^3$ from one side of the cell to the other, within the effective compartments of size s . Taking $s \sim a$ gives the maximal molecule number difference of $\Delta\bar{n} = a^4\bar{g} = 60$ for *Dictyostelium* (Table 1.1). Together \bar{p} and $\Delta\bar{n}$ specify the sensing conditions as completely as \bar{g} and \bar{c} do.

Experiments [17] have shown that breast cancer tumor cells exhibit a chemotactic response in a gradient $\bar{g} = 550 \text{ nM/mm}$ of the cytokine CCL21, on top of a background concentration of $\bar{c} = 1100 \text{ nM}$. Given a typical cell size of $a = 20 \mu\text{m}$, this corresponds to a percent difference of $\bar{p} = a\bar{g}/\bar{c} = 1\%$, similar to *Dictyostelium*. Yet, this also corresponds to a maximal molecule number difference of $\Delta\bar{n} = a^4\bar{g} = 53,000$, which is much higher than that of *Dictyostelium* (Table 1.1). Even though the sensitivities are similar in terms of percent change, they are very different in terms of absolute molecule number.

Lower molecule numbers correspond to higher relative error. We can see this explicitly by writing Eq. 1.2 in terms of the percent change $\bar{p} = a\bar{g}/\bar{c}$. Defining $\epsilon = \sigma_g/\bar{g}$ and taking $s \sim a$, we have $\epsilon \sim 1/\sqrt{\bar{p}^2 a \bar{c} D T}$. Accounting for the fact that tumor cells (TC) have roughly twice the diameter as *Dictyostelium* cells (DC), this expression implies that the sensitivities of the two cell types over the same integration time T to chemoattractants with the same diffusion constant D satisfy $\epsilon_{\text{DC}}/\epsilon_{\text{TC}} = \sqrt{2\bar{c}_{\text{TC}}/\bar{c}_{\text{DC}}} \approx 18$. We see that because the *Dictyostelium* experiments were performed at lower background concentration, corresponding to lower absolute molecule numbers, the relative error in gradient sensing is 18 times that of the tumor cells, despite the fact that both cell types are responsive to 1% concentration gradients. Therefore, it is important to take note of the background concentration when studying the precision of gradient sensing. These data imply that *Dictyostelium* cells can sense noisier gradients than tumor cells. However, *Dictyostelium* cells have been studied more extensively than tumor cells as exemplars of gradient detection. It

	Single Cell		Multicellular	
	<i>Dictyostelium</i> (Amoeba) [29]	Breast Cancer [17]	Neurons [32]	Mammary Epithelia [25]
Cell Length Scale, a	10 μm	20 μm	10 μm	10 μm
Background Concentration, \bar{c}	7 nM	1100 nM	1 nM	2.5 nM
Concentration Gradient, \bar{g}	10 nM/mm	550 nM/mm	0.1 nM/mm	0.5 nM/mm
Percent Concentration Difference, $\bar{p} = \bar{g}a/\bar{c}$	1.4%	1.0%	0.1%	0.2%
Molecule Number Difference, $\Delta\bar{n} = \bar{g}a^4$	60	53,000	0.6	3

Table 1.1.

Gradient sensory thresholds for single cells and multicellular collectives. Note that experiments can provide equal percent concentration differences but unequal molecule number differences across a cell body, as seen for amoeba and breast cancer cells. We see that multicellular groups can detect smaller gradients than single cells by all measures.

remains an interesting open question what is the minimum gradient that tumor cells can detect, not only in terms of percent concentration change, but also in terms of absolute molecule number differences.

1.4 Drug sensitivity and implications for therapy

We have seen that cells, including tumor cells, are remarkably precise sensors of molecules in their environment. This raises the question of how sensitive tumor cells are to drug molecules in their environment. What is the minimum drug concentration

Outcome	Drug Concentration	Molecules per Cell
Physical change [49]	1 nM	5,000
Cell death [50]	10^4 nM	5×10^7
Cell death, nanoparticle delivery [51]	100 nM	500,000
Communication blockage [25]	50 nM	30,000

Table 1.2.

Drug sensitivity thresholds. Molecules per cell volume are calculated assuming a cubic cell of length $a = 20 \mu\text{m}$ for tumor cells (rows 1-3) and $a = 10 \mu\text{m}$ for epithelial cells (row 4).

required not just for precise detection by a cell, but for causing a phenotypic change, such as cell death?

Experiments have shown that cancer cells are sensitive to very small drug concentrations. For example, lung carcinoma cells were exposed *in vitro* to various concentrations of the anti-cancer drug paclitaxel, also known as taxol, which acts to block mitosis in order to achieve cell death by disrupting microtubule regulation [49]. Paclitaxel concentrations as low as 1 nM were shown to affect microtubule dynamics of the cells. This concentration is commensurate with the smallest background concentrations in which cells can perform gradient sensing (Table 1.1). Assuming a cell length of $20 \mu\text{m}$, this concentration corresponds to only a few thousand drug molecules in the volume of a cell (Table 1.2). Evidently lung cancer cells are affected by drug concentrations that are near the fundamental limits of what can be sensed.

Although cancer cells may be very sensitive to small drug concentrations, that does not translate to successful treatment. In order to achieve cell death, much larger drug concentrations are required. In the same study on lung carcinoma cells, cell death was observed for drug concentrations on the order of 10 nM and greater. More typical drug concentrations required for cell death are on the order of micromolars. For instance, it has been shown *in vitro* that anticancer drug concentrations on the

order of $10\ \mu\text{M}$ are required to kill at least 90% of tumor cells [50]. With a cell length of $20\ \mu\text{m}$, $10\ \mu\text{M}$ corresponds to tens of millions of drug molecules in the volume of a cell, four orders of magnitude greater than drug concentrations required to affect cell functionality (Table 1.2). In order to effectively kill a solid tumor, very high drug doses are required.

Complicating matters is the fact that the tumor and its surrounding microenvironment comprise a complex and heterogeneous system. Although most cells in the human body are naturally within a few cell lengths of a blood vessel, due to high proliferation tumor cells may be upwards of tens of cell lengths away from a vessel [52]. This makes it difficult for drugs to reach the tumor. Moreover, the high density of many solid tumors causes gradients of drug concentration to form as a function of tumor radius [53]. This results in a reduced drug concentration at the center of the tumor and makes innermost tumor cells the most difficult to kill. A promising way to overcome this difficulty is through the use of nanoparticle drug delivery systems, which increase both the specificity and penetration of drugs to the tumor. Nanoparticle delivery has been shown [51] to achieve cell death with concentrations as low as $100\ \text{nM}$. Although this concentration is lower than for delivery without nanoparticles, it is still two orders of magnitude higher than the minimum concentration that causes physical changes in the cell (Table 1.2). Even with targeted delivery, achieving drug-induced tumor cell death remains a challenging task.

Given this challenge, we may hope to draw upon the physical insights reviewed herein to devise therapeutic strategies that are alternative or complementary to comprehensive cell death. Specifically, we imagine focusing on the metastatic invasion phase, and targeting the functions of invading tumor cells, including communication and migration, in addition to targeting cells' overall viability, to produce better treatment (Fig. 1.1C). Communication is a particularly promising candidate, since it has recently been shown that cell-to-cell communication makes cancer cells more resistant to therapy and helps sustain tumor growth [54]. Indeed, the exchange of extracellular vesicles, which is a form of communication observed between tumor cells and stromal

cells, has been linked to immune suppression, tumor development, angiogenesis, and metastasis [55]. This suggests that disrupting cell-to-cell communication could be an effective strategy for stopping tumor progression or curbing metastatic invasion. Disrupting communication may not require concentrations as large as those necessary for cell death, which are difficult to maintain *in vivo* across the whole tumor. For example, as little as 50 nM of the gap-junction-blocking drug Endothelin-1 is sufficient to remove collective responses in epithelial cells [25]. This concentration is several orders of magnitude smaller than that required for comprehensive cell death, and it is on the order of concentrations that are effective with targeted nanoparticle delivery (Table 1.2). Therefore, it is tempting to suggest that managing metastatic invasion by blocking communication or other cell functions is a more accessible therapeutic strategy than eradicating a tumor outright.

1.5 Outlook

In this review, we have taken a quantitative look at metastatic invasion as a sensing-and-migration process, which has allowed us to compare metastatic cells to other cell types in terms of their physical capabilities. We have seen that tumor cells can sense very shallow chemoattractant gradients, which may help guide metastatic invasion, but it remains unclear whether tumor cells operate near fundamental sensing limits, as bacteria and amoeba do. Recognizing that metastatic invasion can be collective, we have reviewed recent results on the physical limits to collective sensing, and we have identified the overarching mechanisms of collective migration. A key insight that emerges is that collective capabilities rely critically on cell-to-cell communication. This insight opens up alternative strategies for therapy that target specific cell capabilities such as communication, in addition to strategies that aim for comprehensive cell death.

Moving forward, it will be important to identify whether the physical theory of sensing reviewed herein can be applied in a predictive manner to tumor cells, and

whether gradient sensing plays a dominant role during metastatic invasion. More generally, it will be necessary to integrate the theory of sensing with models of collective migration to predict quantitatively what groups of migratory cells can and cannot do. Finally, controlled experiments with metastatic cells are required to validate these predictions, and to assess the viability of alternative therapies that target specific cell functions in order to combat metastatic invasion. Our hope is that the integrated, physics-based perspective presented herein will help generate innovative solutions to the pervasive problem of metastatic disease.

2. CONSTRAINTS ON SINGLE-CELL CHEMOTACTIC PERFORMANCE

In this chapter we examine the constraints that the external environment poses on single-cell chemotaxis. This is accomplished through collaboration with Dr. Bumsoo Han’s group. I develop a computational model of single-cell chemotaxis, in conjunction with Dr. Bumsoo Han and Hye-ran Moon’s experiments on breast cancer cells. From simulations we are able to predict how environmental parameters affect cancer cell chemotactic performance, and we use a simple physical model to explain how chemotaxis is constrained by these same environmental parameters.

As mentioned in Chapter 1, chemotaxis can be broken down into cell sensing, polarization, and locomotion. How well the cell executes these aspects of chemotaxis determines its performance. Just as the fundamental limits to cell sensory precision is set by the extrinsic noise in chemical diffusion, chemotactic performance is limited by extrinsic and intrinsic parameters present in its three core components. The ability for the cell to polarize and induce motility is an intrinsic property of the particular cell-type in question. Whereas environmental parameters affect what the cell can sense and its ability to move, providing extrinsic limits to chemotaxis. Here we focus solely on environmental parameters, and study how they place extrinsic limits on chemotactic performance.

Before presenting experimental, simulation, and theoretical results, the most prevalent chemotaxis metrics found in the literature are reviewed. This is important because a wide variety of metrics are used to measure the chemotactic performance, and often go by the same or very similar names. Metrics are dependent on the details of each experimental set-up, and it is frequently unclear how different metrics can be compared or related between studies. This ambiguity makes identifying quantitative patterns between different studies very challenging. From the review we identify

three metrics that provide a comprehensive and intuitive description of chemotactic behavior. The three metrics quantify accuracy, persistence, and speed. Next, we present experimental data on breast cancer cells chemotaxis performed by the Han group. Simulations of single-cell chemotaxis are used to probe beyond what is experimentally feasible and identify the extrinsic limits environmental parameters place on chemotactic performance. Finally, a simple theoretical model is used to explain how cell chemotactic accuracy and persistence is physically restricted to a specific performance range due to environmental factors.

2.1 Review of Chemotaxis Metrics

The literature on cell migration and chemotaxis experiments contains a variety of different metrics used to characterize cell motion. In this section we briefly review some of the more common metrics used for measuring cell motility, persistence (also referred to as directionality) and chemotactic performance. Common metrics from the literature and their definitions are explained in order to motivate the definitions used in our study.

2.1.1 Accuracy

For chemotaxis experiments, often a single metric referred to as the chemotactic index is reported to quantify how well cells track the chemoattractant in question. However, the mathematical definition of the chemotactic index (CI) varies throughout the literature, and here we review some of the more common ones. CI has been defined as the ratio of the distance traveled towards the chemoattractant to the distance traveled in the absence of chemoattractant [56], the ratio of the number of cells that migrate in response to a chemical to the number of cells that migrate in the absence of stimulus [57–59], and the population average of the cosine of the angle made between a cell’s displacement and the gradient direction [29, 60–62].

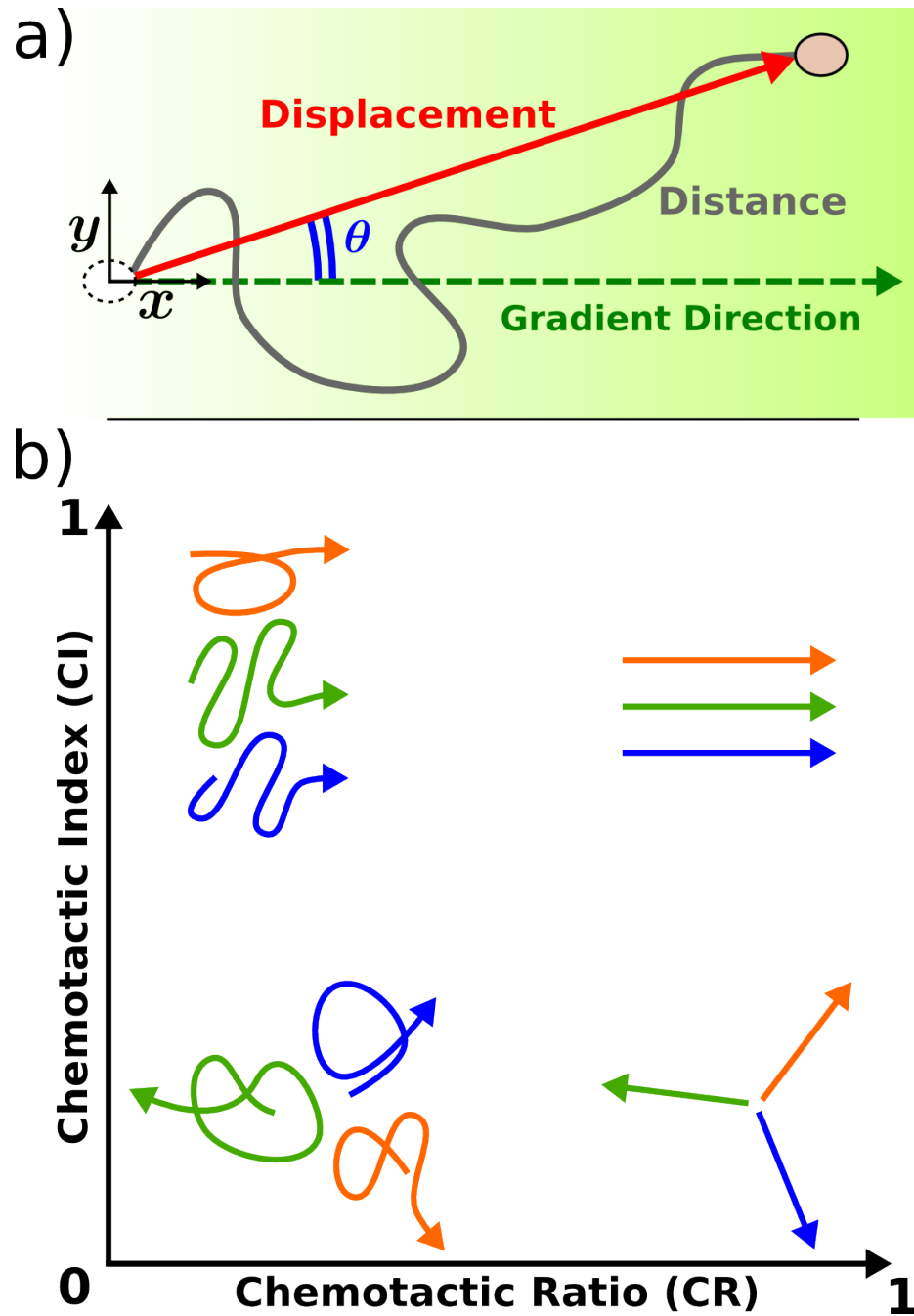


Fig. 2.1. a) Illustration of cell chemotaxis. The cell's displacement makes an angle θ with the gradient direction. b) Illustration of cell trajectories associated with different CI and CR values. Illustrations of typical cell trajectories are shown in different colors.

The former two ratio-based definitions are commonly found in the literature although comparing them between different experiments is difficult. Both definitions give a measure of the migratory response when cells are exposed to a certain chemical. In these cases $CI = 1$ corresponds to no chemotactic response and $CI > 1$ represents an increased response. They may confound the effects of chemkinesis and chemotaxis since the former induces cell motility but not necessarily directed migration. Furthermore, neither definition clearly characterizes the cell's accuracy in tracking the chemoattractant; instead they quantify a fraction of cells that respond to the chemical.

In this study we use the definition based on cosine of the angle cell trajectories make with the chemoattractant gradient direction as illustrated in Fig. 2.1a. Specifically, we define CI as the population average of the cosine of the angle made between a cell's displacement and the gradient direction [60–62],

$$CI \equiv \langle \cos \theta \rangle . \quad (2.1)$$

Strictly speaking, CI is bounded between -1 and 1, but for chemotaxis in response to a chemoattractant – as is the case in this study – CI generally falls between 0 and 1. $CI = 1$ represents perfectly accurate chemotaxis in which cell displacement is parallel to the gradient direction (Fig. 2.1b, top-half), and $CI = 0$ indicates that the cells' migration is unbiased (Fig. 2.1b, bottom-half). This metric is more easily comparable between experiments, and its bounded range makes it easier to get intuition for different values of CI.

2.1.2 Persistence

Cell migratory persistence is commonly quantified using the chemotactic ratio and the directional autocorrelation function. The chemotactic ratio (CR) is defined as the ratio of the cell's displacement to the total distance traveled (Fig. 2.1a):

$$CR \equiv \left\langle \frac{\text{displacement}}{\text{distance}} \right\rangle . \quad (2.2)$$

The CR metric goes by several names in the literature such as the McCutcheon index [63], directionality (ratio), length ratio [64], and straightness index [65]. CR is bounded between 0 and 1 and intuitive sense can be made of either limit. If $CR = 1$, then the cells are moving in perfectly straight lines and motion is optimally efficient (Fig. 2.1b, right-half). However, $CR = 0$ represents cell motion that is neither persistent nor efficient (Fig. 2.1b, left-half).

The directional autocorrelation function (AC) calculates on average, how much time must pass for the cell's current direction of motion to be independent from the direction it was going in the past [64, 66]. It quantifies persistence by calculating the timescale of decay in correlations between current and previous direction of motion. The AC is defined as

$$AC(\Delta t) = \langle \cos(\theta_{\Delta t+t} - \theta_t) \rangle_{t,N} , \quad (2.3)$$

where the average is taken over all starting times t and all N cell trajectories. The AC measures how the direction of cell motion is correlated with the direction of motion at a time Δt later. At $\Delta t = 0$, $AC(0) = 1$ since when no time has passed both angles in Eq. 2.3 are equal. In the opposite limit, $AC(\Delta t \rightarrow \infty) = 0$ since trajectories that occurred infinitely far apart in time should have no effect on each other. Calculating AC for all Δt times sets a timescale τ which quantifies the rate at which correlations decay from 1 to 0. Therefore τ quantifies the persistence in the cells motion, a larger τ is indicative of more persistent motion. We define τ as

$$\tau = \int_0^\infty dt' AC(t') . \quad (2.4)$$

The AC is useful for cross-comparing experiments since the persistence timescale τ is largely independent of the frequency at which measurements were taken as well as the total observation time.

We calculate the AC and its timescale τ from our experimental data. Fig. 2.2a shows the autocorrelations from the control assay, the black dots are the AC values for all times Δt observed in our experiment, and its AC has a timescale $\tau = 1.02$ hr. In Fig. 2.2b we compare the CR and AC timescale values from all experimental

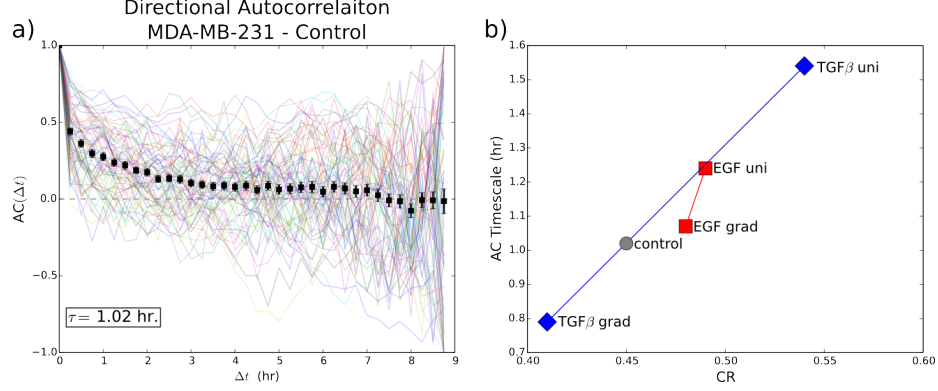


Fig. 2.2. a) Directional Autocorrelation from control dataset. Light-colored trajectories indicate autocorrelations for individual cell trajectories. Timescale τ is calculated using Eq. 2.4. b) Directional autocorrelation timescales and CR values for all experimental assays. Data points are color-coded based on chemical environment.

conditions. Going from a uniform to a graded concentration of either EGF or TGF β results in a decreased CR value, and the AC timescale also decreases when going from a uniform to a graded concentration. This indicates that there is a monotonic relationship between CR and τ . As the measured value of CR increases so too will the AC timescale τ .

Therefore, quantifying persistence with CR leads to the same patterns and analysis that could have been deduced from using AC. Additionally, the timescale obtained from the AC is not a bounded, dimensionless quantity. This makes gaining intuition about persistence from the autocorrelation timescale more difficult than CR. Since CR provides a clearer intuitive picture for persistence in cell chemotaxis we use it in our study.

2.1.3 Migration Speed

The final factor contributing to chemotactic performance is cell speed. Speed is important in order to ensure that the cells reach their destination in a timely manner.

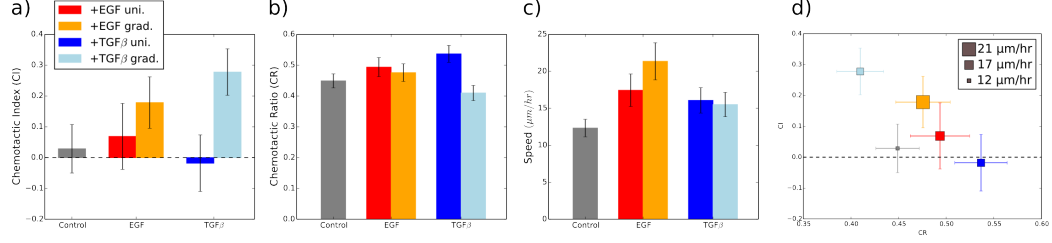


Fig. 2.3. [Plots a-c can be replaced with box-whisker style plots.] MDA-MB-231 cell chemotaxis assays. Cells are cultured in different chemical environments and trajectories are tracked. CI (a), CR (b) and mean speed (\bar{v}) are reported. d) Summary of chemotaxis assay results, data point size is proportional to mean speed. In all plots colors: no chemoattractant (gray), 400nM EGF uniform concentration (red), 0-800nM EGF gradient (orange), 25nM TGF β uniform concentration (blue), and 0-50nM TGF β gradient (light blue). Error bars are the standard error over the population of trajectories observed.

Cell speed is affected by many environmental factors such as collagen stiffness, and chemical concentration profiles. We define speed as the population average of the instantaneous cell speed during chemotaxis

$$\bar{v} \equiv \left\langle \frac{||\Delta\vec{r}||}{\Delta t} \right\rangle, \quad (2.5)$$

with Δt being the time lapsed between observations, and $||\Delta\vec{r}||$ the cell's displacement during that time period. Experimentally, measuring cell speed is limited by the frequency at which cell trajectories are recorded. Therefore comparison of cell speed recorded in different chemotaxis studies necessitates careful consideration of the procedures used in each respective study. Nonetheless, speed is a simple, easily digestible metric for quantifying how motile cells are during chemotaxis.

2.2 Experimental Results

We conducted experiments to measure the effects that the environment imposes on cell chemotaxis. Different chemicals known to induce motility and directed migration

were used to measure how chemotactic performance would change. Breast cancer cell line MDA-MB-231 was used in several different chemotaxis and motility assays.

[A more detailed description of the experimental setup and procedures needed.]

First, a control experiment was conducted to characterize the baseline behavior of the MDA-MB-231 cells (Fig. 2.3, gray bars). As expected, when the cells are not in the presence of a chemoattractant they do not migrate in any preferred direction as indicated by a chemotactic index centered around zero (Fig. 2.3a). However, even in the absence of any chemical signal cells do exhibit persistent motion with a $CR > 0$ (Fig. 2.3b), since the cell motion is intrinsically directional due to the cells' internal migratory machinery [9]. Similar persistent motion has been observed and modeled in the context of other cell types [65,67,68]. Finally, we characterize the baseline cell motility, with a speed of $\approx 12\mu\text{m/hr}$ (Fig. 2.3c).

What happens when chemicals are added to the external environment? We start by performing assays with epidermal growth factor (EGF). EGF is a known motility inducing agent [67,69] and may also bias cell migration [70]. Experiments are conducted for both a uniform 400nM concentration and gradient of 0-800nM across a 1mm-long chamber [Perhaps discuss spatio-temporal features of gradient profile here and/or in supplement]. As shown in Fig. 2.3a, adding a uniform concentration of EGF to the cellular environment results in a CI value within one standard error of $CI = 0$ indicative that the addition of EGF does not produce any significant bias to cell trajectories. This is expected since adding a uniform concentration of a chemical should not bias cell motion. On the other hand, adding a gradient of EGF does produce a CI that is significantly above zero meaning the breast cancer cells do chemotax in response to EGF (Fig. 2.3a). Examining the persistence and speed of cell movement (Fig. 2.3b-c) shows that the uniform concentration gives similar results to the graded concentration. We observe that adding EGF results in about a 6% increase in CR and an increased cell speed in agreement with the literature that EGF induces cell motility.

Next we used transforming growth factor type beta ($\text{TGF}\beta$) as a chemoattractant. $\text{TGF}\beta$ is a known chemoattractant for many cell types [71, 72]. It is also involved in development, inflammation, and may be involved in carcinogenesis [73–75]. Here we find that $\text{TGF}\beta$ is a strong chemoattractant (Fig. 2.3a, light-blue) with $\text{CI} = 0.278 \pm 0.075$ when a 0-50nM gradient is used. $\text{TGF}\beta$ does promote more directionally persistent motion as its CR value for a uniform concentration (but not for the graded concentration) is greater than that recorded for the control (Fig. 2.3b). Adding $\text{TGF}\beta$ to the cellular environment does improve cell speed, but not to the extent that was observed for motility-inducing EGF (Fig. 2.3c).

In summary, adding a gradient of EGF or $\text{TGF}\beta$ results in chemotaxis as indicated by CI values significantly above zero. The experimental parameters' affects on chemotactic behavior are consolidated into Fig. 2.3d. Movement in the CI-CR plane of Fig. 2.3d indicates changing persistence and accuracy of chemotaxis, whereas the size of each data point represents the average speed. Under all conditions the cells move at speeds of $\sim 10\mu\text{m/hr}$. An increase in speed is observed when the MD-MB-231 cells are exposed to either growth factor. This is not not a surprising result since chemical agents that promote persistent or directed migration often results in increased motility [9]. EGF and $\text{TGF}\beta$ both produce similarly persistent motion though EGF promotes more motility as indicated by its fastest cell speed.

2.3 Chemotaxis Simulations

The experiments tell us how cells respond to specific concentration profiles of EGF and $\text{TGF}\beta$. However, experiments do not tell us how chemotactic performance varies from experimental configuration to the next, and we are limited to testing conditions that experimentally feasible. Can we develop a model of chemotaxis that is capable of predicting chemotactic performance before doing experiments?

Here we conduct single cell chemotaxis simulations to further probe cell chemotactic performance. With simulations environmental parameters such as collagen

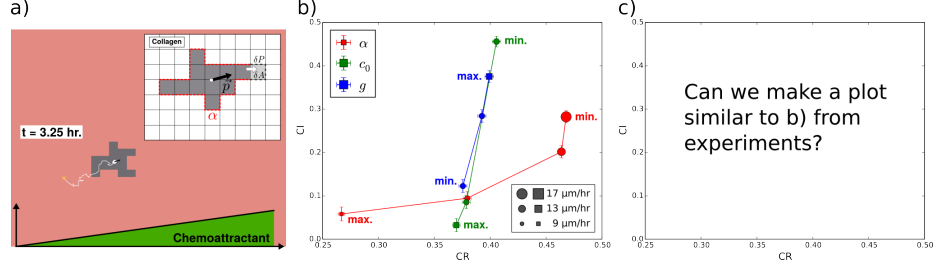


Fig. 2.4. a) Screen shot of simulation. Cell (gray) is migrating towards increasing chemical concentration, and the white line traces out the cell's path. Inset, illustration of the CPM. A Cell is comprised of simply connected lattice sites. There is an adhesion energy associated with cell-collagen contact, α (red-dashed line). Cell motility occurs through the addition/removal of lattice sites (light-gray). The white dot represents the cell's center of mass and the black arrow its polarization vector \vec{p} . b) Simulation results. Environmental parameters collagen stiffness α (red), background concentration c_0 (green), and gradient g are varied (blue). Parameter values along each trajectory: $\alpha \in \{0.1, 0.4, 0.7, 1.0\}$, $c_0 \in \{1.0, 10.0, 100.0 \text{ nM}\}$, $g \in \{1.0, 5.0, 10.0 \text{ nM}/\mu\text{m}\}$.

stiffness, background chemical concentration, and gradient can all be easily varied over a wide range of values which may not be experimentally practical. These experimental parameters are individually varied to develop predictions on how each parameter affects chemotactic accuracy (CI), persistence (CR), and speed.

2.3.1 Computational Implementation

Cell chemotaxis simulations are implemented using the Cellular Potts Model (CPM) [46,47]. The CPM used here is similar to that used in our previous study [76]. The source code for the simulations can be found here [CITE]. Briefly, the cell in the CPM are composed of a finite set of simply connected lattice sites $\{x\}$ (Fig. 2.4a, inset). Cell lattice sites are given the lattice label $\sigma(x) = 1$ whereas the extracellular environment is labeled $\sigma(x) = 0$. Cells have a desired size A_0 and perimeter P_0 from which they can fluctuate, and cells adhere to their neighboring environment

with an adhesion energy α . The energy of the whole system is the sum of adhesion, area-restriction, and perimeter-restriction terms,

$$u = \alpha N_p + \lambda_A (A_0 - N)^2 + \lambda_P (P_0 - N_p)^2 . \quad (2.6)$$

N_p is the number of lattice sites that comprise the cell's perimeter, N is the total number of cell lattice sites. The parameters λ_A and λ_P are the area and perimeter restriction costs.

Cell motion is a consequence of minimizing the energy of the whole system. This stochastic process is sensitive to thermal fluctuations and is modeled using a Monte Carlo scheme. In a system of n lattice sites, one *Monte Carlo* time step (MC step) is composed of n attempts to copy a random lattice site's label to a randomly chosen neighboring site. An attempt is accepted with probability P , which depends on the change in the system's energy Δu accrued in copying over the lattice label,

$$P = \begin{cases} e^{-(\Delta u - w)} & \Delta u - w > 0, \\ 1 & \Delta u - w \leq 0. \end{cases} \quad (2.7)$$

The bias term w acts to bias cell motion in the direction of its polarization, and is necessary in order for cells to exhibit directed motion [38]. The bias is defined as

$$w = \Delta \hat{x} \cdot \vec{p} , \quad (2.8)$$

with $\Delta \hat{x}$ the unit vector pointing in the change in the cell's center of mass caused by the addition or removal of the lattice site in question, and \vec{p} is the cell's polarization vector (Fig. 2.4a, black arrow). The dot product acts to bias cell motion since movement that is parallel to the polarization vector will result in a more positive w which in turn results in a higher acceptance probability (Eq. 2.7).

After the random addition and removal of lattice sites occurs during one MC step the cell updates its polarization vector. The time evolution of the cell's polarization vector is defined as

$$\frac{d\vec{p}}{dt} = -r\vec{p} + \Delta\vec{x} + \epsilon\vec{q} . \quad (2.9)$$

The first term in Eq. 2.9 results in exponential decay of the cell's current polarization at a rate r . Δx is the cell's displacement and it creates persistence in cell motion; \vec{p} is reinforced in the direction of motion. The third term represents chemotaxis, with ϵ the bias strength and \vec{q} an abstraction of the cell's gradient sensing.

$$\vec{q} = \frac{1}{N_P} \sum_{i=1}^{N_P} \frac{c_i - \bar{c}}{\bar{c}} \hat{r}_i \quad (2.10)$$

\hat{r}_i is a unit vector that points radially outwards from the cell's center of mass to the location of lattice site i . c_i is the concentration of the chemoattractant sampled at the lattice site i and \bar{c} is the cell's measurement of the mean concentration in its local environment; c_i is sampled from a Poisson distribution and \bar{c} is the mean from all c_i measured at each lattice site.

2.3.2 Calibration of Simulation Parameters

The length and time scales of the simulation are calibrated to the experimentally observed average cell size and speed over all assays. Internal cellular parameters, such as the cell polarization strength and decay rate, are then calibrated such that the simulation's CI and CR values are approximately the same as those observed in experiments.

From experiments we know that cells are on average $400\mu\text{m}^2$ in size, and we use this to set one lattice site to equal $5\mu\text{m}$ such that cells occupy ~ 10 lattice sites. Next we calibrate the time-scale in simulations by equating the average cell velocity in simulations to approximately that observed experimentally, $\sim 10\mu\text{m/hr}$. With this we equate a simulation time step to 5min. Finally, we need to calibrate the internal cell parameters. We consider internal cell parameters to be those which are not affected by the environment and are characteristic of the particular cell type we are simulating. These include the energy costs of cell area and perimeter fluctuations λ_A , λ_P , the polarization decay rate r , and the bias strength ϵ . These parameters are set such that the chemotactic index (CI) and chemotactic ratio (CR) recorded in experiments is approximately the same as that observed in experiments. We refer to

the collagen stiffness α , background concentration c_0 , and the concentration gradient g as experimental parameters.

In running simulations internal parameters are fixed to the values used for the initial calibration. External parameters are varied (as in Fig. 3 of the manuscript) in order to quantify their effects on chemotactic performance. The internal parameter values used as well as the baseline external parameter values are listed in Table 2.1.

Parameter	Value	Notes
Relaxed Cell Area A_0	$400 \mu\text{m}^2$	
Relaxed Cell Perimeter P_0	$3.6\sqrt{A_0} \mu\text{m}$	Assumes circular resting shape
Area Energy Cost λ_A	0.3	Prevents “stringy” cell-shapes
Perimeter Energy Cost λ_P	0.01	
Polarization Bias Strength ϵ	0.1	
Polarization Decay Rate r	2.4 hr^{-1}	Sets polarization memory time
Cell-environment Contact Energy α	0.7	Sets energy scale
Concentration \bar{c}	10 nM	
Gradient g	$0.5 \text{ nM}/\mu\text{m}$	

Table 2.1.

Table of parameters and values used in simulations. The first six parameters are intrinsic to the cell and remain fixed. The final three parameters represent the environment and are varied in Fig. 2.4. Energy costs are in units of $k_B T$, where $k_B T$ is the thermal energy of the CPM Monte Carlo scheme.

2.3.3 Simulation Results

With length and time scales of the simulation are calibrated and internal cellular parameters fixed, we vary the environmental parameters. Collagen stiffness α , background concentration c_0 , and gradient g are varied to study their effects on

chemotactic performance. Fig. 2.4b shows the resulting CI, CR and speed values when environmental parameters are changed. Each data point along a parameter's trajectory indicates the CI and CR values, while the size of the data point indicates the average speed for that particular choice of parameter value. All other parameters are held fixed along each trajectory. The background concentration is varied over three orders of magnitude whereas both the gradient and collagen stiffness are varied over one order of magnitude.

We find that varying the background concentration and gradient most significantly affects the accuracy of chemotaxis, not the persistence nor the speed. This is displayed in Fig. 2.4b in which both c_0 and g have much longer trajectories along the CI axis than along either the speed or CR axis. As the background concentration increases, the fluctuations in the diffusing chemoattractant become larger relative to the gradient making it more difficult for the cell to correctly determine the gradient direction. This results in a decreasing CI as c_0 increases. Conversely, increasing the gradient enables the cell to more accurately detect the gradient direction resulting in increasing CI values (Fig. 2.4b,c).

Along with changing the accuracy of chemotaxis, varying c_0 and g also results in slightly increased persistence and speed. This goes hand in hand with the improved gradient detection due to increased g or decreased c_0 . As cells become more accurate movements perpendicular to the gradient are reduced, resulting in more persistent and faster motion along the gradient direction as shown in Fig. 2.4b.

Collagen stiffness is the only parameter that significantly affects the persistence in the cell's motion, indicated by the larger displacement in α 's trajectory along CR versus CI or speed (Fig. 2.4a,b). Stiffer collagen is more difficult for cells to traverse leading to slower speeds, and we find a monotonic relationship between CR and speed when stiffness is varied (Fig. 2.4b). As was observed for the chemoattractant-related parameters the more persistent cell motion seen at small α also corresponds to more accurate, faster chemotaxis.

From these simulation results we deduce some stereotypical patterns of cell chemotaxis. Increasing the relative change in chemoattractant concentration across cell (either by increasing g or reducing c_0) results in more accurate chemotaxis. Material that is more difficult for cells to traverse during chemotaxis, whether its stiffer collagen *in vitro* or denser extracellular matrix *in vivo*, results in reduced chemotactic performance across all metrics. Finally, the simulations show a positive correlation between CR and speed since as cell motion becomes more persistent it typically also enables faster cell movement.

2.4 Theoretical Model of Chemotaxis

Interestingly, although both experiments [Similar plot for experiments? (Fig. 3c)] and simulations vary environmental parameters affecting cell chemotaxis, the chemotactic performance metrics do not dramatically change. Both CI and CR can range from 0 to 1, but our MDA-MB 231 cell assays result in CR values close to 0.45 and CI values less than 0.3 for all environmental conditions (Fig. 2.3). Simulations allow for probing chemotactic behavior over an even larger parameter space, and yet CI and CR values remain limited to a fraction of the whole range (Fig. 2.4).

Can this phenomenon be explained with a simple physical model? One of the simplest models for cell movement and chemotaxis is the biased persistent random walk [68, 77]. In its simplest form, a random walk involves a walker that is equally likely to move in any direction, and its next movement is independent of its previous motion. To add persistence to the random walk means that the walkers' movements are correlated. The walker's next movement is not equally likely in all directions as in the simplest case, but now depends on its previous direction of motion [78]. Finally, adding bias means that the walker is more likely to move in a particular fixed direction. Biased persistent random walks (BPRWs) have been used to model chemotaxis [68, 77]. Before we get into how the BPRW model can shed light on the

chemotactic performance of MDA-MB-231 breast cancer cells, lets review the model formulation.

2.4.1 BPRW Formulation

The BPRW is modeled as a velocity jump process in which a walker moves in a particular direction with fixed speed for an exponentially distributed amount of time. The walker reorients to a new direction \vec{v} from its previous velocity \vec{v}' depending on the probability density $T(\vec{v}, \vec{v}')$. We assume a reorientation frequency λ , thus λ^{-1} is the average run time, and that it moves at a constant speed s . The reorientations are chosen based on a probability density $T(\vec{v}, \vec{v}')$ which depends only on the angular direction of the walker's movements $T(\vec{v}, \vec{v}') = T(\theta, \theta')$. Here θ is taken relative to the x axis which is parallel to the gradient direction.

Let $p(\vec{r}, \theta, t)d\vec{r}d\theta$ be the number density of individual walkers found between positions \vec{r} and $\vec{r} + d\vec{r}$ with movement orientation between θ and $\theta + d\theta$. From Othmer *et al.* it is shown that the evolution equation for the probability density $p(\vec{r}, \theta, t)$ simplifies to

$$\frac{\partial p}{\partial t} + s\vec{\xi} \cdot \vec{\nabla} p = -\lambda p + \lambda \int_{-\pi}^{\pi} d\theta' T(\theta, \theta') p(\vec{r}, \theta', t), \quad (2.11)$$

with $\vec{\xi} = (\cos \theta, \sin \theta)$. In order to derive expressions for the moments some assumptions have to be made on the reorientation probability density. We assume that $T(\theta, \theta')$ is the sum of two functions,

$$T(\theta, \theta') = \underbrace{k(\theta)}_{\text{bias}} + \underbrace{h(\phi)}_{\text{persistence}} \quad (2.12)$$

with $\phi = \theta - \theta'$ being the turning angle. $k(\theta)$ is maximally valued and symmetric about $\theta = 0$, and biases movement towards the gradient. $h(\phi)$ is the turning angle

distribution which is assumed to be symmetric about $\phi = 0$. Along with these properties $T(\theta, \theta')$ and its component functions must obey the following conditions:

$$T(\theta, \theta') \geq 0, \text{ for all } (\theta, \theta'), \quad (2.13)$$

$$\int_{-\pi}^{\pi} d\theta T(\theta, \theta') = 1, \quad (2.14)$$

$$\int_{-\pi}^{\pi} d\theta k(\theta) = 0, \quad (2.15)$$

$$\int_{-\pi}^{\pi} d\phi h(\phi) = 1. \quad (2.16)$$

With Eq. 2.11 and the restrictions on $T(\theta, \theta')$ (Eq. 2.13-2.16), Othmer *et al.* derive the moments for the BPRW.

$$\langle r^2(t) \rangle = \frac{2s^2}{\lambda_0} \left[\left(1 - \frac{2\chi^2}{(1-\psi)^2} \right) t - \frac{\chi^2 t e^{-\lambda_0 t}}{(1-\psi)^2} + \frac{3\chi^2(1-\psi)^{-2} - 1}{\lambda_0} (1 - e^{-\lambda_0 t}) + \frac{\chi^2 \lambda_0 t^2}{2(1-\psi)^2} \right] \quad (2.17)$$

$$\langle x(t) \rangle = \frac{\chi}{1-\psi} s \left(t - \frac{1 - e^{-\lambda_0 t}}{\lambda_0} \right) \quad (2.18)$$

$$\langle y(t) \rangle = 0 \quad (2.19)$$

These results are derived with the assumption that individuals in the BPRW start at the origin with uniformly distributed initial orientations. The mean squared displacement (Eq. 2.17) and the mean walker location (Eq. 2.18-2.19) both depend on the parameters χ , ψ , and λ_0 . The bias strength (also referred to as the taxis coefficient) is represented by χ which is defined as

$$\chi \equiv \int_{-\pi}^{\pi} d\theta k(\theta) \cos \theta. \quad (2.20)$$

ψ represents the persistence strength (also referred to as the persistence index), and it is defined as

$$\psi \equiv \int_{-\pi}^{\pi} d\phi h(\phi) \cos \phi. \quad (2.21)$$

Note that the restrictions on the reorientation probability density (Eq. 2.13-2.16) result in $\chi \leq 1 - \psi$. Finally, λ_0 is the effective turning rate of the walker, $\lambda_0 \equiv \lambda(1 - \psi)$.

Since λ is the reorientation rate and ψ is the persistence strength, λ_0 describes the effective rate at which the walker forgets its previous orientation.

Starting from the definitions for CI and CR in Eqs. 2.1-2.2, we use the moments given in Eqs. 2.17-2.19 to calculate CI and CR for the BPRW model as functions of time:

$$\text{CI}(t) = \left\langle \frac{x}{r} \right\rangle \approx \frac{\langle x \rangle}{\sqrt{\langle r^2 \rangle}} = \chi \sqrt{\frac{\lambda}{2(1-\psi)}} \left(t - \frac{1 - e^{-\lambda_0 t}}{\lambda_0} \right) [\dots]^{-1/2}, \quad (2.22)$$

$$\text{CR}(t) = \frac{\langle r \rangle}{L} \approx \frac{\sqrt{\langle r^2 \rangle}}{st} = \frac{1}{t} \sqrt{\frac{2}{\lambda_0}} [\dots]^{1/2}. \quad (2.23)$$

The term $[\dots]$ is shorthand for the bracketed term in Eq. 2.17, and L is the total path length. In Eq. 2.22 we approximate the two moments as being independent of one another, and in both Eqs. 2.22-2.23 we make the approximation that $\langle x \rangle \approx \sqrt{\langle x^2 \rangle}$. These approximations are in very good agreement the exact solutions of CI and CR times in which many reorientation events occur, $t \gg \lambda^{-1}$. Note that neither CI nor CR depend on the speed s , and assuming that $\chi < 1 - \psi$, to first order CR decays as $\text{CR} \sim t^{-1/2}$.

The BPRW predictions for CI and CR depend on how strongly persistence and bias affect the walker's movements. The timescales in the BRPW are calibrated to those of our experiments; total observation time $t = 9\text{hr}$, the reorientation frequency $\lambda = 4\text{hr}^{-1}$, and we approximate the speed to be $s = 15\mu\text{m/hr}$. With the BPRW timescales calibrated we can proceed to vary $T(\theta, \theta')$ which in turn affects the bias strength χ , and the persistence strength ψ .

Simulations of the BPRW are performed with varying $T(\theta, \theta')$ to find the resulting values of CI and CR possible given our experimental system. In the simulations the bias and persistence functions to take on the forms:

$$k(\theta) = k_1 \cos \theta, \quad (2.24)$$

$$h(\theta - \theta') = h_1 f_{\text{VM}}(\theta | \theta', \kappa_1) + h_2 f_{\text{VM}}(\theta | \theta', \kappa_2). \quad (2.25)$$

Here k_1 sets the bias strength, and $h(\theta - \theta')$ is a linear combination of two von Mises distributions with $f_{\text{VM}}(\theta | \theta', \kappa) = \frac{1}{2\pi I_0(\kappa)} e^{\kappa \cos(\theta - \theta')}$. The von Mises distribution is

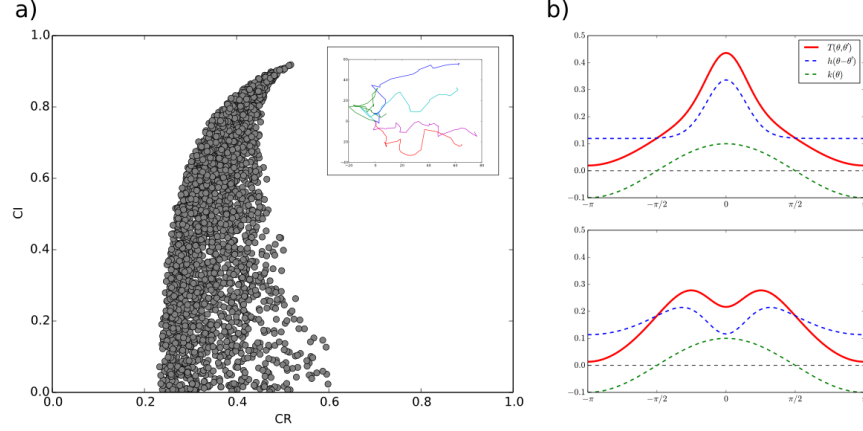


Fig. 2.5. a) Possible values of CI and CR for a BPRW. Each dot represents the CI and CR value for a BPRW of a given bias and persistence strength. Inset, sample trajectories of a BPRW. b) Example reorientation probability densities $T(\theta, \theta')$, and their component bias $k(\theta)$ and persistence $h(\theta - \theta')$ functions. For both b) plots $\theta' = 0$. For all plots: $t = 36$, $\lambda = 1.0$, $s = 3.75$, and $\theta = 0$ is the direction of bias.

approximately equal to a normal distribution bounded to a circle, and it is commonly used in random walk models of biological systems [65]. The parameters κ_1 and κ_2 set the persistence strength with larger values of κ resulting in higher persistence. h_1 and h_2 set the shape of the distribution, with $\{h_1, h_2\} > 0$ results in a single-peaked $h(\theta - \theta')$ function as shown in Fig. 2.5b, top. Whereas, if $h_1 > 0$ and $h_2 < 0$ then the resulting $h(\theta - \theta')$ function has two peaks, symmetric across $\theta = \theta'$ (Fig. 2.5b, bottom). Interestingly, even in this idealized model of chemotaxis the whole range of CI and CR values is not available to the BPRW. The mechanics of the random walk limit its performance resulting in behavior that cannot attain perfect accuracy (CI = 1), nor perfect persistence (CR = 1).

In summary, by calibrating BPRW to our experiments the parameters t , λ , and s are fixed. From here we can sample possible CI and CR values given a particular bias and persistence strength. By varying over all possible combinations of bias and persistence parameters while enforcing the restrictions on $T(\theta, \theta')$ (Eq. 2.13-2.14)

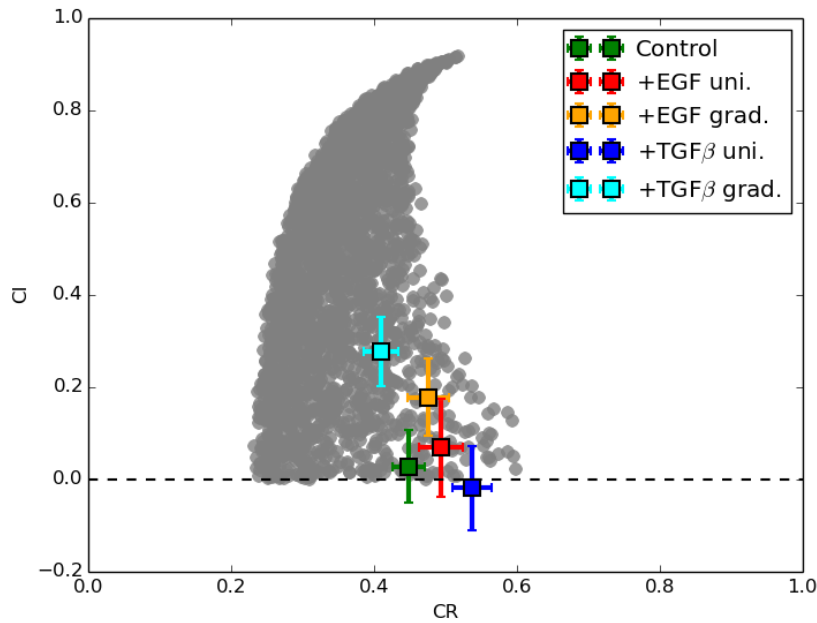


Fig. 2.6. Theoretical bounds on chemotactic performance based on the biased persistent random walk model. Gray dots represent possible theoretical CI and CR values for a BPRW. Colored squares are experimentally recorded values for different environmental conditions.

all possible values of CI and CR permitted under the BPRW model are calculated. The CI and CR values permitted by our theoretical model are shown alongside the experimental results in Fig. 2.6. We see that our simple theoretical model is able to recover the CI and CR values observed. More importantly, the BPRW puts limits on how well these breast cancer cells can chemotaxis regardless of how favorable the environmental conditions are made as represented by the gray-shaded region in Fig. 2.6.

3. LIMITS TO COLLECTIVE CHEMOTAXIS

In this chapter we transition from studying single-cell chemotaxis to that of multicellular collectives. Collective behavior occurs in a variety of biological systems such as organism development [11, 98–100], tissue morphogenesis [25] and metastatic invasion [22, 67, 90, 101]. Throughout these systems collective chemotaxis may occur in a variety of different ways. The simplest way for cells to collectively chemotax is by individual detection and response to the chemical attractant: each cell measures the gradient through the spatial difference in chemoattractant across its body and moves in the perceived direction of the gradient, while short-range coupling keeps the group together. Groups performing this type of *individual-based chemotaxis* (IC) are found not only in cell biology [102] but also in ecological systems such as bird flocks [41]. IC is sometimes referred to as “many wrongs”, as alluded to in Ch. 1. However, recent experiments have uncovered an alternative type of chemotaxis, in which cells grouped together chemotax differently than if they were alone [12, 79, 86, 103]. Interactions within the collective results in cell behavior which is unlike that of IC. For example, cells on the outer edges of the collective may polarize while inner cells do not, a mechanism observed in neural crest cells [11] and considered in several recent modeling studies [43, 76, 79]. This type of *emergent chemotaxis* (EC) behavior seen in cell collectives presupposes a machinery within cells which allows for behavior to change once a cell is in a group. Since this machinery may come at a cost, this raises the question of whether EC offers any fundamental advantage over IC.

We address this question using simple physical models of EC and IC. Cell collectives respond to graded profiles of freely diffusing molecules, and we quantify the migratory behavior of one-dimensional (1D) cell chains, two-dimensional (2D) cell sheets, and three-dimensional (3D) cell clusters [Fig. 3.1(a)], configurations designed to mimic physiological multicellular structures such as filaments and ducts [21, 90, 104].

The collectives exist at low Reynolds number, hence their velocity \vec{v} is proportional to the motility force, and in turn the polarization \vec{P} . Therefore, understanding the behavior of \vec{P} will inform us of the collective migratory performance. We focus on two measures of performance: the mean and the relative error of the polarization in the gradient direction P_z , where the relative error is defined

$$\epsilon^2 = \frac{\text{Var}[P_z]}{\langle P_z \rangle^2} = \frac{\text{Var}[v_z]}{\langle v_z \rangle^2}. \quad (3.1)$$

In either model, cells sense and polarize in response the chemoattractant diffusing in the environment. The chemoattractant concentration is a random variable of the form $c(\vec{r}, t) = c(0, t) + \vec{r} \cdot \vec{g}(\vec{r}, t)$, which obeys regular diffusion $\dot{c} = D\nabla^2 c + \eta_c$ with D the diffusion coefficient and η_c the Langevin noise due to the diffusive fluctuations in concentration [34, 105]. The mean concentration is $\bar{c}(\vec{r}) = c_0 + \vec{r} \cdot \vec{g}$, and first we consider a constant gradient $\vec{g} = g\hat{z}$ that is shallow ($ag \ll c_0$). Cells are assumed to preferentially adhere to one another, hence the polarization of a collective of N cells is the sum of its constituent cells' polarization vectors $\vec{P}(t) = \sum_{i=1}^N \vec{p}_i(t)$, although the exact form of \vec{p}_i will depend on the model. The cell polarization will fluctuate due to the particulate nature of diffusion. Focusing on this extrinsic source of noise, we treat each cell as a sphere of radius a through which molecules freely diffuse, akin to the “perfect instrument” described by Berg and Purcell [2].

Collectives performing EC and IC are found to have very similar mean speed, with polarization strength scaling linearly with the number of cells regardless of chemotactic mechanism or dimensionality. However, 1D and 2D EC collectives have higher chemotactic precision than IC collectives: we find that for N cells, the relative error in EC scales as $\{N^{-2}, N^{-3/2}, N^{-1}\}$ for 1D, 2D, and 3D, respectively, whereas in IC it scales as N^{-1} for any dimension. We explain the physical origin of this difference and discuss its implications.

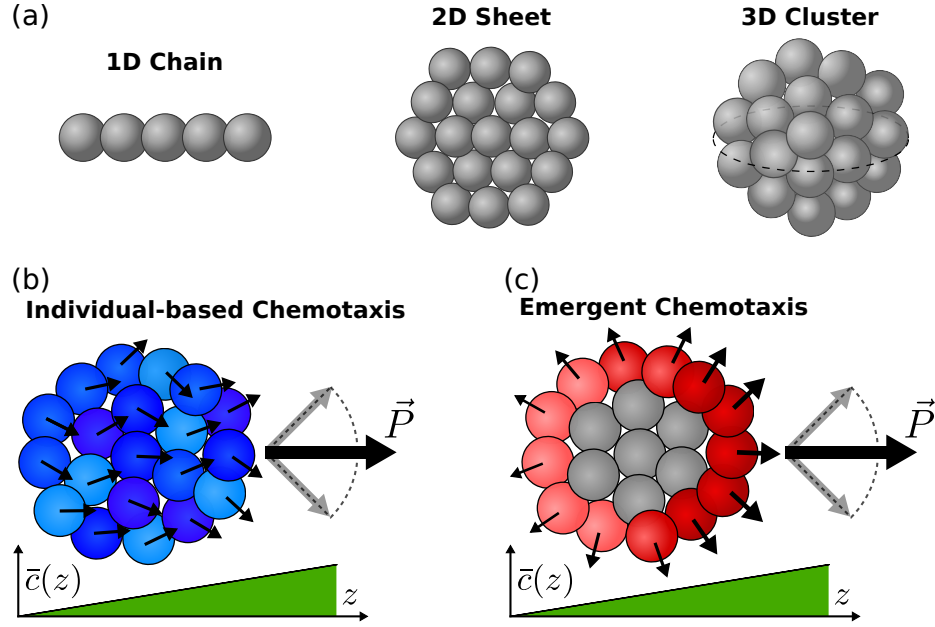


Fig. 3.1. (a) We study the chemotactic performance of 1D chains, 2D sheets, and 3D clusters of cells. (b) In individual-based chemotaxis (IC), cells in the collective polarize based on their own gradient measurement. (c) In emergent chemotaxis (EC), cell polarization depends on intercellular interactions: cells on the edge polarize based on their measurement of the concentration, and cells in the bulk do not polarize. In both mechanisms the total polarization \vec{P} will fluctuate in magnitude and direction due to noise in cell measurements.

3.1 Individual-based Chemotaxis

We first consider IC [Fig. 3.1(b)]. Due to the chemoattractant molecules in the environment, each cell i becomes polarized with vector \vec{p}_i in its desired direction of motion [10]. The components of \vec{p}_i reflect the difference in concentration $c(\vec{r}, t)$ between the front and back of the cell in each respective direction. The concentration difference is encoded internally as a weighted count of the molecules within the cell volume U_i . The weighting function will depend on the sensory network, but will generally be positive at the front and negative at the back; here we choose cosine for simplicity. Orienting our coordinate system such that \hat{z} is parallel to the gradient, the components of \vec{p}_i become

$$p_{i\alpha}(t) = \int_{U_i} d^3r w_\alpha c(\vec{r}, t), \quad (3.2)$$

where $\alpha \in \{x, y, z\}$, and in spherical coordinates the cosine is $w_\alpha = \{\sin \theta \cos \phi, \sin \theta \sin \phi, \cos \theta\}$.

To investigate $\langle P_z \rangle$ and ϵ^2 for the IC model, we first perform particle-based simulations of the chemoattractant in the presence of the permeable cells [107]. A complete description of the simulations used can be found in Section 3.5. We find that the total mean polarization $\langle \vec{P} \rangle$ points solely in the gradient direction with equal magnitude regardless of dimensionality [Fig. 3.2(a), blue data points]. Indeed, Eq. 3.2 indicates that a single cell will have mean polarization proportional to the concentration difference across the cell, $\langle \vec{p}_i \rangle = \pi a^4 g / 3 \hat{z}$, regardless of the cell's location. Therefore the mean collective polarization is geometry-independent, depending only on the number of cells present,

$$\langle \vec{P} \rangle_{\text{IC}} = \frac{\pi}{3} a^4 g N \hat{z}, \quad (3.3)$$

as shown in Fig. 3.2(a) (blue lines).

We next investigate the relative error for IC collectives. Simulations show that the error decreases with cluster size as $\epsilon^2 \sim N^{-1}$ for all three geometries [Fig. 3.2(b), blue data points]. This is the result that one would obtain if the cells were independent sensors, since both the mean and variance scale with N in that case [41]. However, they are not independent: their noise is correlated by fluctuations in the concentration

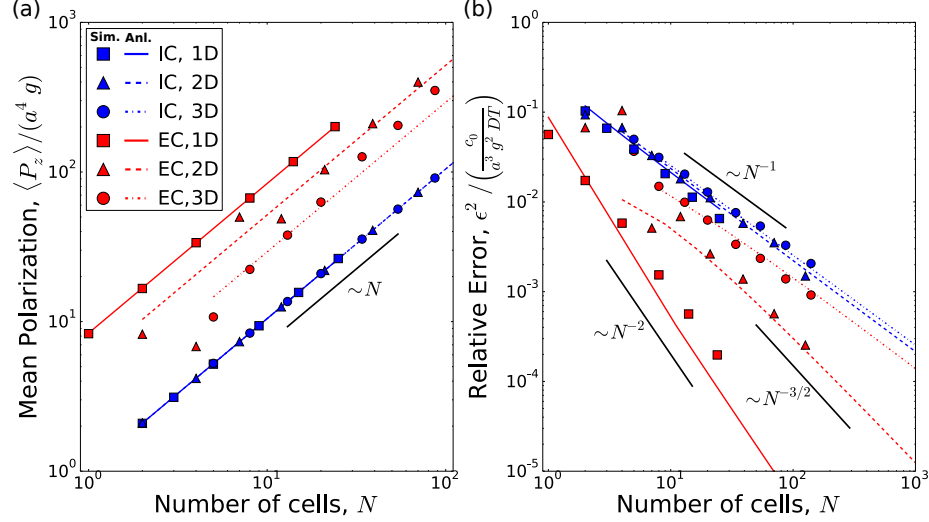


Fig. 3.2. (a) Mean cluster polarization and (b) relative error for both mechanisms of collective chemotaxis in every configuration. Points are simulation data, colored lines are analytical predictions. 1D EC data plotted with respect to $N - 1$.

[33,34]. To understand why correlations do not affect the relative error we investigate the model analytically.

We begin by linearizing the concentration $c(\vec{r}, t) = \bar{c}(\vec{r}) + \delta c(\vec{r}, t)$ as well as the cell polarization $\vec{p}_i(t) = \langle \vec{p}_i \rangle + \delta \vec{p}(t)$, and by Fourier transforming in both space and time we derive analytic expressions for $\text{Var}[P_z]$ and thereby ϵ^2 [106]. Since $P_z = \sum_{i=1}^N p_{iz}$, the variance in the total polarization is a linear combination of all cell polarization variances and covariances present in the collective,

$$\text{Var}[P_z] = \sum_i \text{Var}[p_{iz}] + \sum_{i \neq j} \text{Cov}[p_{iz}, p_{jz}] \equiv V + C, \quad (3.4)$$

The variance and covariance for cells within the collective are derived from the power spectrum in polarization cross correlations, taking the general form

$$\text{Cov}[p_{i\alpha}, p_{j\alpha}] = \frac{1}{T} \lim_{\omega \rightarrow 0} \int \frac{d\omega'}{2\pi} \langle \delta \tilde{p}_{i\alpha}^*(\omega') \delta \tilde{p}_{j\alpha}(\omega) \rangle, \quad (3.5)$$

with T the cell's measurement integration time and $\text{Var}[p_{i\alpha}] = \text{Cov}[p_{i\alpha}, p_{i\alpha}]$ [4,33,34].

Eq. 3.5 assumes that the integration time is larger than the timescale of molecule

diffusion over the radius R of the collective, $T \gg \tau_D = R^2/D$, though we relax this assumption in later simulations. Following this procedure we find that V and C for IC are [106]

$$V_{\text{IC}} = \frac{4\pi a^5 c_0}{45DT} N, \quad (3.6)$$

$$C_{\text{IC}} = -\frac{\pi a^5 c_0}{18DT} \sum_{i \neq j}^N \frac{3 \cos^2 \Theta_{ij} - 1}{n_{ij}^3}. \quad (3.7)$$

Here n_{ij} is the number of cell radii separating the centers of cells i and j , and Θ_{ij} is the angle between the gradient direction and a line connecting the two cells. A detailed derivation of these analytic results can be found in Section 3.6.

V_{IC} scales with N since each cell is involved in gradient sensing and in turn polarizes. On the other hand, Eq. 3.7 reveals an angular dependence on the correlations between two IC cells. A pair of cells can be correlated or anti-correlated depending on their locations relative to the gradient. For example, if a pair of cells is parallel to the gradient then $\cos^2 \Theta_{ij} = 1$, resulting in a negative covariance, indicating that their gradient measurements are anti-correlated. In contrast, if two cells are perpendicular to the gradient then $\cos^2 \Theta_{ij} = 0$, resulting in a positive covariance and correlations between the two cells. The resulting contribution of C_{IC} to $\text{Var}[P_z]$ is dimensionality-dependent since the angles made between pairs of cells is determined by geometry, whereas V_{IC} is dimension-independent.

For a 1D chain of IC cells, every pair is parallel to the gradient resulting in anti-correlated measurements which we find in total scale as N [106]. As dimensionality increases, more and more pairs of cells will be perpendicular to the gradient resulting in reduced anti-correlations in the collective. This culminates in 3D clusters having zero cell-cell covariance contribution to the total cluster variance [106]. The result is that $\epsilon^2 \sim N^{-1}$ regardless of dimensionality, indicating that IC cells behave as effectively independent gradient sensors, even though there are diffusion-mediated cross-correlations between cells. The scalings for V and C are summarized in Table 3.1. The resulting ϵ^2 predictions are plotted in Fig. 3.2(b) (blue lines), and we see excellent agreement with the simulations.

		$\langle P_z \rangle$	V	C	ϵ^2
IC	1D	N^1	N^1	$-N^1$	N^{-1}
	2D	N^1	N^1	$-N^1$	N^{-1}
	3D	N^1	N^1	0	N^{-1}
EC	1D	N^1	N^0	$-N^{-1}$	N^{-2}
	2D	N^1	$N^{1/2}$	$N^{1/2}$	$N^{-3/2}$
	3D	N^1	$N^{2/3}$	N^1	N^{-1}

Table 3.1.

Summary of scaling behavior. N dependence of the leading order term for the mean $\langle P_z \rangle$, and the variance (V) and covariance (C) contributions to the relative error $\epsilon^2 = (V + C)/\langle P_z \rangle^2$. C for EC in 2D has a log correction [106].

3.2 Emergent Chemotaxis

Next we turn our attention to EC, the mechanism in which grouped cells sense and migrate differently than individuals. Often cells in a cluster differentiate, with edge cells polarized and bulk cells unpolarized [79, 98]. In accordance with previous studies [43, 76], we assume that cell interactions are mediated by contact inhibition of locomotion [44]. The interactions result in edge cells polarized away from their neighbors, and interior cells that remain uninvolved in chemical sensing and do not polarize [Fig. 3.1(c)]. The edge cells polarize with strength proportional to the local concentration which, again like Berg and Purcell's perfect instrument [2], is estimated

by counting the molecules present within their cell volume. Hence we define the polarization of the i th cell in the collective as

$$\vec{p}_i(t) = \begin{cases} \hat{r}_i \int_{U_i} d^3r \, c(\vec{r}, t) & i \in \{N_{\text{edge}}\} \\ 0 & i \in \{N_{\text{bulk}}\} \end{cases}, \quad (3.8)$$

where \hat{r}_i points radially outwards from the collective, and U_i is the cell volume. Eq. 3.8 dictates that \vec{p}_i is dependent on a cell's location relative to the collective. As illustrated in Fig. 3.1(c), only the cells on the edge sense the chemoattractant, polarizing with a larger magnitude on the high concentration side of the collective. The total polarization depends only on the cells along the edge: $\vec{P} = \sum_i \vec{p}_i$, $\forall i \in \{N_{\text{edge}}\}$.

Simulations for EC show that the mean polarization $\langle P_z \rangle$ scales with N for all geometries [Fig. 3.2(a), red points] even though N_{edge} is dependent on the dimensionality of the collective. Our analytical solution helps us understand this result. For 1D EC, only the two opposing cells are polarized so $\langle \vec{P} \rangle$ can be solved for exactly, but for 2D and 3D we take the continuum limit of $\vec{P} = \sum_i \vec{p}_i$, assuming the collective is much larger than a single cell $R \gg a$ [106]. The resulting expressions are

$$\langle \vec{P} \rangle_{\text{EC}} = f_d a^4 g N \hat{z}, \quad (3.9)$$

where the prefactors are $f_d = \{8\pi/3, 2\pi^2/3, 16\pi/9\}$ for $d = \{1, 2, 3\}$ dimensions, and for $d = 1$ we have taken $N - 1 \rightarrow N$ for large N . Eq. 3.9 is shown in Fig. 3.2(b) (red lines), and we see good agreement. $\langle P_z \rangle$ scales with N because it depends on the product of $N_{\text{edge}} \sim N^{(d-1)/d}$ and the distance spanned in the gradient direction by the collective $R \sim N^{1/d}$, resulting in a mean polarization which is geometry invariant [79].

Comparing EC and IC shows that $\langle P_z \rangle \sim N$ regardless of collective migration mechanism or geometry as seen in Fig. 3.2(a). $\langle P_z \rangle$ has the same parameter dependency for both EC and IC, namely $a^4 g$, which is the average change in the number of chemoattractant molecules across a cell. Although $\langle P_z \rangle_{\text{EC}} \approx 6 \langle P_z \rangle_{\text{IC}}$ meaning that EC speed is faster than IC, this relatively small difference may be difficult to detect

in biological systems. Moreover, both mechanisms have the same N scaling. Does the same equivalence between EC and IC also hold for the relative error?

Interestingly, simulations show that the EC relative error does depend on geometry and in fact outperforms IC in terms of scaling in 1D and 2D [Fig. 3.2(b), red points]. Only in 3D does the relative error appear to scale the same as IC. In order to understand the dimension dependence of the EC relative error we again investigate the model analytically. Following the procedure outlined by Eqs. 3.4 and 3.5 we find analytic expressions for $\text{Var}[P_z] = V + C$ for EC,

$$V_{\text{EC}} = \frac{16\pi a^5 c_0}{15DT} \sum_{i=1}^{N_{\text{edge}}} \cos^2 \Theta_i, \quad (3.10)$$

$$C_{\text{EC}} = \frac{8\pi a^5 c_0}{9DT} \sum_{i \neq j}^{N_{\text{edge}}} \frac{\cos \Theta_i \cos \Theta_j}{n_{ij}}, \quad (3.11)$$

with Θ_i the angle \hat{r}_i makes with the gradient. Again, a detailed derivation of these results can be found in Section 3.6. Both V_{EC} and C_{EC} depend on dimensionality simply because $N_{\text{edge}} \sim N^{(d-1)/d}$. From Eqs. 3.10 and 3.11 we see that $V \sim N_{\text{edge}}$, and that C depends on the angles edge cells make with the gradient. The angular dependence means that cells along the front and back sides of the cluster (relative to the gradient) are strongly anti-correlated since $\cos \Theta_i \cos \Theta_j \approx -1$, whereas pairs of edge cells near the middle are very weakly correlated ($\cos \Theta_i \cos \Theta_j \approx 0$). Unlike in the case of IC, the scaling of C with N increases with dimensionality as summarized in Table 3.1, and the resulting ϵ^2 predictions show good agreement with the simulation results [Fig. 3.2(b)].

The dimension dependence of the EC relative error can be understood by thinking of the collective as one large detector whose sensory surface is comprised of two halves. If both halves were to take measurements of their local concentrations and then polarize in opposing directions with strengths proportional to their measurements, then ϵ^2 would depend on the size of each half a_{eff} and their separation distance A_{eff} according to $\epsilon^2 \sim a_{\text{eff}}^{-1} A_{\text{eff}}^{-2}$ [33]. The size of each half is independent of N for a 1D chain (each half is a single cell), but it scales as $a_{\text{eff}} \sim N^{1/d}$ for $d = 2$ or 3 dimensions.

The separation distance scales with the radius of the collective in all dimensions, $A_{\text{eff}} \sim N^{1/d}$. This results in $\epsilon^2 \sim \{N^{-2}, N^{-3/2}, N^{-1}\}$ for $d = \{1, 2, 3\}$ [Fig. 3.2(b), black lines], which agree with the scalings seen in simulations and analytics.

Thus, the physical origin of the advantage of EC over IC lies in how the errors scale with the collective size N . In IC, all N cells contribute to the sensing, and cross-correlations between them scale either linearly or sublinearly with N , leading to a scaling $\epsilon^2 \sim 1/N$ that is characteristic of independent sensors. But in EC, only $N_{\text{edge}} \sim N^{(d-1)/d}$ cells contribute to the sensing, leading to a sublinear scaling with N of the variance contributions of the individual cells. The total variance of the collective, then, depends on the cross-correlations, which are geometry-specific: in 1D they are dwarfed by the individual variances, in 2D they are commensurate, and in 3D they dominate (Table 3.1). As a result, 1D and 2D EC collectives benefit from a variance that scales subextensively, i.e., sublinearly with N .

3.3 Model Extensions

Our analytical treatment relies on several assumptions which we now relax using the simulations. In Fig. 3.2 the integration time T is larger than the timescale for molecule diffusion τ_D . We relax the assumption that the integration time T must be larger than the timescale for diffusion $\tau_D \sim R^2/D$ [Fig. 3.3(a)]. We find that ϵ^2 scales the same way as previously predicted for both EC and IC, even when $T = \tau_D/100$. The only exception is that ϵ^2 for 3D EC [Fig. 3.3(a), red circles] has a more negative power-law dependence on N than the expected $\sim N^{-1}$. The shorter integration time results in decreased correlations between edge cells which when $T > \tau_D$ results in $C \sim N$. Hence with $T < \tau_D$ the total variance is less dependent on C , and $V \sim N^{2/3}$ becomes the dominant contribution to $\text{Var}[P_z]$ in the case of 3D EC. This results in a steeper scaling of ϵ^2 closer to $\text{Var}[P_z]/\langle P_z \rangle^2 \sim N^{2/3}/N^2 = N^{-4/3}$. Interestingly, we see that relaxing the assumption $T \gg \tau_D$ results in improved precision for EC over IC not just in 1D and 2D but also in 3D configurations.

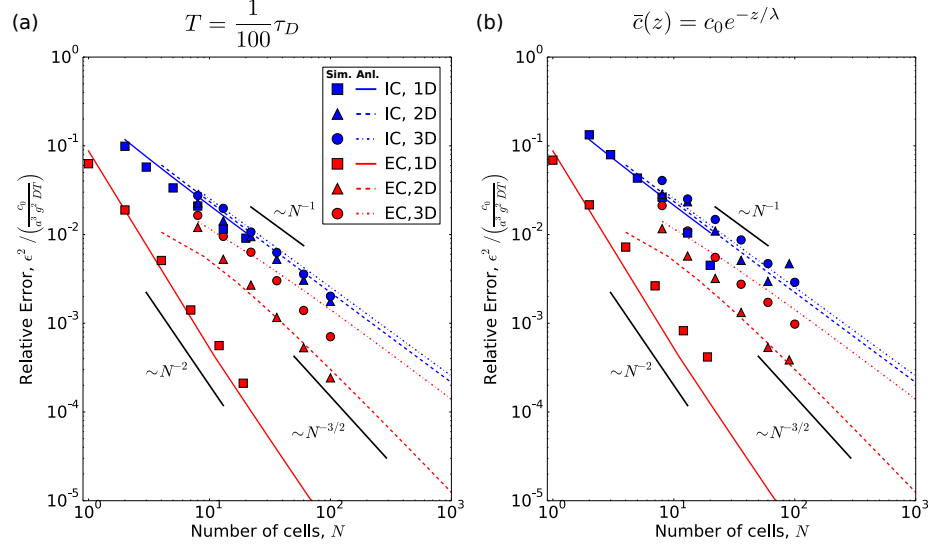


Fig. 3.3. (a) Short-time integration relative error results. Data points are of simulations for $T = \frac{1}{100}\tau_D$. (b) Exponential concentration profile relative error results. The mean concentration profile is $\bar{c}(z) = c_0 e^{-z/\lambda}$, the lengthscale $\lambda = \sqrt{D/\beta}$ is set by the diffusion coefficient D and the molecule decay rate β . Lines are from original analytical predictions using $T > \tau_D$ and a linear concentration profile.

In Fig. 3.3(b) we change the concentration profile from linear to exponential which has a mean concentration of $\bar{c}(z) = c_0 e^{-z/\lambda}$. The lengthscale $\lambda = \sqrt{D/\beta}$ depends on the diffusion coefficient and the molecule degradation rate β . In Fig. 3.3(b) the simulation results are for $\lambda > a$. We find that ϵ^2 is in very good agreement with our original analytic predictions. The only exception is that due to the exponential profile, $\langle P_z \rangle$ for 1D EC (Fig. 3.3(b), red squares) is non-linear in N causing the relative error data to scale less steeply than the expected N^{-2} .

In our model, IC polarization is adaptive to the background concentration as observed in the Ras signalling pathway for *Dictyostelium discoideum* chemotaxis [108]. On the other hand, our EC model is non-adaptive. Cell polarization increases with background concentration causing tension in the collective [Fig. 3.1(c)], as previously studied [43]. However, adaptive collective sensing has been observed in mammary

epithelial cells [25]. Our EC model could be made adaptive by replacing the integrand in Eq. 3.8 with $c(\vec{r} + \vec{r}', t) - c_0$. This change does not affect the properties of \vec{P} since the background concentration cancels out when summing over all edge cells, but it does remove the internal tension in the collective.

3.4 Discussion

Besides the advantage revealed here in terms of chemotactic precision, another benefit of EC is in terms of cell differentiation. In EC only edge cells need to be involved in chemical sensing and polarization, freeing bulk cells from the obligation of receptor and protein production necessary for chemotaxis. Bulk cells are free to differentiate into other phenotypes, possibly serving different uses for the collective. This is in stark contrast with IC where every cell must be of the polarized phenotype, leaving no cells with the freedom to differentiate.

The two EC advantages of improved chemotactic precision and the possibility of cell differentiation may be why EC-style collective migration is more prevalent than IC. For example, EC has been observed in two dimensional collectives of malignant lymphocytes [79] and in border cell migration [98]. In cancer, metastatic invasion sometimes occurs in the form of chains of cells leaving the tumor with a leader cell at the front [21, 90], analogous to our 1D EC model. Two-dimensional EC migration may also be implicated in tumorigenesis and metastasis in pancreatic ductal cells given the cylindrical surface-like geometry of pancreas ducts [104].

How can our predictions be tested in experiments? The chemotactic index (CI), commonly defined as $CI \equiv \langle \cos \theta \rangle$ where θ is the angle between the trajectory and the gradient [29], is actually a simple monotonic function of ϵ^2 . For small deviations from perfect chemotaxis, we have $CI \approx 1 - \langle \theta^2 \rangle / 2 = 1 - \text{Var}[\theta] / 2$. If v_z and v_x are the components of the velocity of the collective parallel and perpendicular to the gradient, respectively, then $\theta \approx v_x / v_z$ with $\langle v_z \rangle > 0$ and $\langle v_x \rangle = 0$, resulting in $\text{Var}[\theta] = \text{Var}[v_x] / \langle v_z \rangle^2 = \epsilon^2$. Therefore the relative error and chemotactic index are

related as $CI = 1 - \epsilon^2/2$ for small errors. With this relationship the predicted scalings of ϵ^2 for EC and IC may be tested with chemotaxis experiments. Additionally, the CI scaling behavior could be used to determine whether an EC- or IC-style migration is at play in a system of collective chemotaxis.

We have shown how the fluctuations in a diffusing attractant concentration set physical limits to collective chemotactic performance. By focusing on two fundamental classes of collective chemotaxis, we have found that the mean speed scales with the size of the collective irrespective of the mechanism or geometry, but that an emergent mechanism outperforms an individual-based one for 1D and 2D geometries in terms of chemotactic precision. This advantage arises due to the ways that errors accumulate in the two mechanisms: in an emergent strategy, fewer cells contribute their sensory noise to the collective, and in 1D and 2D the cross-correlations between cells remain low, ultimately leading to a subextensive scaling of polarization variance with collective size. As such, the performance advantage is an inherent property of the emergent mechanism, and we suspect that it not only helps explain the prevalence of emergent chemotaxis in cellular systems, but that it also is detectable using standard measures such as the chemotactic index.

3.5 Description of Simulations

Computational simulations are performed to test the properties of EC and IC for one, two and three dimensional collectives. In the simulation, particles move randomly inside a 3D volume and boundaries are set to produce the desired concentration profiles. Cells are placed at fixed positions in the 3D volume in either one, two or three dimensional configurations. For a linear concentration profile, one boundary produces particles, and the opposing one is an absorbing boundary while all other boundaries periodic. For an exponential concentration, the same boundaries are used and particles are also allowed to degrade.

At each time-step of the simulation particles randomly move and are produced. In a given time-step particles move in a random direction with a probability $p = D\Delta t/b^2$, with b the particle hopping distance, D the diffusion coefficient, and Δt the time-step. A particle is produced during that time-step with probability $q = k\Delta t$, with k the production rate. The time-step Δt is set such that $p + q \leq 1$. In the case of an exponential concentration profile, particles may also degrade during a time-step. Particles degrade with probability $r = \beta\Delta t$, with β the degradation rate. In this case Δt is set such that $p + q + r \leq 1$.

The simulation code used for this paper can be found at <https://doi.org/10.5281/zenodo.401040>, and the most up-to-date version of the code can be found at <https://github.com/varennnes/particletrack>.

3.6 Derivation of Analytic Results

We consider collectives in one, two and three dimensions of radius R comprised of N cells. Each cell is taken to be a permeable sphere of radius a through which molecules of the surrounding chemical concentration $c(\vec{r}, t)$ can freely diffuse. The chemical concentration is taken to be

$$c(\vec{r}, t) = c(0, t) + \vec{r} \cdot \vec{g}(\vec{r}, t) \quad (3.12)$$

with \vec{g} parallel to the z axis. The chemical concentration obeys normal diffusion

$$\dot{c} = D\nabla^2 c + \eta_c \quad (3.13)$$

with D the diffusion coefficient, and η_c the Langevin noise due to fluctuations in concentration. We linearize the concentration $c(\vec{r}, t) = \bar{c}(\vec{r}) + \delta c(\vec{r}, t)$ with

$$\bar{c}(\vec{r}) = c_0 + \vec{r} \cdot \vec{g} \quad (3.14)$$

where c_0 is the mean concentration at the origin. The Langevin noise term η_c , and the Fourier transformed fluctuation in the concentration $\delta\tilde{c}(\vec{k}, \omega)$ have the following properties (see Ref. [23] of the main text):

$$\langle \tilde{\eta}_c(\vec{k}', \omega') \tilde{\eta}_c(\vec{k}, \omega) \rangle = 2D \, 2\pi\delta(\omega - \omega') \int d^3y \, \vec{k} \cdot \vec{k}' \, \bar{c}(\vec{y}) \, e^{i\vec{y} \cdot (\vec{k} - \vec{k}')} , \quad (3.15)$$

$$\langle \delta\tilde{c}(\vec{k}', \omega') \delta\tilde{c}(\vec{k}, \omega) \rangle = \frac{\langle \tilde{\eta}_c(\vec{k}', \omega') \tilde{\eta}_c(\vec{k}, \omega) \rangle}{(Dk'^2 - i\omega)(Dk'^2 + i\omega')} . \quad (3.16)$$

Next, we define the cell polarization vectors for individual-based chemotaxis (IC) and emergent chemotaxis (EC). Collectives of N cells form shapes of different dimensionality: a chain of cells of length $2R$ (1D), a disc of cells with radius R (2D), and a sphere of cells of radius R (3D).

3.6.1 Individual-based Chemotaxis

In the IC mechanism, cells independently measure the chemoattractant gradient in order to set their polarization vector \vec{p} . For a spherically-shaped cell with volume U_i , \vec{p}_i is defined as

$$p_{i\alpha}(t) = \int_{U_i} d^3r \, w_\alpha c(\vec{r}, t), \quad (3.17)$$

where $\alpha \in \{x, y, z\}$, and in spherical coordinates the cosine is $w_\alpha = \{\sin \theta \cos \phi, \sin \theta \sin \phi, \cos \theta\}$.

The x, y, z components are written as

$$p_{ix}(t) = \int d\Omega' \, \sin \theta' \cos \phi' \int_0^a dr' \, r'^2 \, c(\vec{r}_i + \vec{r}', t) \quad (3.18)$$

$$p_{iy}(t) = \int d\Omega' \, \sin \theta' \sin \phi' \int_0^a dr' \, r'^2 \, c(\vec{r}_i + \vec{r}', t) \quad (3.19)$$

$$p_{iz}(t) = \int d\Omega' \, \cos \theta' \int_0^a dr' \, r'^2 \, c(\vec{r}_i + \vec{r}', t), \quad (3.20)$$

where $d\Omega' = \sin \theta' d\theta' d\phi'$. The r' coordinates are relative to the center of the respective cell, and the r_i coordinates are relative to the center of the collective. Using the mean

concentration (Eq. 3.14) with a constant gradient $\vec{g} = g\hat{z}$, we calculate the mean polarization of a single cell:

$$\begin{aligned}\langle p_{iz} \rangle &= \int d\Omega' \cos \theta' \int_0^a dr' r'^2 \bar{c}(\vec{r}_i + \vec{r}') \\ &= \int_0^a dr' r'^2 \int d\Omega' \cos \theta' (c_0 + gr_i \cos \theta_i + gr' \cos \theta') \\ &= \frac{\pi}{3} a^4 g .\end{aligned}$$

The means for the x and y components are $\langle p_{ix} \rangle = \langle p_{iy} \rangle = 0$ since they are perpendicular to the gradient. On average, cells performing IC migration will only polarize in the z direction. The mean for a collective of IC cells is

$$\langle \vec{P} \rangle = \frac{\pi}{3} a^4 g N \hat{z} . \quad (3.21)$$

3.6.2 Emergent Chemotaxis

In EC, cells along the edge of the cluster polarize outwards, whereas cells in the interior are not involved in chemical sensing and remain unpolarized:

$$\vec{p}_i(t) = \begin{cases} \hat{r}_i \int_{U_i} d^3r c(\vec{r}, t) & i \in \{N_{\text{edge}}\} \\ 0 & i \in \{N_{\text{bulk}}\} , \end{cases} \quad (3.22)$$

where \hat{r} points radially outwards from the collective. In order to break down $\vec{p}_i(\vec{r}, t)$ into component vectors we must be mindful of the dependence of \hat{r}_i on the cell location. For an edge cell the unit vector \hat{r}_i points in the direction of the cell's location in the collective, $\hat{r}_i = \sin \Theta_i \cos \Phi_i \hat{x} + \sin \Theta_i \sin \Phi_i \hat{y} + \cos \Theta_i \hat{z}$ where Θ_i is the polar angle made with the gradient direction and Φ_i is the azimuthal angle along the collective. The cell component vectors are

$$p_{ix}(t) = \sin \Theta_i \cos \Phi_i p_i(t), \quad (3.23)$$

$$p_{iy}(t) = \sin \Theta_i \sin \Phi_i p_i(t) , \quad (3.24)$$

$$p_{iz}(t) = \cos \Theta_i p_i(t) , \quad (3.25)$$

with $p_i(t) = \int_{U_i} d^3r \, c(\vec{r}, t)$ and $i \in \{N_{\text{edge}}\}$. The total polarization of the collective, $\vec{P} = \vec{P}_x + \vec{P}_y + \vec{P}_z$, is a sum of all the component vectors:

$$P_x(t) = \sum_i^{N_{\text{edge}}} \sin \Theta_i \cos \Phi_i p_i(t) , \quad (3.26)$$

$$P_y(t) = \sum_i^{N_{\text{edge}}} \sin \Theta_i \sin \Phi_i p_i(t) , \quad (3.27)$$

$$P_z(t) = \sum_i^{N_{\text{edge}}} \cos \Theta_i p_i(t) . \quad (3.28)$$

For an edge cell, the mean polarization is equal to the average number of molecules the cell counts within its spherical body:

$$\begin{aligned} \langle \vec{p}_i \rangle &= \int_{U_i} d^3r \, \bar{c}(\vec{r}) \, \hat{r}_i \\ &= \frac{4\pi}{3} a^3 (c_0 + gR \cos \Theta_i) \, \hat{r}_i , \end{aligned}$$

where Θ_i is the angle the cell's location makes with the gradient direction. The mean for a cluster of EC cells will depend on the dimensionality of the cluster. For a 1D chain of cells, only the two cells on the opposite ends of the chain are polarized, and $\langle P \rangle$ is the difference in the mean number of molecules counted in between the two edge cells:

$$1\text{D} : \langle \vec{P} \rangle = \frac{8\pi}{3} a^4 g (N - 1) \, \hat{z} . \quad (3.29)$$

In order to calculate the mean total polarization for two and three dimensional clusters we assume that the cluster size is relatively large ($a \ll R$) and approximate the sum as an integral. For a 2D disc of cells the sum $\vec{P} = \sum_i^{N_{\text{edge}}} \vec{p}_i$ becomes an integral over the circumference of the cluster. The circumference and the total number of cells along the edge are related by $2\pi R = 2aN_{\text{edge}}$, and so a segment along the perimeter of length $R\theta$ is equivalent in length to $2an$ with n the number of edge cells in that segment. Hence $n = \frac{R}{2a}\theta$ allowing us to write integrals for $\vec{P}(t)$ as

$$\vec{P}(t) = \frac{R}{2a} \int_0^{2\pi} d\theta \, \vec{p}_i(t) . \quad (3.30)$$

The mean polarization will point only in the z direction with magnitude

$$\langle P_z \rangle = \frac{R}{2a} \int_0^{2\pi} d\theta \langle p_z \rangle = \frac{R}{2a} \int_0^{2\pi} d\theta \cos \theta \left(\frac{4\pi}{3} a^3 (c_0 + gR \cos \theta) \right) = \frac{2\pi^2}{3} a^2 g R^2 .$$

Using the relation $N = (R/a)^2$, the mean of the total polarization is

$$2D : \langle \vec{P} \rangle = \frac{2\pi^2}{3} a^4 g N \hat{z} . \quad (3.31)$$

Similarly, in 3D we approximate the sum as an integral of the spherical surface of the cluster. A patch on the surface of area ΩR^2 encompasses $n = \Omega R^2 / (\pi a^2)$ edge cells. The total polarization can therefore be written as an integral over the surface of a spherical cluster:

$$\vec{P}(t) = \frac{R^2}{\pi a^2} \int d\Omega \vec{p}_i(t) . \quad (3.32)$$

The mean polarization will point only in the z direction with magnitude

$$\langle P_z \rangle = \frac{R^2}{\pi a^2} \int d\Omega \langle p_z \rangle = \frac{R^2}{\pi a^2} \int d\Omega \cos \theta \left(\frac{4\pi}{3} a^3 (c_0 + gR \cos \theta) \right) = \frac{16\pi}{9} a g R^3 .$$

For a spherical cluster, $N = (R/a)^3$ and the mean of the total cluster polarization is

$$3D : \langle \vec{P} \rangle = \frac{16\pi}{9} a^4 g N \hat{z} . \quad (3.33)$$

3.6.3 Variance in Cell & Cluster Polarization

Here we derive the variance in cell and collective polarizations. The first section gives a general outline for how this is done for either collective migration mechanism. The following sections will derive the specific expressions for IC, and EC and provide scaling arguments for 1D, 2D and 3D geometries.

General Outline

Since the total collective polarization is a sum of the cell polarization for IC or EC, the variance in the total polarization takes the general form:

$$\begin{aligned} \text{Var}[P_\alpha] &= \underbrace{\sum_{i=1}^N \text{Var}[p_{i,\alpha}]}_{\text{variance contribution}} + \underbrace{\sum_{i \neq j} \text{Cov}[p_{i,\alpha}, p_{j,\alpha}]}_{\text{covariance contribution}} \\ &\equiv V + C, \end{aligned} \quad (3.34)$$

with $\alpha \in \{x, y, z\}$. In order to derive an expression for the variance in collective polarization we must first understand the fluctuations occurring in single cell measurements. The fluctuations in the i^{th} cell's polarization vector are calculated by linearizing each component, $p_{i,\alpha}(t) = \bar{p}_{i,\alpha} + \delta p_{i,\alpha}(t)$ and taking the Fourier transform. The Fourier transform of $\delta p_{i,\alpha}(t)$ takes the general form

$$\delta \tilde{p}_{i,\alpha}(\omega) = \int d^3x_i \int \frac{d^3k}{(2\pi)^3} f(\theta_i, \phi_i) \delta \tilde{c}(\vec{k}, \omega) e^{-i\vec{k} \cdot (\vec{x}_i + \vec{x})} \quad (3.35)$$

where the functional form of $f(\theta_i, \phi_i)$ is dictated by the migration mechanism (EC or IC) and the component α . The cross-spectrum between the i^{th} and j^{th} cells is $\langle \delta \tilde{p}_{i,\alpha}^*(\omega') \delta \tilde{p}_{j,\alpha}(\omega) \rangle$. Utilizing the cross-spectrum we can derive an expression for the variance and covariance in the long-time averaged cell polarization by calculating the power spectrum

$$S_{ij,\alpha}(\omega = 0) = \lim_{\omega \rightarrow 0} \int \frac{d\omega'}{2\pi} \langle \delta \tilde{p}_{i,\alpha}^*(\omega') \delta \tilde{p}_{j,\alpha}(\omega) \rangle. \quad (3.36)$$

The cell polarization variance and covariance is given by:

$$\text{Var}[p_{i,\alpha}] = \frac{1}{T} S_{ii,\alpha}(0), \quad (3.37)$$

$$\text{Cov}[p_{i,\alpha}, p_{j,\alpha}] = \frac{1}{T} S_{ij,\alpha}(0), \quad (3.38)$$

where T is the averaging time. With the above expressions for the cell polarization variance and covariance we can solve for Eq. 3.34 and in turn calculate the relative error for the whole collective. In subsequent sections we show the derivation only for

the z component of the polarization since it is parallel to the gradient. The expressions x and y components will be equal to the z component since the fluctuations in concentration are symmetric in each direction.

3.6.4 Individual-based Chemotaxis

For IC the variance in P_z is

$$\text{Var}[P_z] = \sum_{i=1}^N \text{Var}[p_{i,z}] + \sum_{i \neq j} \text{Cov}[p_{i,z}, p_{j,z}] \equiv V_{\text{IC}} + C_{\text{IC}} . \quad (3.39)$$

The Fourier-transformed fluctuations in IC cell polarization is

$$\delta \tilde{p}_{j,z}(\vec{k}, \omega) = \int_V d^3x \int \frac{d^3k}{(2\pi)^3} \cos \theta \delta \tilde{c}(\vec{k}, \omega) e^{-i\vec{k} \cdot (\vec{x}_j + \vec{x})} . \quad (3.40)$$

The cross-spectrum for the z -component between two cells is

$$\langle \delta \tilde{p}_{i,z}^*(\omega') \delta \tilde{p}_{j,z}(\omega) \rangle = \int_V d^3x d^3x' \int \frac{d^3k d^3k'}{(2\pi)^6} \cos \theta \cos \theta' \langle \delta \tilde{c}^*(\vec{k}', \omega') \delta \tilde{c}(\vec{k}, \omega) \rangle e^{-i\vec{k} \cdot (\vec{x}_j + \vec{x})} e^{i\vec{k}' \cdot (\vec{x}_i + \vec{x}')} . \quad (3.41)$$

We can rewrite Eq. 3.41 by noting that only the relative locations of cell i and j are relevant for the cross-spectrum. Let $\vec{r}_{ij} = \vec{x}_i - \vec{x}_j$ and $r_{ij} = |\vec{r}_{ij}|$.

$$\begin{aligned} \langle \delta \tilde{p}_{i,z}^*(\omega') \delta \tilde{p}_{j,z}(\omega) \rangle &= \int_V d^3x d^3x' \int \frac{d^3k d^3k'}{(2\pi)^6} \cos \theta \cos \theta' \\ &\quad \langle \delta \tilde{c}^*(\vec{k}', \omega') \delta \tilde{c}(\vec{k}, \omega) \rangle e^{-i\vec{k} \cdot \vec{x}} e^{i\vec{k}' \cdot (\vec{r}_{ij} + \vec{x}')} \end{aligned} \quad (3.42)$$

Plugging in Eq. 3.16 for $\langle \delta \tilde{c}^*(\vec{k}', \omega') \delta \tilde{c}(\vec{k}, \omega) \rangle$ and writing $\cos \theta$ in terms of spherical harmonic $Y_1^0(\hat{x})$ yields

$$\begin{aligned} \langle \delta \tilde{p}_{i,z}^*(\omega') \delta \tilde{p}_{j,z}(\omega) \rangle &= \int_V d^3x d^3x' \int \frac{d^3k d^3k'}{(2\pi)^6} \frac{4\pi}{3} Y_1^0(\hat{x}) Y_1^0(\hat{x}') 2D \\ &\quad \frac{2\pi \delta(\omega - \omega')}{(Dk^2 - i\omega)(Dk'^2 + i\omega')} \int d^3y \vec{k} \cdot \vec{k}' \bar{c}(\vec{y}) e^{i\vec{y} \cdot (\vec{k} - \vec{k}')} e^{-i\vec{k} \cdot \vec{x}} e^{i\vec{k}' \cdot (\vec{r}_{ij} + \vec{x}')} \\ &= \frac{4D}{3(2\pi)^5} 2\pi \delta(\omega - \omega') \int_V d^3x d^3x' \int d^3k d^3k' d^3y Y_1^0(\hat{x}) Y_1^0(\hat{x}') \\ &\quad \frac{\bar{c}(\vec{y}) \vec{k} \cdot \vec{k}' e^{i\vec{y} \cdot (\vec{k} - \vec{k}')}}{(Dk^2 - i\omega)(Dk'^2 + i\omega')} e^{-i\vec{k} \cdot \vec{x}} e^{i\vec{k}' \cdot (\vec{r}_{ij} + \vec{x}')} \end{aligned}$$

Plugging in the above expression for $\langle \delta \tilde{p}_{i,z}^*(\omega') \delta \tilde{p}_{j,z}(\omega) \rangle$ into $S_{ij,z}(0)$ (Eq. 3.36) and using the specified mean concentration from Eq. 3.14:

$$S_{ij,z}(0) = \frac{4}{3(2\pi)^5 D} \int_V d^3x d^3x' \int d^3k d^3k' d^3y Y_1^0(\hat{x}) Y_1^0(\hat{x}') \frac{\vec{k} \cdot \vec{k}'}{k^2 k'^2} (c_0 + \vec{g} \cdot \vec{y}) e^{i\vec{y}(\vec{k}-\vec{k}')} e^{-i\vec{k} \cdot \vec{x}} e^{i\vec{k}' \cdot (\vec{r}_{ij} + \vec{x}')} . \quad (3.43)$$

We can break up the expression for $S_{ij,z}(0)$ into two terms: one dependent on the background concentration, the other on the gradient.

$$S_{ij,z}(0) = \frac{4}{3(2\pi)^5 D} \int_V d^3x d^3x' \int d^3k d^3k' Y_1^0(\hat{x}) Y_1^0(\hat{x}') \frac{\vec{k} \cdot \vec{k}'}{k^2 k'^2} e^{-i\vec{k} \cdot \vec{x}} e^{i\vec{k}' \cdot (\vec{r}_{ij} + \vec{x}')} \left((2\pi)^3 \delta^3(\vec{k} - \vec{k}') c_0 + \int d^3y \vec{g} \cdot \vec{y} e^{i\vec{y}(\vec{k}-\vec{k}')} \right) \quad (3.44)$$

Let S_{ij}^1 represent the background concentration term and S_{ij}^2 represent the gradient dependent term in the power spectrum such that $S_{ij,z}(0) = S_{ij}^1 + S_{ij}^2$.

$$S_{ij}^1 = \frac{4c_0}{3(2\pi)^2 D} \int_V d^3x d^3x' \int d^3k Y_1^0(\hat{x}) Y_1^0(\hat{x}') \frac{1}{k^2} e^{-i\vec{k} \cdot \vec{x}} e^{i\vec{k}' \cdot (\vec{r}_{ij} + \vec{x}')} \quad (3.45)$$

$$S_{ij}^2 = \frac{4c_0}{3(2\pi)^5 D} \int_V d^3x d^3x' \int d^3k d^3k' d^3y Y_1^0(\hat{x}) Y_1^0(\hat{x}') \frac{\vec{k} \cdot \vec{k}'}{k^2 k'^2} \vec{g} \cdot \vec{y} e^{i\vec{y}(\vec{k}-\vec{k}')} e^{-i\vec{k} \cdot \vec{x}} e^{i\vec{k}' \cdot (\vec{r}_{ij} + \vec{x}')} \quad (3.46)$$

The following expansions will prove useful:

$$e^{-i\vec{k} \cdot \vec{r}} = 4\pi \sum_{l,m} (-i)^l j_l(kr) Y_l^m(\hat{k}) Y_l^{m*}(\hat{r}) , \quad (3.47)$$

$$\vec{a} \cdot \vec{b} = \frac{4\pi}{3} ab \sum_{m=-1}^1 Y_1^m(\hat{a}) Y_1^{m*}(\hat{b}) . \quad (3.48)$$

Starting with Eq. 3.45 we expand all the exponential terms, and we use these expansions in order to evaluate the angular integrals in S_{ij}^1 .

$$S_{ij}^1 = \frac{2^5(2\pi)c_0}{3D} \int_V d^3x d^3x' \int d^3k Y_1^{0*}(\hat{x}) Y_1^{0*}(\hat{x}') \frac{1}{k^2} \left(\sum_{l_1, m_1} i^{-l_1} j_{l_1}(xk) Y_{l_1}^{m_1}(\hat{x}) Y_{l_1}^{m_1*}(\hat{k}) \right) \left(\sum_{l_2, m_2} i^{l_2} j_{l_2}(r_{ij}k) Y_{l_2}^{m_2}(\hat{k}) Y_{l_2}^{m_2*}(\hat{r}_{ij}) \right) \left(\sum_{l_3, m_3} i^{l_3} j_{l_3}(x'k) Y_{l_3}^{m_3}(\hat{k}) Y_{l_3}^{m_3*}(\hat{x}') \right) \quad (3.49)$$

The angular integrals over \hat{x} and \hat{x}' eliminate the summations over l_1, m_1 and l_3, m_3 .

$$S_{ij}^1 = \frac{2^5(2\pi)c_0}{3D} \int_0^a dx dx' \int d^3k \frac{1}{k^2} x^2 x'^2 j_1(xk) j_1(x'k) Y_1^{0*}(\hat{k}) Y_1^0(\hat{k}) \left(\sum_{l_2, m_2} i^{l_2} j_{l_2}(r_{ij}k') Y_{l_2}^{m_2}(\hat{k}') Y_{l_2}^{m_2*}(\hat{r}_{ij}) \right) \quad (3.50)$$

The product of the two spherical harmonics is

$$Y_1^{0*}(\hat{k}) Y_1^0(\hat{k}) = \frac{1}{\sqrt{4\pi}} \left(Y_0^0(\hat{k}) + \frac{2\sqrt{5}}{5} Y_2^0(\hat{k}) \right).$$

Therefore when evaluating the \hat{k} integral in Eq. 3.50 only the $l_2 = 0, m_2 = 0$ and $l_2 = 2, m_2 = 0$ terms of the summation will be non-zero.

$$S_{ij}^1 = \frac{2^5(2\pi)c_0}{3D\sqrt{4\pi}} \int_0^a dx dx' \int_0^\infty dk x^2 x'^2 j_1(xk) j_1(x'k) \left(j_0(r_{ij}k) Y_0^0(\hat{r}_{ij}) - \frac{2\sqrt{5}}{5} j_2(r_{ij}k) Y_2^0(\hat{r}_{ij}) \right) \quad (3.51)$$

The integrals over x and x' evaluate to:

$$\int_0^a dx x^2 j_1(kx) = \frac{1}{k^3} (2 - 2 \cos(ak) - ak \sin(ak)) \equiv \frac{1}{k^3} h(ak).$$

Note that $Y_0^0(\Theta_{ij}, \Phi_{ij}) = \frac{1}{\sqrt{4\pi}}$, and $Y_2^0(\Theta_{ij}, \Phi_{ij}) = \frac{1}{2} \sqrt{\frac{5}{4\pi}} (3 \cos^2 \Theta_{ij} - 1)$. The angle Θ_{ij} is the angle \hat{r}_{ij} makes relative to the gradient direction \hat{g} , $\cos \Theta_{ij} = \hat{r}_{ij} \cdot \hat{g}$. The expression for S_{ij}^1 reduces to

$$S_{ij}^1 = \frac{2^4 c_0}{3D} \int_0^\infty dk \frac{h^2(ak)}{k^6} [j_0(r_{ij}k) - j_2(r_{ij}k)(3 \cos^2 \Theta_{ij} - 1)] \quad (3.52)$$

We can make the integral dimensionless by making the variable substitutions $u \equiv ak$ and $n_{ij} \equiv r_{ij}/a$.

$$S_{ij}^1 = \frac{2^4 c_0 a^5}{3D} \int_0^\infty du \frac{h^2(u)}{u^6} [j_0(n_{ij}u) - j_2(n_{ij}u)(3 \cos^2 \Theta_{ij} - 1)] \quad (3.53)$$

We can break up Eq. 3.53 into two integrals and evaluate them individually. Note that the exact solution to either integral depends parametrically on n_{ij} and that n_{ij} is the number of cells radii separating two cells. If we are evaluating the cross-correlations

in one cell then $i = j$ and $n_{ii} = 0$; on the other hand, if $i \neq j$ then $n_{ij} \geq 2$ in order to eliminate the possibility of overlapping cells. In either case the expression simplifies to:

$$S_{ij}^1 = \begin{cases} \frac{4\pi c_0 a^5}{45D} & i = j \\ -\frac{\pi c_0 a^5}{18D} \frac{1}{n_{ij}^3} (3 \cos^2 \Theta_{ij} - 1) & i \neq j, n_{ij} \geq 2 \end{cases}. \quad (3.54)$$

Doing the same set of expansions for S_{ij}^2 in Eq. 3.46, and performing the same kind of analysis reveals that the gradient dependent term is asymmetric under exchange of i and j . Therefore when calculating the cluster polarization variance all the S_{ij}^2 terms will cancel. The variance contributions V and C are

$$V_{IC} = \sum_{i=1}^N \frac{1}{T} S_{ii,z}(0) = \frac{4\pi a^5 c_0}{45DT} N, \quad (3.55)$$

$$C_{IC} = \sum_{i \neq j}^N \frac{1}{T} S_{ij,z}(0) = -\frac{\pi a^5 c_0}{18DT} \sum_{i \neq j}^N \frac{(3 \cos^2 \Theta_{ij} - 1)}{n_{ij}^3}, \quad (3.56)$$

resulting in the IC collective total variance

$$\text{Var}[P_z] = \frac{\pi a^5 c_0}{9DT} \left[\frac{4}{5} N - \frac{1}{2} \sum_{i \neq j}^N \frac{(3 \cos^2 \Theta_{ij} - 1)}{n_{ij}^3} \right], \quad (3.57)$$

as in Eqs. 6 and 7 in the main text. Next we will show how Eq. 3.57 scales for collectives in one, two and three dimensional configurations.

One Dimensional Chain

For a one-dimensional chain of IC cells each cell is aligned parallel to the gradient and the angular dependence of C_{IC} (Eq. 3.56) vanishes,

$$C_{IC} = -\frac{\pi a^5 c_0}{18DT} \sum_{i \neq j}^N \frac{2}{n_{ij}^3}. \quad (3.58)$$

We evaluate the sum:

$$\sum_{i \neq j}^N \frac{1}{n_{ij}^3} = 2 \sum_{i < j}^N \frac{1}{n_{ij}^3} = 2 \sum_{i=1}^{N-1} \frac{N-i}{(2i)^3} = \frac{1}{4} (N H_{N-1}^{(3)} - H_{N-1}^{(2)}),$$

with $H_n^{(m)} = \sum_{k=1}^n \frac{1}{k^m}$ the generalized harmonic number. This results in a total variance of the form

$$\text{Var}[P_z] = \frac{\pi a^5 c_c}{9DT} \left[\frac{4}{5}N - \frac{1}{8} \left(NH_{N-1}^{(3)} - H_{N-1}^{(2)} \right) \right]. \quad (3.59)$$

For large N , $H_{N-1}^{(i)}$ approaches a constant for $i \geq 2$. Therefore, we see that $\text{Var}[P_z]$ scales with N for 1D IC collectives as in Table I of the main text.

Two Dimensional Sheet

For a two-dimensional sheet of IC cells, pairs of cells can now make a variety of angles with the gradient, and the angular dependence of C_{IC} cannot be easily simplified. In order to find the N scaling for C_{IC} we calculate the sum numerically. Since the covariances rapidly fall-off as $1/n_{ij}^3$, we only track nearest neighbor pairs that are less than 3 cell radii apart. The resulting numerical solution to the sum in C_{IC} is

$$\sum_{i \neq j}^N \frac{3 \cos^2 \Theta_{ij} - 1}{n_{ij}^3} = 2 \sum_{i < j}^N \frac{3 \cos^2 \Theta_{ij} - 1}{n_{ij}^3} = \frac{1}{4}(1.70N - 2.67\sqrt{N} + 0.89).$$

Therefore the expression for C_{IC} (Eq. 3.56) simplifies to

$$C_{\text{IC}} = -\frac{\pi a^5 c_0}{18DT} (0.43N - 0.67\sqrt{N} + 0.22). \quad (3.60)$$

The covariance contribution, C_{IC} , to leading order scales linearly with N . The total variance becomes

$$\text{Var}[P_z] = \frac{\pi a^5 c_c}{9DT} (0.59N + 0.33\sqrt{N} - 0.11). \quad (3.61)$$

We see that for large N , $\text{Var}[P_z]$ scales with N for 2D IC collectives as in Table I in the main text.

Three Dimensional Cluster

To obtain a scaling for C_{IC} in a three dimensional cluster we assume that cluster is large, such that $a \ll R$ and $N \gg 1$. For a given cell we can calculate its contribution

to C_{IC} by considering the covariance contribution it makes with a set of cells a fixed distance away from it. The equidistant cells form a spherical shell with the principal cell in the center. Adapting Eq. 3.56 for a cell and its spherical shell of covariance pairs yields:

$$C_{\text{cell}} = -\frac{\pi a^5 c_0}{18DT} \frac{1}{n_{\text{shell}}^3} \sum_{i_{\text{shell}}} 3 \cos^2 \Theta_i - 1, \quad (3.62)$$

with n_{shell} the radius of the shell in terms of cell radii. Going to continuum we can calculate the contribution from the cell and all its pairs

$$C_{\text{cell}} = -\frac{\pi a^5 c_0}{18DT n_{\text{shell}}^3} \int_0^{2\pi} d\phi \int_0^\pi d\theta \sin \theta (3 \cos^2 \theta - 1) = -\frac{\pi^2 a^5 c_0}{9DT n_{\text{shell}}^3} \int_0^\pi d\theta (3 \cos^2 \sin \theta - \sin \theta) = 0. \quad (3.63)$$

In the last step, we see that the integral vanishes. Thus, the contribution from a single cell and its shell of pairs sum to zero. Repeating this argument for all cells in the cluster results in the total $C_{\text{IC}} = 0$. Therefore for 3D clusters there is no covariance contribution to the total variance, and $\text{Var}[P_z] = V_{\text{IC}} \sim N$ as in Table I of the main text.

3.6.5 Emergent Chemotaxis Clusters

For EC the variance in P_z is

$$\text{Var}[P_z] = \sum_{i=1}^N \text{Var}[p_{i,z}] + \sum_{i \neq j} \text{Cov}[p_{i,z}, p_{j,z}] \equiv V_{\text{EC}} + C_{\text{EC}}. \quad (3.64)$$

The Fourier-transformed fluctuations in IC cell polarization is

$$\delta \tilde{p}_{i,z}(\vec{k}, \omega) = \cos \Theta_i \int_V d^3x \int \frac{d^3k}{(2\pi)^3} \delta \tilde{c}(\vec{k}, \omega) e^{-i\vec{k} \cdot (\vec{x}_i + \vec{x})}, \quad (3.65)$$

with Θ_i the angle cell i makes with the gradient. The cross-spectrum for the z -component between two cells is

$$\langle \delta \tilde{p}_i^*(\vec{k}', \omega') \delta \tilde{p}_j(\vec{k}, \omega) \rangle = \cos \Theta_i \cos \Theta_j \int_V d^3x d^3x' \int \frac{d^3k d^3k'}{(2\pi)^6} \langle \delta \tilde{c}^*(\vec{k}', \omega') \delta \tilde{c}(\vec{k}, \omega) \rangle e^{-i\vec{k}' \cdot (\vec{x}_j + \vec{x})} e^{i\vec{k} \cdot (\vec{x}_i + \vec{x}')} \quad (3.66)$$

Following the same procedure as in the case of IC, we get an expression for S_{ij}^1 for EC:

$$S_{ij}^1 = \begin{cases} \frac{16\pi c_0 a^5}{15D} \cos^2 \Theta_i & i = j \\ \frac{8\pi c_0 a^5}{9D} \frac{1}{n_{ij}} \cos \Theta_i \cos \Theta_j & i \neq j, n_{ij} \geq 2 \end{cases}. \quad (3.67)$$

Since again $S_{ij}^2 = 0$ by symmetry, the variance for any configuration of EC cells is

$$V_{\text{EC}} = \frac{16\pi a^5 c_0}{15DT} \sum_{i=1}^{N_{\text{edge}}} \cos^2 \Theta_i, \quad (3.68)$$

$$C_{\text{EC}} = \frac{8\pi a^5 c_0}{9DT} \sum_{i \neq j} \frac{\cos \Theta_i \cos \Theta_j}{n_{ij}}, \quad (3.69)$$

as in Eqs. 10 and 11 in the main text. The resulting total variance is

$$\text{Var}[P_z] = \frac{8\pi a^5 c_0}{3DT} \left[\frac{2}{5} \sum_{i=1}^{N_{\text{edge}}} \cos^2 \Theta_i + \frac{1}{3} \sum_{i \neq j} \frac{\cos \Theta_i \cos \Theta_j}{n_{ij}} \right]. \quad (3.70)$$

One Dimensional Chain

For a one-dimensional chain of cells only the two cells on the opposing ends are polarized. The cell variance contribution to the total variance therefore does not change with increasing cluster size,

$$V_{\text{EC}} = \frac{16\pi a^5 c_0}{15DT} \sum_{i=1}^{N_{\text{edge}}} \cos^2 \Theta_i = \frac{32\pi a^5 c_0}{15DT}. \quad (3.71)$$

Therefore $V_{\text{EC}} \sim N^0$ for 1D collectives. For C_{EC} the distance between the two edge cells increases by two cell radii for each cell added to the chain:

$$C_{\text{EC}} = \frac{8\pi a^5 c_0}{9DT} \sum_{i \neq j} \frac{\cos \Theta_i \cos \Theta_j}{n_{ij}} = -\frac{8\pi a^5 c_0}{9DT} \frac{1}{2(N-1)}. \quad (3.72)$$

So $C_{\text{EC}} \sim N^{-1}$ for 1D collectives. To leading order in N the total collective variance depends only on V_{EC} :

$$\text{Var}[P_z] = \frac{32\pi a^5 c_0}{15DT}, \quad (3.73)$$

and so $\text{Var}[P_z]$ does not depend on collective size for 1D EC as in Table I of the main text.

Two Dimensional Sheet

In order to evaluate the variance for a two-dimensional disc of cells we will approximate the sums as integrals over the circumference of the disc as we did in evaluating the mean polarization. Assuming that $a \ll R$ Eq. 3.68 can be written as an integral

$$V_{\text{EC}} = \frac{16\pi a^5 c_0}{15DT} \frac{R}{2a} \int_0^{2\pi} d\theta \cos^2 \theta . \quad (3.74)$$

Using the relation $N = (R/a)^2$ yields

$$V_{\text{EC}} = \frac{8\pi^2 a^5 c_0}{15DT} \sqrt{N} . \quad (3.75)$$

Hence for 2D EC, the variance contribution V_{EC} scales as \sqrt{N} . In order to determine how C_{EC} scales with N we approximate the sums over i and j as a double integral, again assuming that $a \ll R$.

$$C_{\text{EC}} = \frac{16\pi a^5 c_0}{9DT} \left(\frac{R}{2a^2} \right) \int_{\Delta/2}^{2\pi-\Delta/2} d\theta_1 \int_{\theta_1+\Delta/2}^{2\pi} d\theta_2 \frac{\cos \theta_1 \cos \theta_2}{n(\theta_1, \theta_2)} \quad (3.76)$$

Here $\Delta = 2a/R$ is the angular separation between two edge cells, and

$$n(\theta_1, \theta_2) = \frac{2R}{a} \sin \left(\frac{1}{2}(\theta_2 - \theta_1) \right)$$

is the number of cell radii separating two edge cells. Using this expression for $n(\theta_1, \theta_2)$

we evaluate the integral over θ_2 :

$$\begin{aligned} & \left(\frac{R}{2a^2} \right) \int_{\Delta/2}^{2\pi-\Delta/2} d\theta_1 \int_{\theta_1+\Delta/2}^{2\pi} d\theta_2 \frac{\cos \theta_1 \cos \theta_2}{n(\theta_1, \theta_2)} \\ &= \frac{R}{8a} \int_{\Delta/2}^{2\pi-\Delta/2} d\theta_1 \cos \theta_1 [-4(\cos(\theta_1/2) + \cos(\theta_1 + \Delta/2)) - 2 \cos \theta_1 \log(\tan(\Delta/4) \tan(\theta_1/4))] \end{aligned} \quad (3.77)$$

Breaking up the integral into four separate terms we find:

$$\begin{aligned} & \int_{\Delta/2}^{2\pi-\Delta/2} d\theta_1 \cos \theta_1 \cos(\theta_1/2) = 0 , \\ & \int_{\Delta/2}^{2\pi-\Delta/2} d\theta_1 \cos \theta_1 \cos(\theta_1 + \Delta/2) = -\frac{1}{2} \cos(\Delta/2)(\Delta + \sin \Delta - 2\pi) , \\ & \int_{\Delta/2}^{2\pi-\Delta/2} d\theta_1 \cos \theta_1 \log(\tan(\Delta/4)) = -\frac{1}{2}(\Delta + \sin \Delta - 2\pi) \tan(\Delta/4) , \\ & \int_{\Delta/2}^{2\pi-\Delta/2} d\theta_1 \cos \theta_1 \log(\tan(\theta_1/4)) = 0 . \end{aligned}$$

The first and last integrals are equal to zero since the integrands are odd functions over the range $[0, 2\pi]$. With these results, the whole expression simplifies to

$$C_{\text{EC}} = \frac{16\pi a^5 c_0}{9DT} \frac{1}{4} \sqrt{N} \left(\frac{1}{2} \log N + \log 2 - 2 \right) \left(\pi - \frac{2}{\sqrt{N}} \right) \quad (3.78)$$

Keeping only the leading order terms in N yields

$$C_{\text{EC}} = \frac{2\pi a^5 c_0}{9DT} \sqrt{N} \log N . \quad (3.79)$$

The resulting total variance is

$$\text{Var}[P_z] = \frac{8\pi a^5 c_0}{3DT} \sqrt{N} \left[\frac{\pi}{5} + \frac{1}{12} \log N \right] , \quad (3.80)$$

which to leading order scales as $\sqrt{N} \log N$ as in Table I of the main text.

Three Dimensional Cluster

For the three-dimensional cluster, numerical methods must be used in order to find the scaling properties of the variance. We numerically evaluate the total variance (Eq. 3.70) on a cubic lattice and obtain the following results.

The numerical results [Fig. 3.4] show that $V \sim N^{2/3}$ since the number of edge cells also scales as $N^{2/3}$. We also find that $C \sim N$; the covariance contribution to the total cluster polarization grows linearly with N . For large clusters the N scaling dominates the behavior of $\text{Var}[P_z]$. Therefore, in 3D the leading order scaling for the variance is $\text{Var}[P_z] \sim N$ as in Table I of the main text.

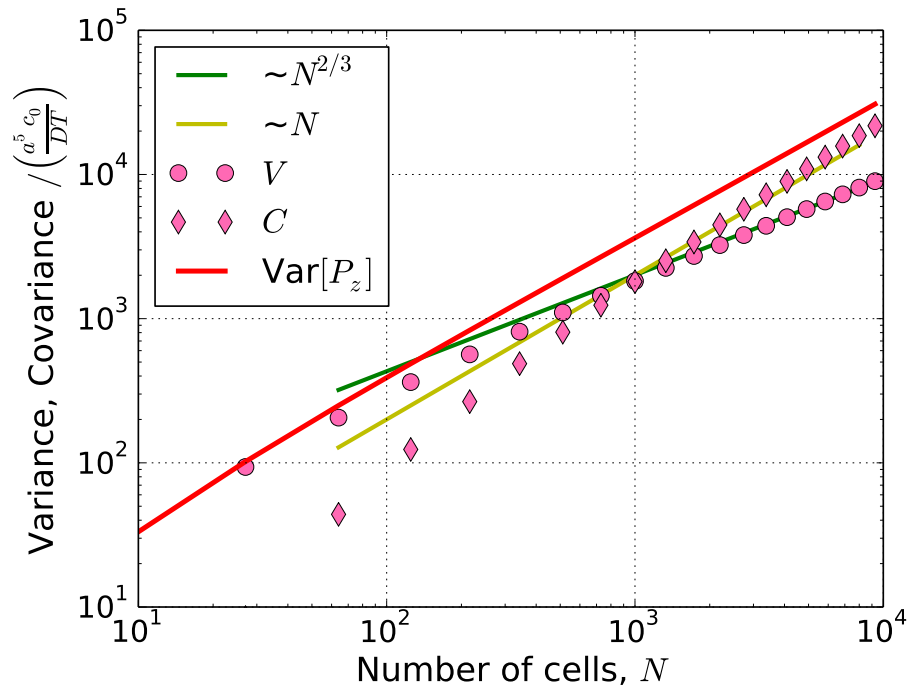


Fig. 3.4. $\text{Var}[P_z]$ for a 3D cluster of EC cells. Cluster variance shown in red. Pink circles are the single cell variance contributions V , and pink diamonds are the cell-cell covariance contributions C .

4. DYNAMICS OF COLLECTIVE CHEMOTAXIS

In this chapter we study the dynamics of more detailed model of collective emergent chemotaxis (EC) than that presented in Ch. 3. Here we further explore how intercellular interactions result in emergent chemotaxis of a cell collective. In Ch. 3 it was assumed that collective edge cells polarize, whereas here we provide a simple, biologically motivated, physical model for how cell polarization emerges from interactions within the collective. It was also assumed that cells in the collective rigidly adhere to one another, this assumption is now relaxed. We explicitly model cell-cell contacts, intracellular molecule production due to chemoattractant sensing, intercellular communication, as well as stochastic fluctuations in individual cell shape and motility. This provides a more realistic application of the EC model presented in Ch. 3 with the addition of cell-cell communication in order to achieve adaptive gradient sensing across a whole collective of cells. The work discussed in this chapter has been published in *Biophysical Journal* [76].

In addition to providing a natural extension to the EC model introduced in Ch. 3, this study also addresses the open question of how gradient sensing is connected to collective cell motion [84–86]. While mechanical models have successfully explained observed collective behaviors such as cell streaming, cell sorting, cell sheet migration, wound healing, and cell aggregation [37–40], these models fall short in explicitly including the effects of multicellular sensing in driving the mechanics at play. Cells are often capable of intercellular communication, so understanding how communicated information is translated into collective migration is of prime interest.

Recent studies by Camley et al. [43] and Malet-Engra et al. [79] have started to address this need for modeling collective sensing and migration. In the study of Camley et al. individual cell measurements act to polarize cells in a cluster outwards causing tension (similar to the EC model in Ch. 3), and when intercellular communi-

cation is incorporated in the model the tension on the cluster adapts to the chemical concentration. However, neither study takes into account the inherent stochasticity of cell sensing and intercellular communication. Individual cell measurements of the environment are error-prone, and propagation of single cell measurements via intercellular communication also adds noise to the system. Accounting for these effects is crucial since collectives have been shown to operate near the limits of what is physically possible. Additionally, these studies also treat cells or clusters as perfect circles, neglecting natural geometric fluctuations in the size and shapes of cells that naturally occurs during collective migration.

Here we focus our attention on stochastic processes governing collective gradient sensing and cell motility. First, we describe the multicellular implementation of the local excitation-global inhibition (LEGI) biochemical network [35] used for collective gradient sensing. Information gained from collective sensing is then used to direct cell motion. We develop a model which takes into account the fluctuating shape of cells while coupling cell motility to noisy collective gradient sensing. We model intercellular communication via the direct exchange of messenger molecules between cells. Candidate mediators of such intercellular communication have been recently identified in *Drosophila* development [87], and other studies suggest intercellular communication's involvement in organoid branching, angiogenesis, and cancer [25, 88–90]. We study cluster migration in shallow gradients where the change in concentration across a cell width is very small relative to the background concentration. This regime is of prime interest since experiments show that collectives can respond to these shallow gradients whereas single cells cannot [25, 32, 79]. By explicitly modeling the stochastic processes of sensing and migration this model places constraints on the collective behavior of cells and predicts an optimal cluster size for fastest chemotaxis. We conclude by discussing our model's implications for cell migration experiments.

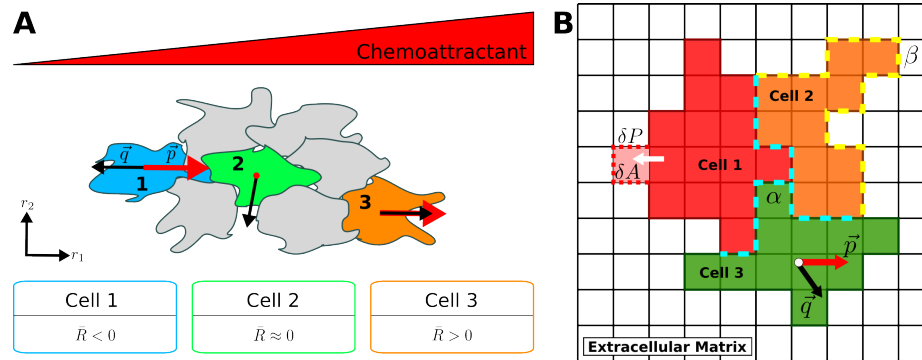


Fig. 4.1. Model implementation. (A) Cell polarization is biased by multicellular sensing. On average, the cells on the left and right edges will measure negative and positive values of R , respectively. This causes the left-edge (Cell 1) and right-edge (Cell 3) cells to polarize in the direction of the gradient, while cells in the middle (Cell 2) are on average not polarized since $\bar{R} \approx 0$. Polarization vectors \vec{p} are red, repulsion vectors \vec{q} are black. (B) Simulations are implemented using the Cellular Potts Model (CPM). Cells comprise of simply connected lattice points. There are adhesion energies associated with different types of contact: cell-cell, α (blue-dashed line), and cell-ECM, β (yellow-dashed line). Cell motility is modeled by the addition/removal of lattice points (pink). Each cell has a center-of-mass (white dot), a polarization vector, \vec{p} (red) and a repulsion vector, \vec{q} (black).

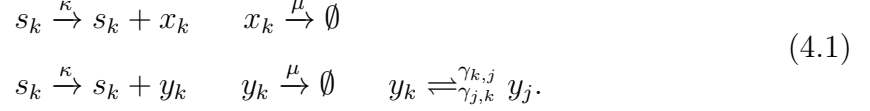
4.1 Model

In order for collective chemotaxis to occur cells within the collective must sense the chemoattractant, polarize in response to their sensory network, and then move in the direction of polarization. First we describe the biochemical network used to detect the chemoattractant and communicate information about it throughout the collective. Next the connection between sensing and cell polarization is explained, and then we describe our simulation implementation of the model used to study its dynamics.

4.1.1 Multicellular LEGI Gradient Sensing

Communication between cells and collective sensing can improve upon an individual cell's ability to sense the environment [25], and in turn this information may be used to direct cell motion. In the LEGI model cells produce two chemical species, a "local" species X , and a "global" species Y , in response to the chemoattractant S . The local species X remains within an individual cell and represents that cell's measurement of its local chemical concentration. This species can be a molecule produced or activated in response to attractant-bound receptors, or the bound receptors themselves. The global species Y can diffuse at the rate γ between neighboring cells and therefore represents the average X population among neighboring cells. Y molecules may only be exchanged when two or more cells are in direct contact with one another. Recent experiments in epithelial cells identified this global species as either calcium or a small molecule involved in calcium signaling (such as IP3), and identified the intercell diffusion mechanism as mediated by gap junctions [25]. Finally, X activates a downstream reporter molecule R , while Y inhibits R . [CONSIDER ADDING FIGURE THAT ILLUSTRATES LEGI (similar to Ch1 fig)]

Let x_k , y_k , and R_k represent the molecule populations in X , Y , and R in the k^{th} cell. The chemical reactions in cell k are



The production and degradation rates for X and Y are κ and μ , respectively. The global reporter molecule exchange rate γ is dependent on the length of the interface \mathcal{C} made between adjacent cells, and on the exchange rate per unit contact-length Γ ,

$$\gamma_{j,k} = \int_{\mathcal{C}} \Gamma dl. \quad (4.2)$$

Therefore the exchange rate γ between pairs of cells is not constant, but will vary with time depending on the interface size between cells.

In the limit of shallow gradients, which are of primary interest in studying collective sensing, R effectively reports the difference in X and Y molecule populations [25] and so we will model the downstream readout as $R_k = x_k - y_k$. A negative (positive) difference indicates that the cell is below (above) the average measured concentration relative to nearby cells as shown by the reported average R values for each cell in Fig. 4.1A.

The chemical concentration is modeled as a space-dependent field $E(r_1, r_2)$, and in this case has a constant gradient in the r_1 -direction,

$$E(r_1, r_2) = \bar{c}gr_1.$$

The average signal in the k^{th} cell's local environment is $\bar{s}_k = \int_{A_k} dr_1 dr_2 E(r_1, r_2)$ where A_k is the area of the k^{th} cell. Since diffusion is a Poisson process the variance in the measured signal s_k is equal to the mean, $\sigma_{s_k}^2 = \bar{s}_k$. At each time step we sample s_k for each cell from a Gaussian distribution with mean and variance \bar{s}_k , which corresponds to instantaneous sensory readout [25]. The dynamics of the local reporter satisfy the stochastic differential equation

$$\dot{x}_k = \kappa s_k - \mu x_k + \eta_{x_k}. \quad (4.3)$$

The first term in Eq. 4.3 is due to the production of X molecules due to the signal S , the second term represents molecule degradation, and the third term η_{x_k} accounts for the noise inherent to these reactions. The noise term is equal to $\eta_{x_k} = \sqrt{\kappa \bar{s}_k} \xi_{1,k} - \sqrt{\mu \bar{x}_k} \xi_{2,k}$ since both production and degradation are stochastic processes [91]. In Eq. 4.3 and subsequent stochastic equations $\xi_{i,k}$ and $\chi_{j,k}$ are unit Gaussian random variables representing the noise in molecule populations. For the local reporter, the steady-state solution is simply

$$x_k^{ss} = (\kappa/\mu) s_k + (1/\mu) \eta_{x_k}. \quad (4.4)$$

The dynamics of the global species can be modeled in similar fashion,

$$\dot{y}_k = \kappa s_k - \mu y_k - y_k \sum_{\langle j,k \rangle} \gamma_{j,k} + \sum_{\langle j,k \rangle} y_j \gamma_{j,k} + \eta_{y_k}. \quad (4.5)$$

The first summation term in Eq. 4.5 accounts for the loss of y_k due to the diffusion out to neighboring cells, and similarly the second summation term accounts for the increase in y_k due to diffusion into cell k from its neighbors. The notation $\langle j, k \rangle$ represents the set of all nearest neighbor pairs. The noise term η_{y_k} in the molecule dynamics depends on the production, degradation and diffusion of Y molecules. In steady-state we can express the noise as

$$\eta_{y_k} = \sqrt{\kappa \bar{s}_k} \xi_4 - \sqrt{\mu \bar{y}_k} \xi_5 + \sum_{j=1}^N [\chi_{j,k} \sqrt{\gamma_{j,k}} (\sqrt{\bar{y}_j} - \sqrt{\bar{y}_k})].$$

Similarly to η_{x_k} , the noise in y_k also depends on production and degradation while an extra term is required to account for the noise in Y molecule exchange. Eq. 4.5 can be simplified by noting that exchange rates between cells are symmetric $\gamma_{j,k} = \gamma_{k,j}$, $\gamma_{i,i} = 0$, and by defining the sum of all the exchange rates between cell k and all other cells as $G_k = \sum_{j=1}^N \gamma_{j,k}$. The steady-state solution for the global reporter is more involved than the local reporter, and can be written as a matrix equation

$$M \vec{y}^{ss} = \kappa \vec{s} + \vec{\eta}_y, \quad (4.6)$$

where M is a square, symmetric matrix that governs the degradation and exchange of Y molecules in all cells,

$$M = \begin{bmatrix} \mu + G_1 & -\gamma_{1,2} & \cdots & -\gamma_{1,N} \\ -\gamma_{2,1} & \mu + G_2 & \cdots & -\gamma_{2,N} \\ \vdots & \vdots & \ddots & \vdots \\ -\gamma_{N,1} & -\gamma_{N,2} & \cdots & \mu + G_N \end{bmatrix}. \quad (4.7)$$

The physical limits to LEGI gradient sensing, as mentioned in Ch. 1, are derived from those of individual cell gradient sensing. Recall that the relative error in single cell gradient sensing results from the cell taking the difference in molecule counts measured in two different regions on the cell surface. The relative error in each compartments concentration measurement is $\sigma_c^2/\bar{c}^2 \sim 1/(s\bar{c}DT)$ with s the compartment size, \bar{c} the mean concentration, D the diffusion coefficient, and T the integration time. Taking the difference of the two measurements yields the lower limit to the relative error in the gradient,

$$\frac{\sigma_g}{\bar{g}} \sim \sqrt{\frac{\bar{c}}{s(a\bar{g})^2DT}}. \quad (4.8)$$

For the LEGI model, Eq. 4.8 can be generalized to the case of multicellular gradient sensing in the limit of strong communication ($\gamma \gg \mu$) [33]. In this limit the relative error in LEGI gradient sensing scales as

$$\frac{\sigma_g}{\bar{g}} \sim \sqrt{\frac{\bar{c}}{a(n_0 a \bar{g})^2DT}}, \quad (4.9)$$

with a the cell size and n_0 being the number of cells over which LEGI can reliably transmit information about the chemoattractant. Communication improves when Y molecule diffusion increases and worsens with faster Y molecule degradation, so $n_0 \propto \gamma/\mu$. As collectives grow larger than n_0 cells the relative error ceases to improve, saturating to the limit set by Eq. 4.9. This is unlike the case where the effects of communication are ignored and the relative error decreases with collective size N without bound

$$\frac{\sigma_g}{\bar{g}} \sim \sqrt{\frac{\bar{c}}{a(Na\bar{g})^2DT}}. \quad (4.10)$$

4.1.2 Connecting Gradient Sensing to Cell Motility

To describe collective migration, we integrate the output of multicellular LEGI gradient sensing with cell motility. Cells in motion have a distinct front and are polarized along the direction of the front to back. Cells within the cluster have their polarization biased by a combination of the LEGI readout and intercellular repulsion due to contact inhibition of locomotion (CIL). CIL is the phenomenon where cells that come into contact cease to form protrusions in the direction of contact [44]. This is a very simple way for cells to translate the noisy, error-prone gradient measurements into collective cell motility [11, 43, 79].

In order to connect sensing to motility, we couple individual cell polarization \vec{p} to both the LEGI downstream readout R and what we will call the cell's repulsion vector \vec{q} . The cell's polarization vector represents the desired direction of motion [10] and modeling collective behavior using cell polarization has been done previously [38, 43]. Information about the cell's surroundings are naturally expressed by the repulsion vector \vec{q} [43]. The repulsion vector is representative of contact inhibition of locomotion (CIL) [44]. CIL demonstrates that cells are aware of their immediate surroundings. The repulsion vector for cell k is a unit vector that points away from all of cell k 's neighbors.

$$\vec{q}_k = \left(\frac{1}{\sum_{\langle j,k \rangle} L_{j,k} |\vec{x}_k - \vec{x}_j|} \right) \sum_{\langle j,k \rangle} L_{j,k} (\vec{x}_k - \vec{x}_j), \quad (4.11)$$

where $L_{j,k}$ is the contact length made between cell k and its neighboring cell j . In our model cell polarization will change as a function of time depending on a combination of the repulsion vector and the LEGI downstream readout,

$$\frac{d\vec{p}_k}{dt} = r \left[-\vec{p}_k + \epsilon \frac{R_k}{\sigma_R} \vec{q}_k \right]. \quad (4.12)$$

The first term in Eq. 4.12 models the decay of cell polarization. In the absence of any stimulus an individual cell will undergo a persistent random walk with a timescale $1/r$ [38]. The second term acts to align or anti-align the cells polarization vector with the repulsion vector, with alignment strength ϵ based on the cell's readout R_k .

The magnitude of R_k is normalized by its standard deviation σ_R . The net effect is illustrated in Fig. 4.1A.

In the presence of a gradient, cells on the edge near the lower-end of the chemical concentration will tend to be polarized into the cluster (Cell 1 in Fig. 4.1A), whereas cells on the higher concentration edge tend to be polarized outwards (Cell 3 in Fig. 4.1A). Cells in the center of the cluster (Cell 2 in Fig. 4.1A) are on average unpolarized. The net effect is that the cells on the edges of the cluster will drive motion in the direction of increasing chemical concentration. It is important to note that in this model single cells are unable to chemotax since the multicellular LEGI mechanism requires more than one cell to detect a gradient, and similarly without neighboring cells there is no repulsion vector to bias the cell's polarization.

4.1.3 Computational Implementation

Computational simulations are conducted in order to understand the dynamics that evolve from the model of collective sensing and migration. The source code for the simulations can be found here [92]. The implementation chosen is the Cellular Potts Model (CPM) [46,47] although other cellular automata models are possible as well [93–95]. The CPM is widely used for simulating cell-centric systems. Despite its relative simplicity, this computational implementation can qualitatively reproduce diverse biological phenomena [48]. The CPM is a very good implementation for simulating systems wherein cell geometry is crucial to the dynamics of the system. Using CPM many studies, some involving cell polarization and mechanical-based coupling, successfully reproduce epithelial cell streaming, cell sorting, chemotaxis and collective migration [37,38,45].

In the CPM cells exist on a discrete lattice and are represented as groupings of lattice points. Simply-connected groups of lattice sites x with the same integer values for their *lattice label* $\sigma(x) > 0$ comprise a single cell. The extracellular matrix (ECM) is labeled with the lattice label $\sigma(x) = 0$. Cells have a desired size and perimeter

from which they can fluctuate, and cells adhere to their neighboring environment with an associated adhesion energy. The energy of the whole system is the sum of contributions from adhesion $J_{i,j}$, area-restriction λ_A , and perimeter-restriction λ_P terms,

$$u = \sum_{\langle x, x' \rangle} J_{\sigma(x), \sigma(x')} + \sum_{i=1}^N (\lambda_A (\delta A_i)^2 + \lambda_P (\delta P_i)^2), \quad (4.13)$$

$$J_{\sigma(x), \sigma(x')} = \begin{cases} 0 & \sigma(x) = \sigma(x') \text{ (within the same cell),} \\ \alpha & \sigma(x)\sigma(x') > 0 \text{ (cell-cell contact),} \\ \beta & \sigma(x)\sigma(x') = 0 \text{ (cell-ECM contact).} \end{cases} \quad (4.14)$$

The parameters α and β characterize intercellular adhesiveness, and in order to ensure that it is energetically favorable for cells to remain in contact, we restrict $\beta > 2\alpha$ [38]. β represents the cell-ECM contact energy, a larger value corresponds to an ECM

Parameter	Value	Notes
Concentration \bar{c}	10nM	Assumes $\bar{c} \gg a\bar{g}$ for shallow gradients [25, 79]
Gradient \bar{g}	0.04nM/ μm	
Production Rate κ	19.72min ⁻¹	Assumes $\{\kappa, \mu\} \gg r$, i.e. biochemical signaling is faster than motility response
Degradation Rate μ	19.72min ⁻¹	
Exchange Rate Γ	80($\mu\text{m min}$) ⁻¹	Varied in Fig. 4.3
Polarization Bias Strength ϵ	0.8	Varied in Fig. 4.2
Polarization Decay Rate r	3.94min ⁻¹	Sets polarization memory time, as used in [38]
Relaxed Cell Area A_0	315 μm^2	Assumes cell radius 10 μm [12]
Relaxed Cell Perimeter P_0	3.6 $\sqrt{A_0}\mu\text{m}$	Assumes circular resting shape
Cell-cell Contact Energy α	1.0	Sets energy scale $2\beta > \alpha$ for cell adhesion [46] (Varied in Fig. 4.2)
Cell-ECM Contact Energy β	3.5	
Area Energy Cost λ_A	1.5	Prevents “stringy” cell-shapes
Perimeter Energy Cost λ_P	0.01	

Table 4.1.

Table of parameter values. Energy costs are in units of $k_B T$, where $k_B T$ is the thermal energy of the CPM Monte Carlo scheme.

that is more difficult to traverse. Heterogeneities in the microenvironment could be represented by a spatially dependent β ; here we take β to be a constant. The area- and perimeter-restriction energy terms prevent cells from growing or shrinking to unphysical sizes as well as branching or stretching into unphysical shapes. Cells fluctuate in shape and size around the desired area A_0 and perimeter P_0 with $\delta A_i \equiv A_i - A_0$ (and similarly for δP_i). The resulting dynamics evolve from the minimization of the system's energy under thermal fluctuations.

Cell dynamics are a consequence of minimizing the energy of the whole system. This is a random process that is sensitive to thermal fluctuations and is modeled using a Monte Carlo process. In a system of n lattice sites, one *Monte Carlo* time step (MC step) is composed of n *elementary* steps. Each elementary step consists of an attempt to copy the lattice label of a randomly chosen lattice site onto that of a randomly chosen neighboring site as illustrated by the pink lattice site in Fig. 4.1B. The new configuration resulting from the copy is accepted with probability P , which depends on the change in the system's energy accrued in copying over the lattice label,

$$P = \begin{cases} e^{-(\Delta u - w)} & \Delta u - w > 0, \\ 1 & \Delta u - w \leq 0. \end{cases} \quad (4.15)$$

The term Δu is the change in energy of the system due to the proposed lattice label copy. w is the *bias* term which acts to bias cell motion in the direction of polarization. The bias term in the CPM model is required in order for cell clusters to exhibit directed motion [38],

$$w = \sum_{k=\sigma(a), \sigma(b)} \frac{\Delta \vec{x}_{k(a \rightarrow b)} \cdot \vec{p}_k}{|\Delta \vec{x}_{k(a \rightarrow b)}| |\Delta \vec{x}_{k(\Delta t)}|}. \quad (4.16)$$

The summation in Eq. 4.16 is over the cells involved in the elementary time step: a is the lattice site being copied, and b is the lattice site being changed. The change in the cell's center of mass position during the elementary time step is $\Delta \vec{x}_{k(a \rightarrow b)}$, whereas $\Delta \vec{x}_{k(\Delta t)}$ is the cell's change in the center of mass during a MC step. The cell polarization vector \vec{p}_k is updated at every MC step in accordance with Eq. 4.12. The

dot product acts to bias cell motion since movement that is parallel to the polarization vector will result in a more positive w which in turn results in a higher acceptance probability (Eq. 4.15).

In addition to calculating the energy of the system, at each MC step the X and Y molecule populations in each cell are sampled by solving Eq. 4.4 and 4.6. In doing so our model accounts for fluctuations in molecule numbers, cell shape, and cell-cell contact. With this computational implementation cells on the edges of the cluster are polarized in the direction of increasing chemical concentration, and cells near the center of the cluster have no net polarization, resulting in collective migration in the direction of increasing chemical concentration.

4.2 Results

We simulate clusters of various sizes migrating in response to shallow constant chemical gradients over a fixed distance (Fig. 4.2A, Movie S1). The simulation results were calibrated using the cluster migration data from Malet-Engra et al. [79] and assuming a typical cell radius $a = 10\mu\text{m}$. Similar to the experimental study, initial simulations were conducted with a gradient and background concentration equivalent to $\bar{g} = 0.001\text{nM}/\mu\text{m}$ and $\bar{c} = 1\text{nM}$. We found that increasing the gradient and background concentration values to those reported in Table 4.1 (see pg. 11), which still maintain the limit $a\bar{g} \ll \bar{c}$, decreased computation cost while yielding the same qualitative results. Therefore all results presented here use the values of \bar{c} and \bar{g} in Table 4.1. The simulation timescale was then calibrated such that clusters of cells migrate with velocities on the same order as those in the study by Malet-Engra et al. All simulation parameter values used are presented and motivated in Table 4.1 unless specified otherwise.

In order to quantify model behavior, statistics on the simulated mean first-passage time (MFPT) for migrating clusters are collected. The first-passage time is the time it takes for the center of mass of a cluster of cells to cross a threshold distance. First it

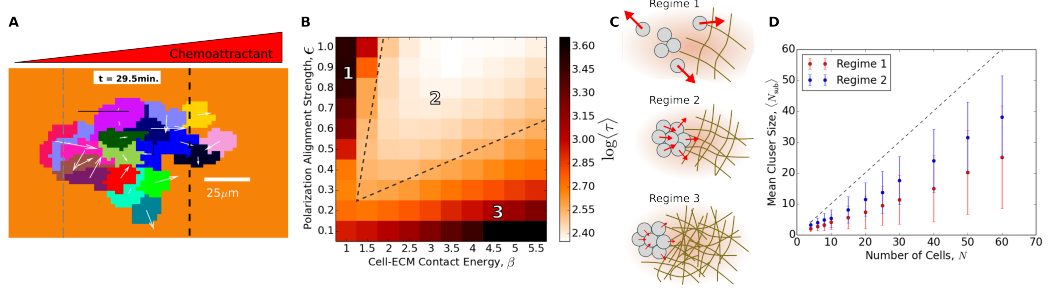


Fig. 4.2. Characterizing the emergent multicellular migration. (A) Snapshot from simulation. Individual cells are distinguished by color and white arrows represent their polarization vectors. The cluster centroid is initially located along the gray dashed line and must cross the black dashed line in order to record a first-passage time event. (B) A heat-map of MFPT in units of minutes as a function of cell-ECM adhesion energy, β and polarization bias strength, ϵ . Warmer colors represent higher MFPT values (colorbar). Parameter values for the heat-map: $N = 20$, $\bar{c} = 10 \text{ nM}$, $g = 0.004 \text{ nM}/\mu\text{m}$, $\Gamma = 80 (\mu\text{m min.})^{-1}$. Illustrations in (C) represent cluster migratory behavior in their respective regimes of parameter space. Larger values of ϵ correspond to larger cell polarization vectors (red arrows), whereas larger values of β correspond to an ECM that is more difficult to traverse. (D) Mean cluster size $\langle N_{\text{sub}} \rangle$ as a function of the total number of cells in the system N . Regime 1: $\beta = 1.5$, $\epsilon = 1.0$. Regime 2: $\beta = 3.5$, $\epsilon = 0.8$

is important to understand the effects of the various parameters in our model on simulations results. Across simulations, two crucial parameters emerge: β the cell-ECM adhesion energy, and ϵ the polarization bias strength. When these two parameters are varied three distinct phases of collective cell migration are clear (regimes 1, 2, and 3 in Fig. 4.2B).

Fig. 4.2B shows that for sufficiently large β the mean first-passage time remains relatively constant as β and ϵ grow in proportion to one another. In this phase, regime 2 of Fig. 4.2B, cells migrate as a collective as illustrated in Fig. 4.2C. However if the adhesion energy is further increased while the bias strength remains fixed the MFPT starts to increase (regime 3 of Fig. 4.2B). This is due to the increased energy cost in cells making protrusions into the ECM. If β is increased further the cluster cells

will eventually stop moving since protrusions become highly improbable as dictated by the CPM (Fig. 4.2C). The other large MFPT phase is due to increasing ϵ while keeping β fixed (regime 1 of Fig. 4.2B). In this case the cell's polarization becomes large enough to overcome the intercell adhesion energy causing the cluster of cells to scatter as illustrated in Fig. 4.2C. To further characterize whether a cluster will scatter or remain persistently connected, we track the mean subcluster size $\langle N_{\text{sub}} \rangle$, defined as the average cluster size weighted by the number of cells present in each constituent cluster (Fig. 4.2D). Although cells' initial configuration is that of a single cluster, partial scattering may occur stochastically and reversibly, leading to a value of $\langle N_{\text{sub}} \rangle$ that is less than the cluster size N . As seen in Fig. 4.2D, the persistence $\langle N_{\text{sub}} \rangle / N$ is largely independent of N , and clusters in the parameter space of regime 2 are more persistent than those corresponding to regime 1 where cells are likely to scatter permanently. Overall, we see that there is a large region in parameter space which yields physically realistic behavior, and the model breaks down in the limits where we would expect it to. With this in mind we further examine simulations within regime 2 of parameter space.

Next we examine the MFPT as a function of cluster size (Fig. 4.3A). Starting from $N = 2$ we see that for sufficiently large Γ (red curve), as the number of cells increases the MFPT decreases. This can be understood from our description of multicellular sensing (Eq. 4.10): before reaching the critical number of cells in a cluster, the error in gradient sensing decreases as $\sigma_R / \bar{R} \sim N^{-1}$ and so the cluster's ability to more precisely measure the gradient increases. The decreased sensing error translates into more accurately directed cell polarization vectors causing the MFPT to decrease. Fig. 4.3B shows the relative error vs. the number of cells in the cluster that are parallel to the gradient direction, N_g . In the small-cluster regime and for fast communication (yellow curve) there is a decrease in relative error with N_g , that is in close agreement with the theoretical prediction for the scaling of N_g^{-1} (Eq. 4.10). Since the global-reporter exchange rate between cells is very large compared to the degradation rate ($\gamma \gg \mu$) it is expected that the effects of communication can be neglected as was

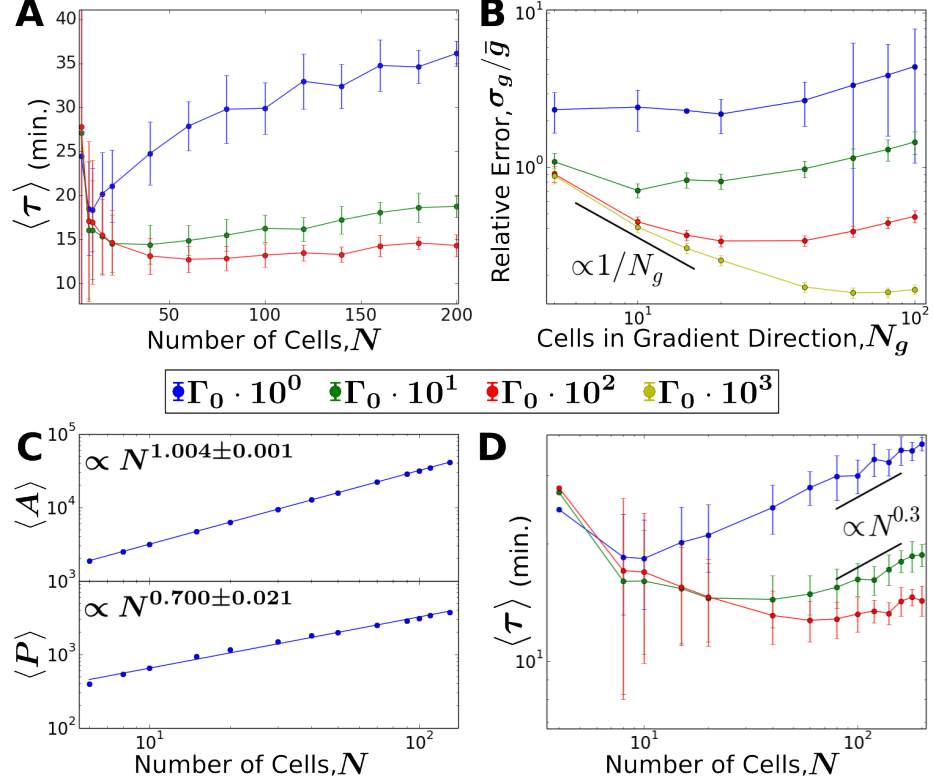


Fig. 4.3. Tradeoff between sensing and drag leads to a minimum mean first-passage time (MFPT) with cluster size. $\Gamma_0 = 0.80(\mu\text{m min})^{-1}$. (A) MFPT for various values of the exchange rate per unit contact-length Γ . (B) Relative error in gradient sensing for various values of Γ . (C) Area A and perimeter P scaling relationships with the number of cells N in a cluster. (D) MFPT results in A on a log-log scale, compared with the geometric prediction arising from C. All error bars represent standard deviation.

the case in deriving Eq. 4.10. However, as the cluster grows in size the effects of communication can no longer be neglected. As illustrated in Fig. 4.3B the relative error reaches a lower limit as predicted by Eq. 4.9 at which sensory precision will no longer increase with increased cluster size.

As the number of cells increases the MFPT tends to saturate to a minimal value and may even begin to increase (Fig. 4.3A). The MFPT reaches a minimum around $N \sim 10-100$ cells depending on the choice of Γ , the global molecule exchange rate per

unit contact-length. Communication between cells improves as Γ increases since more Y molecules can be quickly transmitted between cells, pushing the point of saturation to larger cluster sizes. From these results we see that the model predicts an optimal cluster size for fastest migration. This prediction is in contrast with similar studies which in some cases predict a saturation in velocity and therefore constant MFPT as a function of cluster size [43, 79]. The dependence of MFPT on cluster size is further explored in the Discussion.

In the limit that $\Gamma a/\mu \lesssim 1$ (a being the cell radius) intercellular communication within the cluster is highly localized, and increasing the size of the cluster will not improve sensory precision. If this is the case then the cluster will have outgrown its optimal size for gradient detection. Instead of the cluster acting as one cohesive gradient-sensing device the cluster will comprise several independent gradient sensors which cannot reliably share information with one another. Therefore, in the small Γ limit we expect the MFPT to monotonically increase with increasing N due to increased drag on the cluster. Indeed, simulation results confirm our expectations in the large N , small Γ limit (Fig. 4.3A, blue curve).

Next we asked if the MFPT had any dependence on the geometrical properties of the migrating clusters [96]. The mean first-passage time should scale proportionally with the drag experienced on the cluster, whereas it should be inversely related to the force driving migration,

$$\langle \tau \rangle \sim \frac{\text{drag}}{\text{force}}. \quad (4.17)$$

The drag on the cluster should scale with the area of the cluster, $\text{drag} \propto A(N)$, and the driving force should scale with the perimeter of the cluster since we know that only cells on the edges of the cluster are polarized in the desired direction, $\text{force} \propto P(N)$. Although the size and shape of clusters will fluctuate we can obtain from many simulations how the average area $\langle A \rangle$ and perimeter $\langle P \rangle$ scale with N . Fig. 4.3C shows that both scale with powers of N , i.e. $\langle A \rangle \sim N^d$ and $\langle P \rangle \sim N^f$. We find $d = 1.004 \pm 0.001$, which makes sense since the average area of the should scale linearly with the number of cells. We also find $f = 0.700 \pm 0.021$, which is

intriguing because for a circular cluster we would expect $f = 1/2$. The larger value of f reflects the elongated and amoebic shape of the cluster (Fig. 4.2A), which causes its perimeter-to-area ratio to be larger than that expected for a circle.

Given these geometric scalings, Eq. 4.17 then makes a prediction: the MFPT should scale as $\langle\tau\rangle \sim N^{d-f} = N^{0.304 \pm 0.021}$. We compare this prediction to the MFPT data, on a log-log scale, in Fig. 4.3D. We see that in the large N , small Γ limit, the prediction agrees well with the data (blue and green curves). This demonstrates that the slowdown of large, poorly communicating clusters is dominated by the geometrical aspects of cluster propulsion and drag.

In summary, in the limit that communication between cells is strong ($\Gamma a/\mu \gg 1$), information can be reliably transferred over $n_0 \gg 1$ cells. As long as cluster sizes N remain smaller than n_0 cells, there will be an improvement in the sensory capability of the cluster with size, and an associated decrease in the MFPT $\langle\tau\rangle$. As the critical size n_0 is reached, sensory ability will cease to improve with size, and $\langle\tau\rangle$ will reach a minimum. Further addition of cells will cause $\langle\tau\rangle$ to increase according to $\langle\tau\rangle \sim \text{drag/force}$, since the drag is proportional to the cluster area, whereas the force is proportional only to the cluster perimeter.

4.3 Discussion

We have developed a model in which collective sensing of noisy chemical gradients induces multicellular migration. The model includes the stochastic processes of ligand and diffusion, intercellular communication and cell shape fluctuations. In the model cells are polarized based on collective gradient information and contact-mediated interactions, leading to biased migration despite the fact that individual cells do not chemotax. We find that the antagonistic effects of sensing and drag result in a minimum mean first-passage time (MFPT) as a function of cluster size, i.e. an optimal size for fastest migration. The optimal size is governed by the strength of cell-cell

communication, with stronger communication leading to both a larger optimal size and a decreased migration time (Fig. 4.3D).

Whereas previous models have idealized cell or cluster geometries as perfect circles [43, 96], our use of the cellular Potts model has allowed us to capture natural fluctuations in cell and cluster shape. As a result, we have found that while migrating, clusters adopt a shape that is (i) elongated in the gradient direction and (ii) non-convex (see Fig. 4.2A). Both features lead to a cluster perimeter-to-area ratio that is significantly larger than that expected for a circle or other convex shape with aspect ratio near unity. Importantly, we have found that the area and perimeter scalings remain predictive of MFPT in the communication-limited regime (Fig. 4.3D), even with the observed non-circular and fluctuating geometries.

To the extent possible, our model has been constructed and parameterized using current experiments on collective migration. Intercellular communication is modeled as a direct exchange of messenger molecules between cells since this type of communication has been implicated in development, organoid branching, angiogenesis, and cancer [25, 87–90]. The chemical concentration and gradient values are selected to ensure that our simulations are in the shallow gradient regime, where experiments show that collectives can respond whereas single cells cannot [25, 32, 79]. Cell size, chemical concentration, chemical gradient, cell-cell contact energy, and cell-ECM contact energy values are taken from previous experimental studies of collective cell behavior (Table 4.1).

How do our model predictions compare to experiments? There have been many studies on collective migration [18, 21, 85, 87] though only one (to our knowledge), by Malet-Engra et al. [79], measures migratory properties as a function of cluster size. The experiments conducted by Malet-Engra et al. reveal that beyond a minimum cluster size, the cluster velocity saturates to a maximal value and then remains constant with increasing cluster size. In our study, we find that when communication is strong, the MFPT – which is inversely related to the mean velocity – also saturates to a minimal value and remains constant for a large range of cluster sizes. As

shown in Fig. 4.3A (red curve), as the cluster size increases from about 30 to 200 cells the MFPT remains relatively constant, in qualitative agreement with the aforementioned experimental results. This saturation regime occurs when communication is sufficiently strong to suppress, over a large range of cluster sizes, the drag-induced slowdown. Our findings thus suggest that sensory information is reliably transferred throughout the clusters of lymphocytes studied by Malet-Engra et al., and that communication is strong enough that drag does not strongly constrain migration speed for the cluster sizes analyzed.

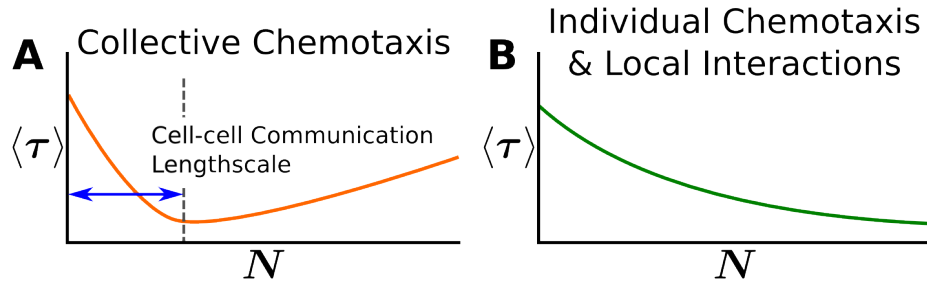


Fig. 4.4. Prediction to distinguish collective from individual chemotaxis in experiments. (A) Expected MFPT behavior for cluster migration driven by collective sensing. (B) Expected MFPT behavior for cluster migration driven by local interactions.

Furthermore, our results suggest a simple experimental test that can distinguish whether cluster chemotaxis is purely collective or individually driven. Broadly speaking, cluster migration (i) can emerge collectively from cells that communicate, either chemically or mechanically, but do not chemotax alone (as in our model), or (ii) it can result from many individual agents that take independent measurements of the environment and through physical coupling or local interactions produce collective migration [42, 97] (a so-called “many wrongs” mechanism [41]). As illustrated in Fig. 4.4A, our results suggest that in the former case, one would observe a minimum in the migration time as a function of the cluster size, with the optimal size determined by the length scale of collective information processing within the cluster. In contrast, as illustrated in Fig. 4.4B, in the latter case migration is driven by the integrated

measurements of many effectively independent agents, and thus one would observe a monotonic decrease in the migration time as a function of the cluster size [41]. Distinguishing the dependence in Fig. 4.4A from that in Fig. 4.4B using microscopy would provide phenomenological evidence of purely collective chemotaxis without relying on molecular-level details.

An important feature of our model and its analysis is that the timescale of sensing is faster than the timescale of cell response and motility (Table 4.1). However, in actuality the duration of cells' sensing timescales relative to their response timescales is unknown [25]. If the motility timescale is shorter than that of sensing for a specific cell type then the MFPT dependence on cluster size may be more complicated than predicted. For short response timescales we expect migratory behavior to be more strongly diffusive, but to still remain biased in the direction of the gradient over periods of time larger than the sensing timescale.

In our model, the precision of multicellular migration is determined in part by noise arising from ligand diffusion at the initial sensory stage. As such, the model respects the fundamental limits to the precision of collective gradient sensing set by the physics of diffusion, which were recently tested in collectives of epithelial cells [25, 33]. It will be interesting to see how these and similar limits translate from the domain of sensing to that of migration, and whether they depend on the underlying migration mechanism (purely collective, individually driven, or a mixture thereof).

REFERENCES

REFERENCES

- [1] L. Song, S. M. Nadkarni, H. U. Bödeker, C. Beta, A. Bae, C. Franck, W.-J. Rappel, W. F. Loomis, and E. Bodenschatz, “Dictyostelium discoideum chemotaxis: threshold for directed motion,” *European journal of cell biology*, vol. 85, no. 9, pp. 981–989, 2006.
- [2] H. C. Berg and E. M. Purcell, “Physics of chemoreception,” *Biophysical journal*, vol. 20, no. 2, p. 193, 1977.
- [3] G. Lan, P. Sartori, S. Neumann, V. Sourjik, and Y. Tu, “The energy-speed-accuracy trade-off in sensory adaptation,” *Nature physics*, vol. 8, no. 5, pp. 422–428, 2012.
- [4] W. Bialek and S. Setayeshgar, “Physical limits to biochemical signaling,” *Proceedings of the National Academy of Sciences of the United States of America*, vol. 102, no. 29, pp. 10 040–10 045, 2005.
- [5] K. Kaizu, W. de Ronde, J. Pajmians, K. Takahashi, F. Tostevin, and P. R. ten Wolde, “The berg-purcell limit revisited,” *Biophysical journal*, vol. 106, no. 4, pp. 976–985, 2014.
- [6] B. A. Bicknell, P. Dayan, and G. J. Goodhill, “The limits of chemosensation vary across dimensions,” *Nature communications*, vol. 6, 2015.
- [7] P. A. Iglesias and P. N. Devreotes, “Navigating through models of chemotaxis,” *Current opinion in cell biology*, vol. 20, no. 1, pp. 35–40, 2008.
- [8] E. T. Roussos, J. S. Condeelis, and A. Patsialou, “Chemotaxis in cancer,” *Nature Reviews Cancer*, vol. 11, no. 8, pp. 573–587, 2011.
- [9] R. J. Petrie, A. D. Doyle, and K. M. Yamada, “Random versus directionally persistent cell migration,” *Nature reviews Molecular cell biology*, vol. 10, no. 8, pp. 538–549, 2009.
- [10] A. Jilkine and L. Edelstein-Keshet, “A comparison of mathematical models for polarization of single eukaryotic cells in response to guided cues,” *PLoS Comput Biol*, vol. 7, no. 4, pp. e1 001 121–e1 001 121, 2011.
- [11] E. Theveneau, L. Marchant, S. Kuriyama, M. Gull, B. Moepps, M. Parsons, and R. Mayor, “Collective chemotaxis requires contact-dependent cell polarity,” *Developmental cell*, vol. 19, no. 1, pp. 39–53, 2010.
- [12] M. F. Leber and T. Efferth, “Molecular principles of cancer invasion and metastasis (review),” *International journal of oncology*, vol. 34, no. 4, pp. 881–895, 2009.

- [13] D. Hanahan and R. A. Weinberg, “The hallmarks of cancer,” *cell*, vol. 100, no. 1, pp. 57–70, 2000.
- [14] —, “Hallmarks of cancer: the next generation,” *cell*, vol. 144, no. 5, pp. 646–674, 2011.
- [15] N. A. Bhowmick, E. G. Neilson, and H. L. Moses, “Stromal fibroblasts in cancer initiation and progression,” *Nature*, vol. 432, no. 7015, pp. 332–337, 2004.
- [16] J. Condeelis and J. W. Pollard, “Macrophages: obligate partners for tumor cell migration, invasion, and metastasis,” *Cell*, vol. 124, no. 2, pp. 263–266, 2006.
- [17] J. D. Shields, M. E. Fleury, C. Yong, A. A. Tomei, G. J. Randolph, and M. A. Swartz, “Autologous chemotaxis as a mechanism of tumor cell homing to lymphatics via interstitial flow and autocrine ccr7 signaling,” *Cancer cell*, vol. 11, no. 6, pp. 526–538, 2007.
- [18] A. Puliafito, A. De Simone, G. Seano, P. A. Gagliardi, L. Di Blasio, F. Chianale, A. Gamba, L. Primo, and A. Celani, “Three-dimensional chemotaxis-driven aggregation of tumor cells,” *Scientific reports*, vol. 5, 2015.
- [19] W. J. Polacheck, J. L. Charest, and R. D. Kamm, “Interstitial flow influences direction of tumor cell migration through competing mechanisms,” *Proceedings of the National Academy of Sciences*, vol. 108, no. 27, pp. 11 115–11 120, 2011.
- [20] A. C. Shieh and M. A. Swartz, “Regulation of tumor invasion by interstitial fluid flow,” *Physical biology*, vol. 8, no. 1, p. 015012, 2011.
- [21] K. J. Cheung, E. Gabrielson, Z. Werb, and A. J. Ewald, “Collective invasion in breast cancer requires a conserved basal epithelial program,” *Cell*, vol. 155, no. 7, pp. 1639–1651, 2013.
- [22] P. Friedl, J. Locker, E. Sahai, and J. E. Segall, “Classifying collective cancer cell invasion,” *Nature Cell Biology*, vol. 14, no. 8, pp. 777–783, 2012.
- [23] N. Aceto, A. Bardia, D. T. Miyamoto, M. C. Donaldson, B. S. Wittner, J. A. Spencer, M. Yu, A. Pely, A. Engstrom, H. Zhu, B. W. Brannigan, R. Kapur, S. L. Stott, T. Shioda, S. Ramaswamy, D. T. Ting, C. P. Lin, M. Toner, D. A. Haber, and S. Maheswaran, “Circulating tumor cell clusters are oligoclonal precursors of breast cancer metastasis,” *Cell*, vol. 158, no. 5, pp. 1110–1122, 2014.
- [24] F. Dahlquist, R. Elwell, and P. S. Lovely, “Studies of bacterial chemotaxis in defined concentration gradients. a model for chemotaxis toward l-serine,” *Journal of supramolecular structure*, vol. 4, no. 3, pp. 329–342, 1976.
- [25] D. Ellison, A. Mugler, M. D. Brennan, S. H. Lee, R. J. Huebner, E. R. Shamir, L. A. Woo, J. Kim, P. Amar, I. Nemenman *et al.*, “Cell–cell communication enhances the capacity of cell ensembles to sense shallow gradients during morphogenesis,” *Proceedings of the National Academy of Sciences*, p. 201516503, 2016.
- [26] R. G. Endres and N. S. Wingreen, “Accuracy of direct gradient sensing by cell-surface receptors,” *Progress in biophysics and molecular biology*, vol. 100, no. 1, pp. 33–39, 2009.

- [27] —, “Accuracy of direct gradient sensing by single cells,” *Proceedings of the National Academy of Sciences*, vol. 105, no. 41, pp. 15 749–15 754, 2008.
- [28] B. Hu, W. Chen, W.-J. Rappel, and H. Levine, “Physical limits on cellular sensing of spatial gradients,” *Physical review letters*, vol. 105, no. 4, p. 048104, 2010.
- [29] P. J. Van Haastert and M. Postma, “Biased random walk by stochastic fluctuations of chemoattractant-receptor interactions at the lower limit of detection,” *Biophysical journal*, vol. 93, no. 5, pp. 1787–1796, 2007.
- [30] M. Postma, J. Roelofs, J. Goedhart, T. W. Gadella, A. J. Visser, and P. J. Van Haastert, “Uniform camp stimulation of dictyostelium cells induces localized patches of signal transduction and pseudopodia,” *Molecular biology of the cell*, vol. 14, no. 12, pp. 5019–5027, 2003.
- [31] C. A. Parent, “Making all the right moves: chemotaxis in neutrophils and dictyostelium,” *Current opinion in cell biology*, vol. 16, no. 1, pp. 4–13, 2004.
- [32] W. J. Rosoff, J. S. Urbach, M. A. Esrick, R. G. McAllister, L. J. Richards, and G. J. Goodhill, “A new chemotaxis assay shows the extreme sensitivity of axons to molecular gradients,” *Nature neuroscience*, vol. 7, no. 6, pp. 678–682, 2004.
- [33] A. Mugler, A. Levchenko, and I. Nemenman, “Limits to the precision of gradient sensing with spatial communication and temporal integration,” *Proceedings of the National Academy of Sciences*, p. 201509597, 2016.
- [34] S. Fancher and A. Mugler, “Fundamental limits to collective concentration sensing in cell populations,” *Phys. Rev. Lett.*, vol. 118, p. 078101, Feb 2017. [Online]. Available: <http://link.aps.org/doi/10.1103/PhysRevLett.118.078101>
- [35] A. Levchenko and P. A. Iglesias, “Models of eukaryotic gradient sensing: application to chemotaxis of amoebae and neutrophils,” *Biophysical journal*, vol. 82, no. 1, pp. 50–63, 2002.
- [36] P. Lu, A. J. Ewald, G. R. Martin, and Z. Werb, “Genetic mosaic analysis reveals fgf receptor 2 function in terminal end buds during mammary gland branching morphogenesis,” *Developmental biology*, vol. 321, no. 1, pp. 77–87, 2008.
- [37] A. J. Kabla, “Collective cell migration: leadership, invasion and segregation,” *Journal of The Royal Society Interface*, p. rsif20120448, 2012.
- [38] A. Szabó, R. Ünneper, E. Méhes, W. Twal, W. Argraves, Y. Cao, and A. Czirók, “Collective cell motion in endothelial monolayers,” *Physical biology*, vol. 7, no. 4, p. 046007, 2010.
- [39] M. Basan, J. Elgeti, E. Hannezo, W.-J. Rappel, and H. Levine, “Alignment of cellular motility forces with tissue flow as a mechanism for efficient wound healing,” *Proceedings of the National Academy of Sciences*, vol. 110, no. 7, pp. 2452–2459, 2013.
- [40] A. Janulevicius, M. van Loosdrecht, and C. Picioreanu, “Short-range guiding can result in the formation of circular aggregates in myxobacteria populations,” *PLoS Comput Biol*, vol. 11, 2015.

- [41] A. M. Simons, “Many wrongs: the advantage of group navigation,” *Trends in ecology & evolution*, vol. 19, no. 9, pp. 453–455, 2004.
- [42] L. Coburn, L. Cerone, C. Torney, I. D. Couzin, and Z. Neufeld, “Tactile interactions lead to coherent motion and enhanced chemotaxis of migrating cells,” *Physical biology*, vol. 10, no. 4, p. 046002, 2013.
- [43] B. A. Camley, J. Zimmermann, H. Levine, and W.-J. Rappel, “Emergent collective chemotaxis without single-cell gradient sensing,” *Phys. Rev. Lett.*, vol. 116, p. 098101, Mar 2016. [Online]. Available: <http://link.aps.org/doi/10.1103/PhysRevLett.116.098101>
- [44] R. Mayor and C. Carmona-Fontaine, “Keeping in touch with contact inhibition of locomotion,” *Trends in cell biology*, vol. 20, no. 6, pp. 319–328, 2010.
- [45] O. J. Maclaren, A. Fletcher, H. Byrne, and P. K. Maini, “Models, measurement and inference in epithelial tissue dynamics,” *arXiv preprint arXiv:1506.05052*, 2015.
- [46] F. Graner and J. A. Glazier, “Simulation of biological cell sorting using a two-dimensional extended potts model,” *Physical review letters*, vol. 69, no. 13, p. 2013, 1992.
- [47] M. H. Swat, G. L. Thomas, J. M. Belmonte, A. Shirinifard, D. Hmeljak, and J. A. Glazier, “Multi-scale modeling of tissues using compucell3d,” *Methods in cell biology*, vol. 110, p. 325, 2012.
- [48] A. F. M. Marée, V. A. Grieneisen, and P. Hogeweg, “The Cellular Potts Model and Biophysical Properties of Cells, Tissues and Morphogenesis,” in *Single-Cell-Based Models in Biology and Medicine*, ser. Mathematics and Biosciences in Interaction, A. R. A. Anderson, M. A. J. Chaplain, and K. A. Rejniak, Eds. Birkhäuser Basel, 2007, dOI: 10.1007/978-3-7643-8123-3_5.
- [49] K. Torres and S. B. Horwitz, “Mechanisms of taxol-induced cell death are concentration dependent,” *Cancer research*, vol. 58, no. 16, pp. 3620–3626, 1998.
- [50] R. Grantab, S. Sivananthan, and I. F. Tannock, “The penetration of anticancer drugs through tumor tissue as a function of cellular adhesion and packing density of tumor cells,” *Cancer research*, vol. 66, no. 2, pp. 1033–1039, 2006.
- [51] Y. Malam, M. Loizidou, and A. M. Seifalian, “Liposomes and nanoparticles: nanosized vehicles for drug delivery in cancer,” *Trends in pharmacological sciences*, vol. 30, no. 11, pp. 592–599, 2009.
- [52] A. I. Minchinton and I. F. Tannock, “Drug penetration in solid tumours,” *Nature Reviews Cancer*, vol. 6, no. 8, pp. 583–592, 2006.
- [53] I. K. Kwon, S. C. Lee, B. Han, and K. Park, “Analysis on the current status of targeted drug delivery to tumors,” *Journal of Controlled Release*, vol. 164, no. 2, pp. 108–114, 2012.
- [54] M. C. Boelens, T. J. Wu, B. Y. Nabet, B. Xu, Y. Qiu, T. Yoon, D. J. Azam, C. Twyman-Saint Victor, B. Z. Wiemann, H. Ishwaran, P. J. ter Brugge, J. Jonkers, J. Slingerland, and A. J. Minn, “Exosome transfer from stromal to breast cancer cells regulates therapy resistance pathways,” *Cell*, vol. 159, no. 3, pp. 499–513, 2014.

- [55] P. Vader, X. O. Breakefield, and M. J. Wood, "Extracellular vesicles: emerging targets for cancer therapy," *Trends in molecular medicine*, vol. 20, no. 7, pp. 385–393, 2014.
- [56] R. D. Nelson, P. G. Quie, and R. L. Simmons, "Chemotaxis under agarose: a new and simple method for measuring chemotaxis and spontaneous migration of human polymorphonuclear leukocytes and monocytes," *The Journal of Immunology*, vol. 115, no. 6, pp. 1650–1656, 1975.
- [57] A. Iellem, M. Mariani, R. Lang, H. Recalde, P. Panina-Bordignon, F. Sinigaglia, and D. D'Ambrosio, "Unique chemotactic response profile and specific expression of chemokine receptors ccr4 and ccr8 by cd4+ cd25+ regulatory t cells," *The Journal of experimental medicine*, vol. 194, no. 6, pp. 847–854, 2001.
- [58] U. Mayr-Wohlfart, J. Waltenberger, H. Hausser, S. Kessler, K.-P. Günther, C. Dehio, W. Puhl, and R. Brenner, "Vascular endothelial growth factor stimulates chemotactic migration of primary human osteoblasts," *Bone*, vol. 30, no. 3, pp. 472–477, 2002.
- [59] J. Fiedler, F. Leucht, J. Waltenberger, C. Dehio, and R. E. Brenner, "Vegf-a and plgf-1 stimulate chemotactic migration of human mesenchymal progenitor cells," *Biochemical and biophysical research communications*, vol. 334, no. 2, pp. 561–568, 2005.
- [60] S. Funamoto, K. Milan, R. Meili, and R. A. Firtel, "Role of phosphatidylinositol 3 kinase and a downstream pleckstrin homology domain-containing protein in controlling chemotaxis in *Dictyostelium*," *The Journal of cell biology*, vol. 153, no. 4, pp. 795–810, 2001.
- [61] G. Mouneimne, V. DesMarais, M. Sidani, E. Scemes, W. Wang, X. Song, R. Eddy, and J. Condeelis, "Spatial and temporal control of cofilin activity is required for directional sensing during chemotaxis," *Current biology*, vol. 16, no. 22, pp. 2193–2205, 2006.
- [62] R. R. Kay, P. Langridge, D. Traynor, and O. Hoeller, "Changing directions in the study of chemotaxis," *Nature Reviews Molecular Cell Biology*, vol. 9, no. 6, pp. 455–463, 2008.
- [63] M. McCutcheon, "Chemotaxis in leukocytes," *Physiological reviews*, vol. 26, no. 3, pp. 319–336, 1946.
- [64] R. Gorelik and A. Gautreau, "Quantitative and unbiased analysis of directional persistence in cell migration," *Nature protocols*, vol. 9, no. 8, pp. 1931–1943, 2014.
- [65] E. A. Codling, M. J. Plank, and S. Benhamou, "Random walk models in biology," *Journal of the Royal Society Interface*, vol. 5, no. 25, pp. 813–834, 2008.
- [66] I. Dang, R. Gorelik, C. Sousa-Blin, E. Derivery, C. Guérin, J. Linkner, M. Nemethova, J. G. Dumortier, F. A. Giger, T. A. Chipysheva *et al.*, "Inhibitory signalling to the arp2/3 complex steers cell migration," *Nature*, vol. 503, no. 7475, pp. 281–284, 2013.

- [67] B. J. Kim, P. Hannanta-Anan, M. Chau, Y. S. Kim, M. A. Swartz, and M. Wu, “Cooperative roles of sdf-1 α and egf gradients on tumor cell migration revealed by a robust 3d microfluidic model,” *PloS one*, vol. 8, no. 7, p. e68422, 2013.
- [68] H. G. Othmer, S. R. Dunbar, and W. Alt, “Models of dispersal in biological systems,” *Journal of mathematical biology*, vol. 26, no. 3, pp. 263–298, 1988.
- [69] B. Mosadegh, W. Saadi, S.-J. Wang, and N. L. Jeon, “Epidermal growth factor promotes breast cancer cell chemotaxis in cxcl12 gradients,” *Biotechnology and bioengineering*, vol. 100, no. 6, pp. 1205–1213, 2008.
- [70] S.-J. Wang, W. Saadi, F. Lin, C. M.-C. Nguyen, and N. L. Jeon, “Differential effects of egf gradient profiles on mda-mb-231 breast cancer cell chemotaxis,” *Experimental cell research*, vol. 300, no. 1, pp. 180–189, 2004.
- [71] S. M. Wahl, D. A. Hunt, L. M. Wakefield, N. McCartney-Francis, L. M. Wahl, A. B. Roberts, and M. B. Sporn, “Transforming growth factor type beta induces monocyte chemotaxis and growth factor production,” *Proceedings of the National Academy of Sciences*, vol. 84, no. 16, pp. 5788–5792, 1987.
- [72] R. Bischoff, “Chemotaxis of skeletal muscle satellite cells,” *Developmental dynamics*, vol. 208, no. 4, pp. 505–515, 1997.
- [73] D. A. Clark and R. Coker, “Molecules in focus transforming growth factor-beta (tgf- β),” *The international journal of biochemistry & cell biology*, vol. 30, no. 3, pp. 293–298, 1998.
- [74] D. Javelaud and A. Mauviel, “Mammalian transforming growth factor- β s: Smad signaling and physio-pathological roles,” *The international journal of biochemistry & cell biology*, vol. 36, no. 7, pp. 1161–1165, 2004.
- [75] M. Pang, A. Georgoudaki, L. Lambut, J. Johansson, V. Tabor, K. Hagikura, Y. Jin, M. Jansson, J. Alexander, C. Nelson *et al.*, “Tgf- β 1-induced emt promotes targeted migration of breast cancer cells through the lymphatic system by the activation of ccr7/ccl21-mediated chemotaxis,” *Oncogene*, vol. 35, no. 6, pp. 748–760, 2016.
- [76] J. Varennes, B. Han, and A. Mugler, “Collective chemotaxis through noisy multicellular gradient sensing,” *Biophysical Journal*, vol. 111, no. 3, p. 640, 2016.
- [77] W. Alt, “Biased random walk models for chemotaxis and related diffusion approximations,” *Journal of mathematical biology*, vol. 9, no. 2, pp. 147–177, 1980.
- [78] C. S. Patlak, “Random walk with persistence and external bias,” *Bulletin of Mathematical Biology*, vol. 15, no. 3, pp. 311–338, 1953.
- [79] G. Malet-Engra, W. Yu, A. Oldani, J. Rey-Barroso, N. S. Gov, G. Scita, and L. Dupré, “Collective cell motility promotes chemotactic prowess and resistance to chemorepulsion,” *Current Biology*, vol. 25, no. 2, pp. 242–250, 2015.
- [80] E. Scarpa and R. Mayor, “Collective cell migration in development,” *J Cell Biol*, vol. 212, no. 2, pp. 143–155, 2016.

- [81] P. Friedl and K. Wolf, “Plasticity of cell migration: a multiscale tuning model,” *The Journal of cell biology*, vol. 188, no. 1, pp. 11–19, 2010.
- [82] T. B. Rasmussen and M. Givskov, “Quorum-sensing inhibitors as anti-pathogenic drugs,” *International Journal of Medical Microbiology*, vol. 296, no. 2, pp. 149–161, 2006.
- [83] A. Szabó and R. Mayor, “Modelling collective cell migration of neural crest,” *Current opinion in cell biology*, vol. 42, pp. 22–28, 2016.
- [84] J. Varennes and A. Mugler, “Sense and sensitivity: physical limits to multicellular sensing, migration and drug response,” *Molecular Pharmaceutics*, 2016.
- [85] B. H. Defranco, B. M. Nickel, C. J. Baty, J. S. Martinez, V. L. Gay, V. C. Sandulache, D. J. Hackam, and S. A. Murray, “Migrating cells retain gap junction plaque structure and function,” *Cell communication & adhesion*, vol. 15, no. 3, pp. 273–288, 2008.
- [86] A. Haeger, K. Wolf, M. M. Zegers, and P. Friedl, “Collective cell migration: guidance principles and hierarchies,” *Trends in cell biology*, vol. 25, no. 9, pp. 556–566, 2015.
- [87] D. Ramel, X. Wang, C. Laflamme, D. J. Montell, and G. Emery, “Rab11 regulates cell–cell communication during collective cell movements,” *Nature cell biology*, vol. 15, no. 3, pp. 317–324, 2013.
- [88] H. Gerhardt, M. Golding, M. Fruttiger, C. Ruhrberg, A. Lundkvist, A. Abramson, M. Jeltsch, C. Mitchell, K. Alitalo, D. Shima *et al.*, “Vegf guides angiogenic sprouting utilizing endothelial tip cell filopodia,” *The Journal of cell biology*, vol. 161, no. 6, pp. 1163–1177, 2003.
- [89] M. Hsu, T. Andl, G. Li, J. L. Meinkoth, and M. Herlyn, “Cadherin repertoire determines partner-specific gap junctional communication during melanoma progression,” *J cell Sci*, vol. 113, no. 9, pp. 1535–1542, 2000.
- [90] P. Friedl and D. Gilmour, “Collective cell migration in morphogenesis, regeneration and cancer,” *Nature reviews Molecular cell biology*, vol. 10, no. 7, pp. 445–457, 2009.
- [91] D. T. Gillespie, “The chemical langevin equation,” *The Journal of Chemical Physics*, vol. 113, no. 1, pp. 297–306, 2000.
- [92] See <https://doi.org/10.5281/zenodo.54980> for source code.
- [93] G. B. Ermentrout and L. Edelstein-Keshet, “Cellular automata approaches to biological modeling,” *Journal of theoretical Biology*, vol. 160, no. 1, pp. 97–133, 1993.
- [94] T. Maire and H. Youk, “Molecular-level tuning of cellular autonomy controls the collective behaviors of cell populations,” *Cell systems*, vol. 1, no. 5, pp. 349–360, 2015.
- [95] C. Mente, A. Voss-Böhme, and A. Deutsch, “Analysis of individual cell trajectories in lattice-gas cellular automaton models for migrating cell populations,” *Bulletin of mathematical biology*, vol. 77, no. 4, pp. 660–697, 2015.

- [96] B. A. Camley, J. Zimmermann, H. Levine, and W.-J. Rappel, “Collective signal processing in cluster chemotaxis: roles of adaptation, amplification, and co-attraction in collective guidance,” *arXiv preprint arXiv:1512.00544*, 2015.
- [97] T. Vicsek, A. Czirók, E. Ben-Jacob, I. Cohen, and O. Shochet, “Novel type of phase transition in a system of self-driven particles,” *Physical review letters*, vol. 75, no. 6, p. 1226, 1995.
- [98] D. Cai, W. Dai, M. Prasad, J. Luo, N. S. Gov, and D. J. Montell, “Modeling and analysis of collective cell migration in an in vivo three-dimensional environment,” *Proceedings of the National Academy of Sciences*, vol. 113, no. 15, pp. E2134–E2141, 2016.
- [99] A. Bianco, M. Poukkula, A. Cliffe, J. Mathieu, C. M. Luque, T. A. Fulga, and P. Rørth, “Two distinct modes of guidance signalling during collective migration of border cells,” *Nature*, vol. 448, no. 7151, pp. 362–365, 2007.
- [100] D. J. Montell, “Morphogenetic cell movements: diversity from modular mechanical properties,” *Science*, vol. 322, no. 5907, pp. 1502–1505, 2008.
- [101] T. S. Deisboeck and I. D. Couzin, “Collective behavior in cancer cell populations,” *Bioessays*, vol. 31, no. 2, pp. 190–197, 2009.
- [102] P. Kulesa and S. Fraser, “Neural crest cell dynamics revealed by time-lapse video microscopy of whole embryo chick explant cultures,” *Developmental biology*, vol. 204, no. 2, pp. 327–344, 1998.
- [103] C. Gaggioli, S. Hooper, C. Hidalgo-Carcedo, R. Grosse, J. F. Marshall, K. Harrington, and E. Sahai, “Fibroblast-led collective invasion of carcinoma cells with differing roles for rhoGTPases in leading and following cells,” *Nature cell biology*, vol. 9, no. 12, pp. 1392–1400, 2007.
- [104] N. Bardeesy and R. A. DePinho, “Pancreatic cancer biology and genetics,” *Nature Reviews Cancer*, vol. 2, no. 12, pp. 897–909, 2002.
- [105] C. W. Gardiner *et al.*, *Handbook of stochastic methods*. Springer Berlin, 1985, vol. 3.
- [106] See Supplemental Information for methods, derivations, and additional discussion.
- [107] See <https://doi.org/10.5281/zenodo.401040> for source code.
- [108] K. Takeda, D. Shao, M. Adler, P. G. Charest, W. F. Loomis, H. Levine, A. Groisman, W.-J. Rappel, and R. A. Firtel, “Incoherent feedforward control governs adaptation of activated ras in a eukaryotic chemotaxis pathway,” *Science signaling*, vol. 5, no. 205, p. ra2, 2012.